AERODYNAMICS OF WIND EROSION AND PARTICLE COLLECTION THROUGH VEGETATIVE CONTROLS

by

HOWELL B. GONZALES

B.S., University of the Philippines - Los Baños, 2001

M.S., Kansas State University, 2010

AN ABSTRACT OF A DISSERTATION

Submitted in partial fulfillment of the requirements for the degree

DOCTOR OF PHILOSOPHY

Department of Biological and Agricultural Engineering

College of Engineering

KANSAS STATE UNIVERSITY

Manhattan, Kansas

2015

Abstract

Wind erosion is an important problem in many locations, including the Great Plains, that needs to be controlled to protect soil and land resources. This research was conducted to assess the effectiveness of vegetation (specifically, standing vegetation and tree barriers) as controls for wind erosion. Specific objectives were to: (1) measure sand transport and abrasion on artificial standing vegetation, (2) determine porosity and drag of a single row of Osage orange (*Maclura pomifera*) barrier, (3) assess effectiveness of Osage orange barriers in reducing dust, (4) predict airflow through standing vegetation, and (5) predict airflow and particle collection through Osage orange barriers.

Wind tunnel tests were conducted to measure wind speed profiles, relative abrasion energies, and sand discharge rates for bare sand and for two vegetation heights (150 and 220 mm) at various densities of vegetation. Results showed that vegetation density was directly related to threshold velocity and inversely related to sand discharge. The coefficient of abrasion was adversely affected by saltation discharge but did not depend on wind speed.

Field tests measured the aerodynamic and optical porosities of Osage orange trees using wind profiles and image analysis, respectively, and an empirical relationship between the two porosities was derived. Vertical wind profiles were also used to estimate drag coefficients. Optical porosity correlated well with the drag coefficient. Field measurements also showed a row of Osage orange barrier resulted in particulate concentration reduction of 15 to 54% for PM2.5 and 23 to 65% for PM10.

A computational fluid dynamics (CFD) software (OpenFOAM) was used to predict airflow in a wind tunnel with artificial standing vegetation. Predicted wind speeds differed slightly from the measured values, possibly due to oscillatory motions of the standing vegetation

not accounted for in the CFD simulation. OpenFOAM was also used to simulate airflow and particle transport through a row of Osage orange barrier. Predicted and measured wind speeds agreed well. Measured dust concentration reduction at two points (upwind and downwind) were also similar to the predicted results.

AERODYNAMICS OF WIND EROSION AND PARTICLE COLLECTION THROUGH VEGETATIVE CONTROLS

by

HOWELL B. GONZALES

B.S., University of the Philippines - Los Baños, 2001
M.S., Kansas State University, 2010

A DISSERTATION

Submitted in partial fulfillment of the requirements for the degree

DOCTOR OF PHILOSOPHY

Department of Biological and Agricultural Engineering
College of Engineering

KANSAS STATE UNIVERSITY
Manhattan, Kansas

2015

Approved by:

Co-Major Professor
Ronaldo G. Maghirang

Co-Major Professor
Mark E. Casada

Abstract

Wind erosion is an important problem in many locations, including the Great Plains, that needs to be controlled to protect soil and land resources. This research was conducted to assess the effectiveness of vegetation (specifically, standing vegetation and tree barriers) as controls for wind erosion. Specific objectives were to: (1) measure sand transport and abrasion on artificial standing vegetation, (2) determine porosity and drag of a single row of Osage orange (*Maclura pomifera*) barrier, (3) assess effectiveness of Osage orange barriers in reducing dust, (4) predict airflow through standing vegetation, and (5) predict airflow and particle collection through Osage orange barriers.

Wind tunnel tests were conducted to measure wind speed profiles, relative abrasion energies, and sand discharge rates for bare sand and for two vegetation heights (150 and 220 mm) at various densities of vegetation. Results showed that vegetation density was directly related to threshold velocity and inversely related to sand discharge. The coefficient of abrasion was adversely affected by saltation discharge but did not depend on wind speed.

Field tests measured the aerodynamic and optical porosities of Osage orange trees using wind profiles and image analysis, respectively, and an empirical relationship between the two porosities was derived. Vertical wind profiles were also used to estimate drag coefficients. Optical porosity correlated well with the drag coefficient. Field measurements also showed a row of Osage orange barrier resulted in particulate concentration reduction of 15 to 54% for PM2.5 and 23 to 65% for PM10.

A computational fluid dynamics (CFD) software (OpenFOAM) was used to predict airflow in a wind tunnel with artificial standing vegetation. Predicted wind speeds differed slightly from the measured values, possibly due to oscillatory motions of the standing vegetation

not accounted for in the CFD simulation. OpenFOAM was also used to simulate airflow and particle transport through a row of Osage orange barrier. Predicted and measured wind speeds agreed well. Measured dust concentration reduction at two points (upwind and downwind) were also similar to the predicted results.

Copyright

Table of Contents

List of Figures

List of Tables

List of Nomenclature

Acronyms

2D	Two-dimensional
3D	Three-dimensional
ASCII	American Standard Code for Information Interchange
CAD	Computer-aided design
CFD	Computational fluid dynamics
FA	Floor area per plant
FSA	Frontal steam and leaf areas per plant
GMD	Geometric mean diameter
GPL	GNU public license
GSD	Geometric standard deviation
LAI	Leaf area index
LES	Large eddy simulation
LV	Low volume
MOS	Metal oxide semiconductor
NRI	National Resources Inventory
OpenFOAM	Open-source field operation and manipulation
OBJ	Object file format
OS	Operating system
PM	Particulate matter
$PM_{2.5}$	Particulate matter with equivalent aerodynamic diameter of 2.5 μm or less
PM_{10}	Particulate matter with equivalent aerodynamic diameter of 10 μm or less
PSD	Particle size distribution
PTFE	Polytetrafluoroethylene
RANS	Reynolds-averaged Navier-Stokes
RAS	Reynolds-averaged stress
RGB	Red green blue
RNG	Re-normalization group
RSM	Reynolds stress model
SAI	Silhouette area index
SEM	Standard error of the mean
SIMPLE	Semi-implicit method for pressure-linked equations
SST	Shear stress transport
STL	STereoLithography file format
USDA	United States Department of Agriculture
USDA NRCS	United States Department of Agriculture Natural Resources Conservation Service

Notations

a	Roughness parameter (0.17) in equation 7.14
A_a	Area of soil inside the abrasion sensor (m^2)
A_{ah}	Area of horizontal abrasion sensor (m^2)
A_{av}	Area of vertical abrasion sensor (m^2)

α	Permeability constant (m^2)
α_p	Aerodynamic porosity
β	Turbulent model constant
β_D	Inertial resistance (m^{-1})
β_p	Optical porosity
β_c	Optical porosity of tree crown
β_t	Optical porosity of tree trunk
C	Concentration (μg m^{-3})
C_{an}	Coefficient of abrasion (m^{-1})
$C_{1\varepsilon}$	Turbulence model constant
$C_{2\varepsilon}$	Turbulence model constant
C_μ	Turbulence model constant
C_C	Slip correction factor
C_D	Drag coefficient
C_{D0}	Zero-lift drag coefficient
C_n	Effective drag coefficient
D	Displacement height (cm)
D_b	Drag force of the barrier (N)
D_g	Drag force of the ground (N)
$\bar{\bar{d}}$	Porosity parameter in OpenFOAM
d_{ctube}	Diameter of central catch tube (m)
d_h	Diameter of horizontal abrasion sensor (m)
∇p	Pressure gradient (Pa)
d_p	Particle diameter (μm)
d_{pipe}	Diameter of pipe used as dust distributor (m)
ε	Turbulence dissipation rate (m^2 s^{-3})
ε_{in}	Turbulence dissipation rate of inflow (m^2 s^{-3})
$\bar{\bar{f}}$	Porosity parameter in OpenFOAM
Γ_{bl}	Bulk drag coefficient
Γ_D	Effective diffusion coefficient
Γ_L	Laminar diffusion coefficient
Γ_T	Turbulent diffusion coefficient
Γ_ϕ	Diffusion coefficient from the general transport equation
H	Average tree height (m)
I	Turbulence intensity (%)
k	Turbulence kinetic energy (m^2 s^{-2})
k_{in}	Turbulence kinetic energy of inflow (m^2 s^{-2})
κ	von Karman constant
k_r	Resistance coefficient
k_1	Roughness relationship (1+ $2a$)
ℓ_{av}	Length of vertical abrasion sensor (m)
λ	Mean free path (μm)
m	Thickness or diameter of canopy (m)
m_a	Mass of soil loss from abrasion sensor (g)

m_{ctube}	Mass of sand collected in the central catch tubes (g)
m_{tub}	Mass of sand collected in the tub (g)
μ	Fluid viscosity (N s m^{-2})
μ_{eff}	Effective viscosity (N s m^{-2})
μ_t	Turbulent viscosity (N s m^{-2})
υ	Kinematic viscosity (m^2 s^{-1})
p_S	Static pressure (Pa)
p_T	Total pressure or stagnation pressure (Pa)
ϕ	Fluid property for the general transport equation
Q_{air}	Volumetric flow rate (m^3 s^{-1})
q_{eff}	Effective saltation discharge (kg m^{-1})
q_h	Sand discharge of the horizontal abrasion sensor (kg)
q_{slot}	Sand discharge flux of the vertical slot samplers (g m^{-1} s^{-1})
q_{tube}	Sand discharge flux of central catch tubes (g m^{-1} s^{-1})
q_v	Sand discharge of the vertical abrasion sensor (kg)
ρ	Fluid density (kg m^{-3})
S_i	Momentum source
S_{ij}	Shearing rate tensor
S_ϕ	Source term
σ_ε	Turbulent Prandtl number for turbulence kinetic energy
σ_k	Turbulent Prandtl number for turbulence dissipation rate
t	Duration of sampling (s)
τ_{ij}	Viscous stress component for the Navier-Stokes equation
u^*	Friction velocity (m s^{-1})
u_i	Velocity component (m s^{-1})
u_x	Stream-wise (downwind) velocity component (m s^{-1})
u_y	Cross-wind velocity component (m s^{-1})
u_z	Vertical velocity component (m s^{-1})
U_b	Throughflow velocity (m s^{-1})
U_{0H}	Freestream velocity (m s^{-1})
U^*_v	Friction velocity (m s^{-1})
U^*_{ot}	Threshold friction velocity (m s^{-1})
u	Fluid velocity (m s^{-1})
V_{avg}	Average velocity (m s^{-1})
w_{av}	Width of vertical abrasion sensor (m)
w_{slot}	Width of slot sampler (m)
x	Stream-wise direction
y	Cross stream direction
z	Vertical direction
Z_f	Roughness length of the vegetated surface (cm)
Z_o	Aerodynamic roughness length (cm)
Z_{os}	Aerodynamic roughness length of the smooth surface (cm)

Acknowledgments

I would like to acknowledge our dear Lord Jesus Christ who gave me wisdom and knowledge to get through with my PhD studies here at Kansas State University and had kept me strong through tough times especially during the loss of my mom which occurred two weeks before I got here in the United States. You are a miraculous God indeed and worthy of all praises!

Secondly, I would like to thank my wife, Gilda, for an amazing support and prayers, though there were rough times, you are indeed my inspiration on continuing my education and hopefully we can continue to be a blessing to others. To my family, my Dad who is equally supportive of me from the start of my studies here, I thank you for the love and confidence you put in me. My sister Hazel who was all the more present and active in prayers when I was starting up to the end of my PhD studies; also to Kuya Esteban for the encouragement to pursue PhD studies and baby Zeleste who was a great addition and major inspiration to the entire Gonzales family; to my sister Haidee who vouched for me as her little brother who wanted to pursue an advanced degree and make my dreams come true to have an advanced degree; my brother Harvey and Ate Mai and my nephews Liam and Lance and niece Lana who equally gave inspiration and joy especially when I talk with them online in between the stressful hours of writing the manuscript. And to my mom who has been my inspiration since the start of my graduate studies, we miss you so much! To the Bubutan and Providо family, thank you for being my prayer warriors from the start of my graduate studies! Thank you Mama Rose and Papa Polding for being there always for me.

I would like to thank my co-adviser, Dr. Ronaldo Maghirang, for opening an opportunity for me to pursue graduate studies here at Kansas State University. Thank you for the knowledge

that you have imparted to me from the very beginning of my MS schooling to my PhD studies. Thank you for all the advice and thank you for your patience, support and encouragement especially throughout the writing of my manuscript. To my co-adviser Dr. Casada, it is a pleasure to work with you at USDA and thank you for giving me confidence to pursue a lot of things and the freedom to conceptualize majority of the topics for my PhD dissertation. It is with deepest gratitude and humility that I have become an integral part of wind erosion and CFD research that you are involved in.

I would like to thank Dr. John Tatarko, one of my committee members for his invaluable support since the day I started working at USDA for the wind tunnel studies and field experiments he was always there helping out in every which way he could aside from the inputs to my dissertation. To the rest of my committee members Dr. Larry Glasgow and Dr. Charles Barden, thank you for their inputs and openness to inquiries addressed regarding the writing of the manuscript. Thank you Dr. Barden for your student Pabodha Galgamuwa who helped identify the vegetative barrier I used for my research, the Osage orange tree. To Dr. Jason Bergtold, a very good friend of mine who was the outside chair of my committee (to my surprise!), thank you so much for your inputs and suggestions.

I would like to thank the invaluable support provided by USDA SPIERU for the entire research. I also would like to thank the USDA wind erosion and engineering people, Dr. Larry Hagen, Dr. Fred Fox, Matt Kucharski, Hubert Lagae, Dr. Dennis Tilley, and Neil Baker and also the students who have come and gone (Michael Berggren, Michelle Busch, Jeremy Meeks, Nathan Goetzinger, AC Maurin, Andrew DeMaranville, and Kevin Hamm) who helped me so much during the start of my research. Dr. Hagen for guiding and helping me conceptualize the topics for my dissertation and equally visiting my experiments from time to time. Dr. Fred Fox

who introduced me to the use of Linux and OpenFOAM which was really encourage me to broaden my knowledge in programming. Matt Kucharski who has been there from day one as I've started my wind tunnel experiment to the end of my field experiments, bro, you just don't know how much I am grateful for what you have done to help me get through all of my experiments! "Bai, daghang salamat!" Dr. Tilley for helping out in driving me to the experiment site to conduct my sampling and tests. Also, thank you Dr. Jeff Wilson for letting me use again the LD instrument for my PhD research and thank you Dr. Rhett Kaufmann for assisting me in using the instrument. Thank you Dr. Rumela Bhadra for the moral support and help during field work.

To the Manhattan Filipino community who accepted Gilda and I as part of a loving Filipino family; all of you who were hospitable and caring to us (ahem, Tita Beth!) To Kuya Eric, a big brother, a friend and a mentor who accommodated me when I was starting my K-State life, you are indeed a blessing to me. To Kuya Attan and Ate Karen, salamat sa pangugumusta and pagmomonitor ng progress ko sa dissertation kung ga-graduate na ba ako or hindi... Hehehe! Finally! Tapos na! Thanks also for lending us your car! Wow, am truly blessed to have you as friends! Although nakakasawa rin na maging BINGO master every year! LOL! To the Andrada family, thanks for the "firsts" moments (first time to play in the snow; first time to watch football game at K-state) and the unending food supply as your neighbors in Jardine (thank you Ate Gless sa pagluluto!), you will forever become part of our extended family in Manhattan. To the McHenry and Santiago (Scott and Rochelle) families, thank you for the support, prayers and friendship. To Aline and Travis Kummer, for the unending support (delicious veggies!) and prayers before and after my final exam, amazingly you have been great friends to us! To Mike and Sheryll, you have been great prayer warriors for me during my experimentations, defense,

and writing of the manuscript. You have shown me that courage and faith in our Lord Jesus Christ is the greatest favor that Gilda and I could ever have! To Beale and Hilt families, thank you for the friendship and delicious delicacies during our bible group studies and gatherings! To Hetland family, thank you for everything from the prayers and support you have provided to Gilda and I, may our Lord Jesus Christ continue to shower you wonderful blessings! To Kuya Max and Ate Ayie, miss you na po! Salamat sa palaging pangungumusta sa aking pag-aaral! Finally, am done! To the Woeppel family, thank you for the prayers and moral support from the very first time I pursued my graduate studies.

To Galos family, you are amazing friends and extended family to us in Kansas City. Thanks for the support you have given us! You are such a wonderful blessing to Gilda and I. To the Ybañez family, amazing people who have been amazing friends and extended families to us from Junction City. To Nathan (thank you for the very nice figures I have included in my dissertation) and Robee, thank you for helping us out during our transition and providing us a shelter where we could not afford one. May our Lord Jesus Christ return those favors to you and to the entire Sandoval and Ybañez families. To Ate Naynie and Kuya Paul Ibbetson and the entire Ibbetson family who helped us when I was starting my PhD studies and also prayed for me to finish my schooling and finally am thankful that it is!

To the Wamego Family Worship Center Church, you are all indeed great spiritual blessings to us! Thank you for all the prayers and support that you have given us, your prayers are more than enough! To Pastors Pat and Beth Green, thanks for welcoming us with open arms to the church which was such a wonderful spiritual family to us! To Grandpa Larry and Grandma Carol Brunner, you just don't know how much you have helped us! We really appreciate the love of Christ from you!

CHAPTER 1 - Introduction

1.1. Background and Rationale

Wind erosion is an important problem in arid and semi-arid regions of the Great Plains in the United States. High wind speeds, relatively dry soil surface, and low vegetation production potential due to high temperatures and low precipitation make the state of Kansas particularly susceptible to wind erosion. Preservation of vegetative cover is a common method to control wind erosion for agricultural lands. As an economical alternative management practice for long-term wind erosion control, many Kansas farmers have established aesthetically pleasing vegetative barriers, also known as windbreaks or shelterbelts, along the perimeter of their agricultural lands to shelter crops from wind erosion (Andreu et al., 2009).

Considerable research has been conducted to establish types and species of shelterbelts; however, quantification of how and to what extent benefits of specific tree species affect agricultural lands is limited. Historically, early settlers of Kansas used Osage orange hedgerows (for land protection aside from wood source (Barnett and Burton, 1997)), and these species are still commonly found on Kansas farmlands. Although Osage orange is commonly used as a shelterbelt in Kansas, research on its aerodynamics is scarce. Additional evaluation of airflow and particle transport through a vegetation barrier is also needed.

1.2. Research Objectives

The overall goal of this study was to assess the effectiveness of vegetative barriers (artificial standing vegetation and Osage orange trees) as controls for wind erosion using experimental measurements and computational fluid dynamics (CFD) simulations. As shown in Figure 1.1, the specific objectives of this dissertation include the following:

1. Determine sand transport and sand abrasion along a simulated standing vegetation canopy;
2. Determine the porosity and drag of a single row of Osage orange barrier (*Maclura pomifera*);
3. Measure the effectiveness of Osage orange barrier in reducing dust;
4. Predict airflow through artificial standing vegetation; and
5. Predict airflow and particle collection through the Osage orange barrier.

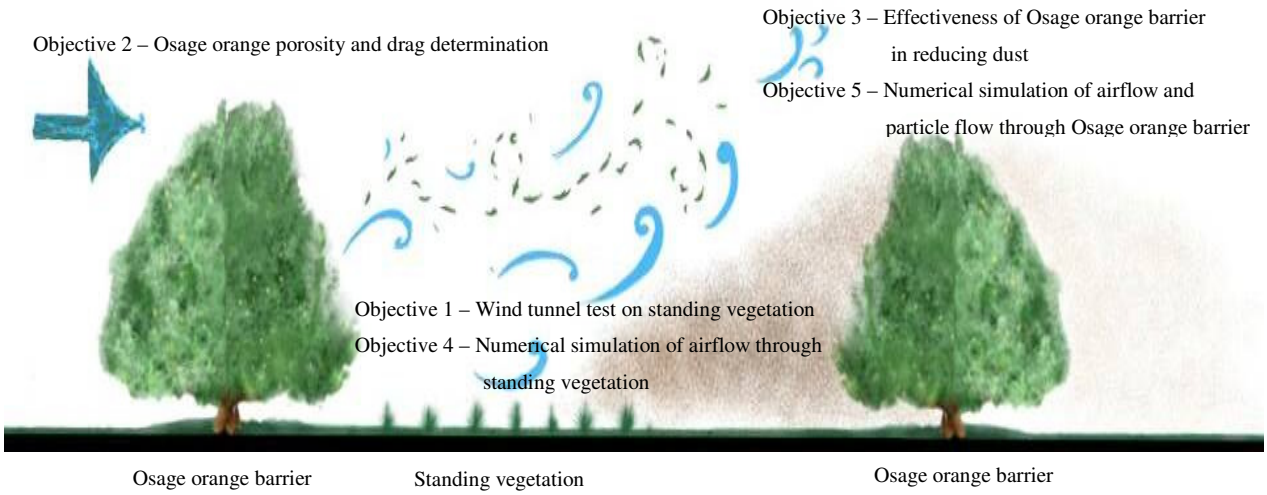

Figure 1.1. Research overview.

For standing vegetation, laboratory wind tunnel research was performed to observe the effects of abrasion and sand transport on land with sparse vegetation canopy (simulated by the insertion of artificial standing vegetation into a bed of quartz sand) (specific objective 1). In addition, open source computational fluid dynamics (CFD) software, OpenFOAM, was used to

model airflow through the simulated standing vegetation (specific objective 4). This open-source software eliminated the software costs of commercially available CFD packages.

For shelterbelts, this research addressed the Osage orange (*Maclura pomifera*) vegetative barrier commonly found in Kansas. The Osage orange species was chosen as the tree type for study because it satisfied the requirement of a "thin" shelterbelt (i.e., a shelterbelt in which wind variation throughout is negligible due to the small ratio of shelterbelt width to its height (Wilson, 2005; Bouvet et al., 2007)), which is essential for testing the applicability of optical porosity measurements to define aerodynamic properties of vegetative barriers. A single row of Osage orange served as an application of optical porosity determination (specific objective 2) and of dust control measurement (specific objective 4). Measured aerodynamic parameters were used as input values for numerical simulation of airflow and particle collection, using OpenFOAM, throughout the Osage orange vegetative barriers (specific objective 5).

The studies done in this dissertation provides technical information regarding the benefits of maintaining surface vegetation (i.e., abrasion impacts, wind speed reduction, and saltation discharge) and establishing vegetative barriers (i.e., wind speed reduction, dust concentration reduction) for preventing wind erosion. The aerodynamics of Osage orange barrier in two different stages of foliage (leaf-on and leaf-off) will be helpful to scientists, engineers, and landowners in providing technical information regarding the benefits of the specific species of vegetative barrier against wind erosion. Experimental measurements of airflow and dust control combined with numerical simulation using OpenFOAM will serve as a basis of comparison and help develop future numerical simulation using different tree species.

1.3. Organization of Dissertation

This dissertation contains eight chapters. Chapter 1 states the objectives and significance of the research. Chapter 2 is a review of literature on wind erosion and strategies of wind erosion mitigation using surface vegetation cover and vegetative barriers. Chapter 3 describes the effects of abrasion on artificial standing vegetation at various configurations in the wind tunnel. Chapter 4 presents aerodynamic measurements (optical and aerodynamic porosities, effective drag coefficients, and wind profiles) for the Osage orange barrier. Chapter 5 details the effectiveness of the Osage orange barrier in reducing particle concentration downwind of the barrier. Chapter 6 contains numerical simulation of airflow through the artificial standing vegetation, and Chapter 7 contains numerical simulation of air and particle flow through the Osage orange barrier taken as a porous region. Chapter 8 includes conclusions and recommendations for future work.

1.4. References

Barnett, J.P., & Burton, J.D. 1997. Osage orange: A pioneering stewardship species. *Tree Planters' Notes*. 48(3-4): 81-86.

Bouvet, T., Loubet, B., Wilson, J.D., & Tuzet, A. 2007. Filtering of windborne particles by a natural windbreak. *Boundary-Layer Meteorol.* 123: 481-509.

Wilson, J.D. 2005. Deposition of particles to a thin windbreak: The effect of a gap. *Atmos. Environ.* 39: 5525-5531.

CHAPTER 2 - Literature Review

2.1. Wind Erosion Problem

According to estimates of the United States Department of Agriculture Natural Resources Conservation Service (USDA NRCS) compiled for the National Resources Inventory (NRI) (USDA NRCS, 2007), the most significant wind erosion problems have been recorded in the Great Plains region, as shown in Figure 2.1. Kansas is located in the Northern Plains, a region in which estimates show large contribution to wind erosion.

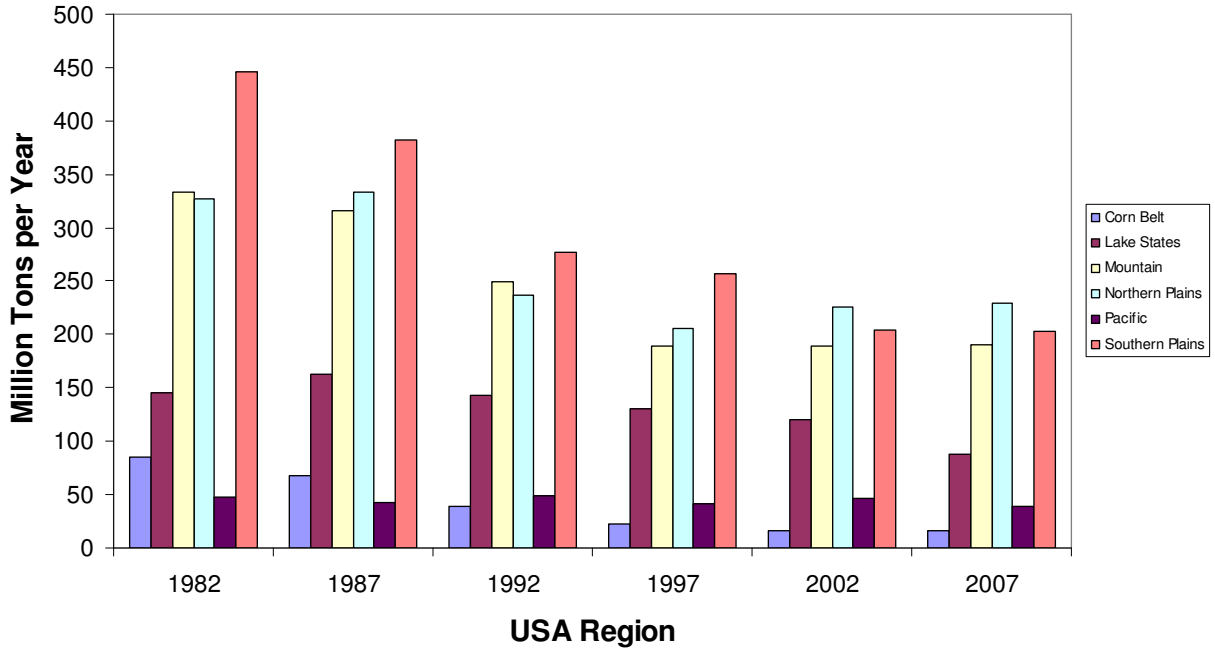

Figure 2.1. Wind erosion estimates for agricultural lands from 1982 to 2007 in the United States (USDA NRCS, 2007).

2.1.1. Factors Affecting Wind Erosion

Factors such as vegetation cover (Wolfe and Nickling, 1993; Lancaster and Baas, 1998; Li et al., 2007), climatic factors (Chepil et al., 1962; Wang et al., 2006), soil structural factors (Zobeck, 1991; Larney and Bullock, 1994), and cultural factors (Smith and English, 1982) affect the occurrence of wind erosion. Vegetation cover refers to the amount of soil cover due to crops and stubble available to minimize effects of wind erosion and are responsible for altering the soil microclimate, thus affecting the heat and water transport (Flerchinger et al., 2003) to the soil surface and soil susceptibility to wind erosion.

Meteorological parameters such as precipitation, wind speed, evaporation, and temperature comprise the relevant climatic factors. Soil dryness, controlled by the amount of precipitation and evaporation through soil moisture control, also contributes to soil vulnerability to erosion. According to a study by Fécan et al. (1999), increased threshold wind velocity for soils in arid and semi-arid regions can be attributed to soil moisture (i.e., the drier the soil, the less tendency to form aggregates, leading to increased erodibility as evidenced by a lower threshold wind velocity). Soil aggregate sizes are affected by the amount of soil moisture, but are heavily dependent on current temperature of the soil (i.e., high temperatures dry out the soil, thereby reducing aggregate sizes and increasing soil susceptibility to wind erosion (Webb and Strong, 2011). In addition, wind erosion is influenced by wind speed; the greater the wind speed, the more soil surface particles are potentially eroded.

Soil texture is classified as a soil structural factor that affects wind erosion. The ability of soils to form clods and soil looseness are soil structure parameters (Belnap and Gillette, 1998). Sandy soils are loose soils that are more prone to wind erosion compared to cloddy soils or soils that form large aggregates, such as loam soils. Sandy soils are coarse-textured, lacking in clay

and silt components that bind particles together to form aggregates. However, loams, silt loams, and clay loams have sufficient silt and clay components that form aggregates which are resistant to wind erosion. Particle size at the surface is an important soil property that dictates soil surface vulnerability to wind erosion. Different particle size ranges that dictates the soil wind erosion processes (i.e., creeping, saltation, suspension) occurring was discussed in detail by Saxton et al. (1999). Creeping is a process where large soil particles move through surface creeping; saltation is a process that occurs close to the surface and carries particles or lift to a certain distance with hopping movement of soil particles due to wind which causes entrainment and subsequent particle transport at the soil surface (Raupach and Findlater, 1993); and suspension is a process that carries particles farther distances away from source (Raupach et al., 2001). Although silt and clay more readily form aggregates when the soil is moist, thereby minimizing soil vulnerability to saltation, dry conditions favor soil particle release and tendency to undergo saltation even if wind speed is low. Sandy soils require greater wind speed than other soil types to initiate saltation or movement of particles, but they are more susceptible to wind erosion because of their looseness and low aggregate stability (Belnap and Gardner, 1993; Belnap and Gillette, 1997) compared to silt and clay, which form aggregates when water content is high in the soil.

Cultural factors correspond to the types and methods of cultivation, field orientation, field size, and wind barrier use. Higher tendency of wind erosion occurs over a smooth, wide, non-vegetated surface as compared to a surface that is "rough," as defined by the presence of ridges, large aggregates, or residue cover that tend to reduce the effects of wind erosion. Field size contributes to wind erosion by providing an ample space in which the "avalanche effect" can occur (likened to a snow avalanche where soil volume increases as a result of soil aggregates

rapidly rolling across the soil surface as wind sweeps through the surface) (Fryrear and Saleh, 1996). The avalanche causes additional soil particles to be carried away by the wind over a farther distance. Tillage, animal, and machine actions affect the soil surface by intervening with surface roughness such as ridge formations, soil clods, and soil aggregates. Repeated tillage (especially with use of tandem disks, offset disks, and harrows) pulverizes and smooths dry soils, consequently increasing soil susceptibility to wind erosion (Nordstrom and Hotta, 2004). The type of tillage implemented in an agricultural land could influence roughness of the soil surface as dictated by sizes of soil aggregates that are formed (López et al., 1998; Zhang et al., 2004). Investigation of the relationship between aerodynamic roughness and aggregate size of cultivated soil by Zhang et al. (2004) showed that large soil clods caused a decrease in the value of the roughness length parameter (z_0), thereby minimizing wind erosion. An investigation by Betteridge et al. (1999) on the effects of animal treading on the soil surface showed that compaction due to animal hooves smooths the surface, making the soil more vulnerable to wind erosion. Hamza and Anderson (2005) verified that traffic and a large number of machinery passes within an area of agricultural land increased soil susceptibility to wind erosion by wind, proving that soil compaction results from overuse of machinery in croplands.

2.1.2. Effects of Wind Erosion

Wind erosion has many ecological impacts and is a concern for croplands because it causes loss of soil nutrients (Gomes et al., 2003). Studies have shown the amount of nutrients lost through wind erosion by comparing remaining nutrients in the soil surface after wind erosion (Larney et al., 1998; Nuberg 1998; Sudmeyer and Scott 2002).

Wind erosion also negatively affects evapotranspiration within the soil. If the soil is subjected to high winds, increased temperature, and low humidity, moisture stress is demonstrated by shallow rooted crops and vegetables, consequently preventing the photosynthetic process due to closure in stomata, leading to crop wilting (Andreu et al., 2009). Khan et al. (2015) showed that dust deposition caused by wind erosion reduced the yield, stomatal conductance, photosynthesis, and evapotranspiration within the leaf and increased the leaf temperature of cotton.

For sparse vegetation, high wind speeds cause significant physical abrasion (Hagen and Casada, 2013). Young crops or small crops (seedlings) (Baker et al., 2009) and flowering stages of some crops (Brandle et al., 2004) are prone to damage caused by abrasion. Abrasion to crops also causes contamination and quality reduction of fruits and vegetables.

2.1.3. Control Strategies for Wind Erosion

Wind erosion minimization ultimately requires reduced surface wind speed and increased soil surface resistance (Funk and Riksen, 2007). Control strategies such as crop diversity and crop rotation (Vomocil and Ramig, 1976), crop residues (Siddoway et al., 1965), sprinkler systems (Cary et al., 1975), strip cropping (Chepil, 1957), no-till (Thorne et al. 2003), trap strips, annual crop barriers (Fryrear, 1963), sparse vegetation (Wolfe and Nickling, 1993), vegetative barriers (Ticknor, 1988), manure application (Woodruff et al., 1974), and treated sewage sludge (Koda and Ozinski, 2011) are employed to alleviate wind erosion problems. However, these practices depend on economics that govern use of such control practices in addition to the interest and perception of farmers and/or landowners.

According to Guan et al. (2003), shelterbelts can be classified as artificial (e.g., fences and thin screens), termed as "non-thickness" barriers in aerodynamics analysis, and vegetative (e.g., trees and shrubs), termed as barriers that possess internal structure and width.

2.2. Use of Vegetation as a Wind Erosion Control Strategy

Protecting soil fertility and crop yield is the primary goal of sparse vegetation on the soil surface. McGowan and Ledgard (2005) stated that vegetation is the most significant factor for minimizing wind erosion. They enumerated effects of vegetation as a factor for: (1) reducing sediment availability for transport by covering the soil; (2) lowering wind velocity below the threshold for sediment transport by absorbing ground level wind momentum; (3) filtering airborne sediments and protecting vegetation to prevent sediments from being re-entrained; and (4) lowering the near-surface wind speed and increasing dust deposition rate by increasing fluid drag in the air. Namikas and Sherman (1995) and Eldridge and Leys (2003) stated that alteration of soil and atmospheric properties, such as soil structural stability and near-surface air moisture through the presence of vegetation, could also minimize wind erosion. A vegetative barrier is a row of vegetation that shelters the downwind portion of the land from wind (Heisler and DeWalle, 1988), dust (Liu et al., 2013), or snow (Greb and Black, 1971).

2.2.1. Effects of Using Vegetation

2.2.1.1. Effects on Micrometeorology

The compound effect of changes in wind direction, wind speed, temperature, relative humidity, and air turbulence due to the presence of barriers drastically alters the plant, soil, and aerial conditions (Campi et al., 2009). Scattering and diffusion of solar radiation by vegetative

barriers (limited by barrier height) could also be important for promoting improved photosynthetic processes that yield healthier crops (Skidmore, 1976). Vegetative barriers' control of thermal radiation losses (within the vicinity of the barrier) could cause a warm environment for forage crops during the night (and possible prevention of frost incidences) and cool conditions during the day, thereby promoting less evapotranspiration and less moisture loss from soil surface, causing faster germination, growth rate, and more efficient use of water by plants (Cleugh, 1998; Zhu, 2008).

Downwind air temperatures are dictated by a combination of effects, such as barrier height (Skidmore, 1976) and eddy zones, within the vicinity of the barrier (Woodruff et al., 1959). Warm zones were found to exist near the barrier and at the soil surface where they originate; these zones are predicted by multiples of barrier height (occurring from 5H to 10H downwind of the barrier, where H is the average height of the barrier). Changes in microclimate within the barrier vicinity are results of reduced vertical air diffusion and mixing, which cause cooler nighttime and warmer daytime air temperatures (Skidmore et al., 1972).

Humidity was found to vary significantly due to combined effects of air mixing, diffusion, radiation, wind speed, air temperature, soil moisture, and evapotranspiration (Van Eimern et al., 1964). Marshall (1967) found that unsheltered and sheltered areas did not show significant changes in relative humidity.

2.2.1.2. Effects on Soil Characteristics

In relation to microclimate, changes in soil characteristics and ambient conditions above the soil surface are the major contributors to improved yield of crops due to controlled and efficient light, moisture, and nutrient exchanges between the soil and the plant. Improved protection against wind erosion that lessens or prevents crop damage also contributes to

increased crop yield (Kort, 1988). Factors such as crop type, shelterbelt design, soil properties, and management practices should be considered to achieve increased yield and crop quality (Brandle et al., 2004). Stoeckeler (1962) asserted that the maximum amount of land occupied by shelterbelts within an area should be 5% of the total area, and Ivanov (1984) stated that the maximum amount of land shelterbelts should occupy was 4% to provide ample sheltering effect. Many studies have described the downwind distance where land is effectively protected by vegetative barriers to be at 10H (Brenner et al., 1995; Cleugh et al., 2002; Vigiak et al., 2003; Cornelis and Gabriels, 2005). Although shelterbelts are advantageous as control for wind erosion, other studies (Lyles et al., 1984; Kessler, 1992; Mayus et al., 1999) have noted that shelterbelts compete for soil water, nutrients, and crop space.

2.2.1.3. Aesthetic Benefits

Preservation of crop yield and crop health is the most important factor for farmers, but improvement of landscapes and aesthetic value of a field also contributes to the establishment of vegetative barriers. Burel and Baudry (1995) discussed the maintenance of greenways (i.e., land networks that provide ecological, recreational, cultural, and historical benefits) with a focus on visual, scenic, and aesthetic values of hedgerows in landscape planning as well as benefits of vegetative barriers to animals.

A classification of shelterbelts was studied to determine visual impacts of shelterbelts in Iowa. Grala et al. (2010) found that 73% of 1,500 farmers and 2,000 non-farmers agreed that shelterbelts were necessary for visual diversification, while 67% those surveyed agreed that lands with shelterbelts are more visually appealing than lands without shelterbelts. Their study showed that approximately 59% of respondents (primarily non-farmers) considered conducting recreational activities (e.g., watching birds, wildlife) within landscapes with shelterbelts. Their

study also showed that farmers preferred conifers as the shelterbelt species and non-farmers preferred mixed conifers and hardwoods. In addition, the presence of shrubs alongside trees within rows of shelterbelts was preferred by non-farmers. Overall, farmers showed more interest in productivity benefits of shelterbelts that affect economics, such as operational costs in farms, while non-farmers are more focused on aesthetics and opportunities for recreation.

2.2.1.4. Effects on Animal Welfare

Vegetative barriers can also provide habitat, food, and shelter to many types of animals (i.e., livestock, wildlife, aquatic organisms) (Ffolliott, 1998). Mader et al. (1999) reported that shade provided by vegetative barriers improved cattle performance in the summer, especially when the cattle are not yet acclimated to hot weather. Their study also showed that cattle response was prominent during the first year of being subjected to the effects of vegetative barriers, but the effect of barriers decreased over the subsequent two years once the cattle become acclimatized. However, as heat load is minimized, cattle productivity increased and cattle health improved, potentially leading to avoidance of cattle deaths, especially during extremely hot weather conditions.

For wind erosion purposes, vegetative barriers can be useful for livestock protection in open areas, as discussed by Gregory (1995). Although the study mentioned disadvantages of vegetative barriers, such as (a) lower capacity of stock due to less grazing area, (b) reduction in herbage, (c) soil compaction, (d) creation of a habitat for pests that could poison the stock, and (e) risk of trapping stock during extreme weather conditions, these disadvantages could be generally controlled so that the advantages would far exceed the disadvantages of use of vegetation in pasture lands.

2.2.1.5. Improvement of Air Quality

The state of Kansas produces large amounts of livestock (i.e., beef cattle, swine, and poultry) and, as a consequence, Kansas experiences air quality problems such as dust, ammonia, odors due to volatile organic compounds (VOCs), and greenhouse gases (GHGs) that emanate from large commercial feedlots. To minimize odor problems, vegetative barriers have been established around the perimeter of these feedlots. Studies have shown the efficiency of these barriers in odor dissipation (Tyndall and Colletti, 2007).

Another study enumerated the effects of vegetative barriers on GHG mitigation. Kulshreshtha and Kort (2009) identified improvements caused by the presence of vegetation, such as carbon sequestration within trees, farm land area reduction that effectively reduces the source of GHG emissions (e.g., farm machinery), more efficient heating and cooling of nearby human and livestock houses, and provision for alternative fuel sources such as woody biomass.

Vegetative barriers can also reduce harmful agricultural or spray drifts that remain immediately following application of chemicals, including herbicides, fungicides, and insecticides, that could negatively affect human and animal health and the environment (Coye, 1985). Wenneker et al. (2005) discussed the benefits of natural shelterbelts for reducing chemical drift from orchard spray, and Ucar and Hall (2001) conducted an extensive review of the use of shelterbelts in pesticide drift mitigation.

Previous studies (Chepil, 1957; Stoeckeler, 1962; Hagen and Skidmore, 1971; Plate, 1971; Heisler and DeWalle, 1988; Ticknor, 1988; Loeffler et al., 1992; Raupach et al., 2001; Brandle et al., 2004; Cornelis and Gabriels, 2005; Tuzet and Wilson, 2007; Buccolieri et al., 2009) have established that the primary use of vegetative barrier is to minimize wind erosion, especially in sandy, erosive soils and arid and semi-arid regions. Vegetative barriers primarily

reduce wind speed below the threshold for erodible soils, thereby suppressing dust generation and suspension and lowering health risks associated with dust emission (Dockery et al., 1993; Saxton et al., 1999; Pope et al., 2002; Gilmour et al., 2006).

2.2.2. Design Considerations of Vegetative Barriers

The initial step prior to vegetative barrier design is determination of the prevailing wind direction at the location of the agricultural land. Tamang et al. (2009) stated that barriers placed perpendicular to the wind promote the greatest sheltering efficiency. They also suggested that if the wind comes from every direction, an enclosed system of vegetative barriers surrounding the target area is appropriate.

Barrier height is another important characteristic for consideration of vegetative barrier design. Cleugh et al. (2002) stated that reduction of wind speed downwind of the barrier is achieved up to a distance of 10 to 30 times the height of the barrier (10H - 30H). Tamang et al. (2009) added that if multiple species of trees are present (representing different heights), the tallest species dictates the extent of sheltering efficiency. According to Dong et al. (2010), this sheltering efficiency is dependent on the downwind distance to which wind velocity is reduced below the minimum required for saltation (effective shelter distance), wind velocity, and state of turbulence within the area under study.

Barrier width should also be considered in such a way that it will not exceed approximately 10H or else wind speed reduction is no longer effective because the wind flow behaved similarly to a forest with considerable reduction in wind speed (Straight and Brandle, 2007). Yusaiyin and Tanaka (2009) came to the same conclusion by investigating the effects of varying shelterbelt width on the values of drag force and bulk drag coefficients using wind tunnel tests and validating results using numerical modeling. They found a nonlinear increase in

drag force with increased shelterbelt width. They also found that effective sheltering existed up to a distance of 10H - 15H downstream.

The most important vegetative barrier characteristic that determines sheltering efficiency is porosity, sometimes referred to as density for vegetative barriers. Barrier porosity is dependent on the arrangement of trunks, branches, and leaves, thereby presenting a complex geometry because of three-dimensionality of each component (Straight and Brandle, 2007). Porosity can be categorized in two ways: aerodynamic porosity (α_p) and optical porosity (β_p). Aerodynamic porosity or volumetric porosity is the true porosity based on the complete three-dimensionality of vegetative barriers, and is a parameter that is difficult to compute (Yusaiyin and Tanaka, 2009). On the other hand, β_p is limited to a two-dimensional (2D) approximation of the true porosity. Straight and Brandle (2007) defined β_p as the background space visible through the barrier, consequently considering only the 2D geometry of the vegetative barrier (USDA-NAC, 2007). The two porosities differ in values, especially for broad-leaved vegetative barriers (Vigiak et al., 2003), but for thin and narrow barriers, value of true porosity is approximated by β_p (Heisler and DeWalle, 1988). As porosity increases, the barrier allows more wind to pass through, thereby lowering reduction in wind speed but causing less turbulence downwind and effectively increasing the distance protected by the barrier. However, if porosity decreases, the opposite phenomena are true; therefore, optimal α_p of vegetative barriers was recommended to be at values within 0.35 - 0.45 (Loeffler et al., 1992).

The long-term objective of research of various types of shelterbelts is to provide a foundation for optimal design of shelterbelts based exclusively on crop protection (Lyles et al., 1984, Norton, 1988; Kowalchuk and de Jong, 1995; Wilson, 1997; Boldes et al., 2001; Campi et al., 2009), animal welfare protection (Bird et al., 2002; Sanford et al., 2003), human and

household protection (Raupach, 2000; Lin et al., 2006), wind erosion protection (Funk et al, 2004; Gregory et al., 2004; Dong et al., 2010; Bao et al., 2009), transportation and facilities protection (Scanlon et al., 2000), and agricultural spray interception (Ucar and Hall, 2001; Mercer, 2009). However, Cable (1999) stated that nonagricultural shelterbelt benefits such as wildlife habitat (Johnson and Beck, 1988), fuel wood, recreation, and aesthetics must be considered as distinct from agricultural benefits, such as erosion control, increased crop yield, livestock protection, and snow control (Iversen, 1981; Shaw, 1988) and improved energy use in cooling/heating of nearby housing structures (DeWalle and Heisler, 1988; Swistock et al., 2005).

2.2.3. Determination of Optical Porosity of Vegetative Barriers

Geometric characteristics of trees largely influence the efficiency of vegetative barriers with respect to particle collection and wind speed reduction (Lee et al., 2010). The height of trees (Van Eimern et al., 1964; Loeffler et al., 1992), length of trees (Mulhearn and Bradley, 1977; Loeffler et al., 1992), width of shelterbelts (Van Eimern et al., 1964; Loeffler et al., 1992), and shelterbelt susceptibility to airflow (porosity) are examples of geometric characteristics of trees. Aerodynamic porosity is the ratio of airflow that passes through barrier pores ("through flow") and diverges over the barrier ("diverged flow"), thereby making porosity a measure of minimum wind speed and position at which the wind recovers speed (Vigiak et al., 2003). Raine and Stevenson (1977) defined aerodynamic porosity as the ratio of pore space to the occupied space of tree stems, twigs, leaves, and branches, as well as a factor that affects the shelter extent and reduction of wind speed leeward of shelterbelts.

Because of the complexity of living shelterbelt geometry, measurement of α_p poses a great challenge to researchers (Kenney, 1987). Development of techniques to determine living

shelterbelt porosity has progressed. Detection principles such as volume and density (porosity) can be employed to deduce geometric characteristics of trees. The current techniques include image analysis, stereoscopy photography, light spectrum analysis, infrared thermograph, ultrasonic sensors, and laser sensors such as the light detection and ranging (LiDAR) (Palacin et al., 2007). Use of the individual techniques varies according to cost of instrumentation required to obtain parameters that enable the user to determine β_p and/or α_p.

2.2.4. Airflow through Barriers

The presence of wind barriers influences airflow upwind, within, and downwind of the barrier. These three locations correspond to three stages of the effect of wind barriers on airflow. Airflow changes abruptly upwind of the barrier, causing a change in the microclimate (surface-plant-air level) and soil climate that differs from the airflow observed in the open field, such as intermittent changes in heat and water vapor transport (Cleugh, 1998; Campi et al., 2009). The altered soil climate and microclimate causes a different response for the sheltered area downwind.

As shown in Figure 2.2, approach flow is determined by the stability of atmospheric conditions and aerodynamic roughness of the upwind portion of the field. If the upwind portion of the field is relatively flat and sparsely vegetated or without vegetation, the approaching flow may transport dust or particulate matter (PM) (particle-bearing flow) as induced by soil wind erosion processes such as saltation and suspension. The effects on the approach flow is important in determining the type or species of tree necessary to render protection downwind from deposition of particles carried by wind.

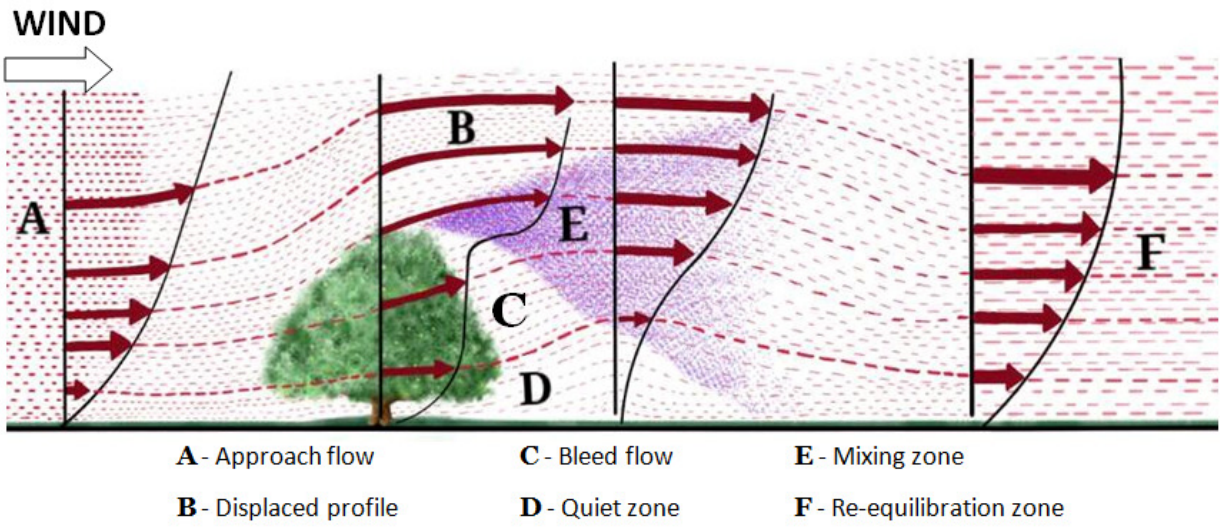

Figure 2.2. Airflow regimes around a shelterbelt positioned normal to airflow (adapted from: Judd et al., 1996).

Various airflow regimes were described by Judd et al. (1996) and illustrated in Figure 2.2. A majority of air flows through the top of a shelterbelt (magnitude determined by porosity of the wind barrier), as shown in the deflection of streamline in Figure 2.2, denoted as displaced profile B. An immediate increase in wind speed is caused by the presence of barrier in this region, thereby satisfying the requirement for flow continuity.

The wind barrier exerts a force on the wind via the drag it creates which is compensated by a loss of momentum in the air. This loss of momentum corresponds to a reduction in wind speed, as shown in the bleed flow region C in Figure 2.2. Drag exerted by the barrier is converted to wind speed reduction necessary for wind erosion sheltering, thereby decreasing the wind's tendency to transport surface particles immediately downwind of the barrier, through quiet zone D in Figure 2.2. Region D in the figure is the sheltered area in which minimum wind speed occurs; the length of this region is determined by the porosity of the wind barrier. Although decreasing barrier porosity increases barrier drag, wind barriers with the greatest drag

are not necessarily the most effective barriers. Woodruff et al. (1963) determined that vegetative barriers may be too dense or too porous to be effective shelters from wind erosion. Excessive drag on wind barriers (corresponding to low porosities) causes minimum downwind wind speeds close to the barriers, but these wind speeds tend to recover their magnitude more quickly than wind speeds downwind of more porous wind barriers. Mixing zone E in Figure 2.2 is a turbulent layer of air that occurs at a distance greater than 10H and eventually develops into an equilibrium zone F, a region that re-establishes the wind profile of approach flow A).

Figure 2.3 illustrates the process when assumingly uniform particles that occupy a height greater than the barrier are carried by approach flow A from Figure 2.2. Depending on the porosity of the barrier, some particles are filtered throughout the height of the wind barrier, corresponding to particle deposition on wind barrier elements (e.g., leaves, trunk, branches). As shown in Figure 2.3, no change in particle concentration is observed in the displaced region B (described in Figure 2.2). Particle concentration is reduced in the bleed flow region C (described in Figure 2.2) due to particle filtering by the wind barrier that, in addition to reduction in wind speed, reduces the amount of particle deposition on the downwind sheltered region or quiet region D (described in Figure 2.2) caused by wind speed reduction in the region. As the distance away from the wind barrier increases, particle concentration recovery occurs at the mixing layer E (described in Figure 2.2), eventually reaching the value of its initial particle concentration (approach flow A concentration).

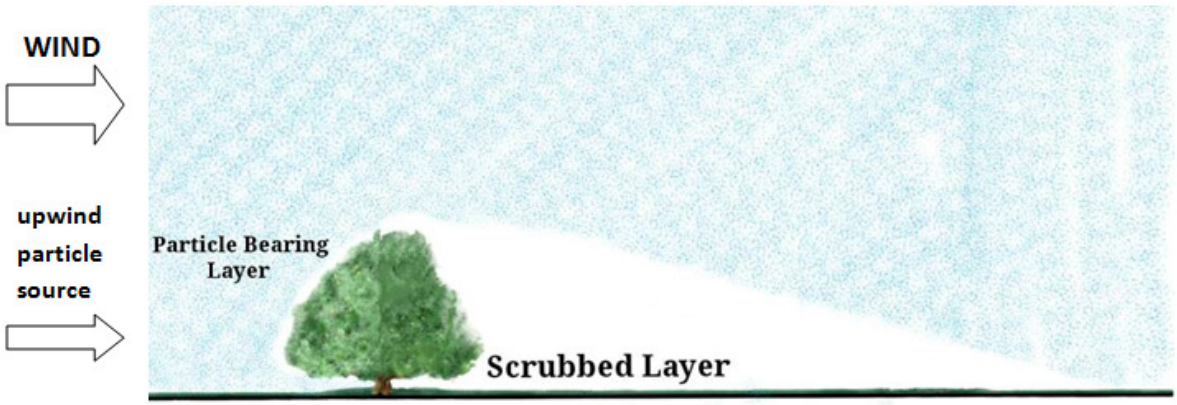

Figure 2.3. Wind barrier protection from deposition (adapted from: Raupach et al., 2001).

2.2.5. Research on Vegetation as Wind Erosion Control

2.2.5.1. Research on Sparse Vegetation

Buckley (1987) studied effects of wind on aeolian dunes by using a wind tunnel to simulate the natural vegetation pattern of erect, spread, and rounded herbaceous dune plants. Threshold velocities were predicted by the value of vegetation cover with which the sand transport was also dependent (i.e., the higher the vegetation cover, the greater the threshold velocity that reduces the sand transported at the surface, where vegetation cover is defined as area covered by vegetation divided by total area).

Li et al. (2007) studied quantitative effects of vegetation cover on wind erosion. They found that grasses more effectively reduce wind erosion compared to sparsely distributed mesquites within the field. Their results also showed that aeolian flux increased throughout their three windy tests, thereby causing a 25% reduction of total organic carbon and nitrogen on the top 5 cm soil surface; approximately 60% of the reduction occurred during the first test.

Burri et al. (2011) evaluated the effects of various densities of Perennial ryegrass (*Lolium perenne*) compared to that of a bare sand configuration. Their study showed an exponential

decrease in mass flux of sand at the end of the tunnel as the canopy density increased. They also analyzed the vertical profile of sand discharge and found that minimal sediment fractions were recorded on heights below the canopy (< 10 cm), implying a more efficient trapping of particles within the canopy as compared to heights above the canopy (10 cm < h < 20 cm). The decrease in sand mass flux above the canopy height was found to be dependent on shear stress velocities (forces that lift particles as compared to forces related to gravity settling).

2.2.5.2. Research on Vegetative Barriers

2.2.5.2.1. Wind Tunnel Measurements on Vegetative Barriers

Guan et al. (2003) studied shelterbelt drag across model trees in a wind tunnel. They used narrow, realistic models for wind tunnel data acquisition, and they proposed the following empirical relationship between β_p and α_p: $\alpha_p = \beta_p^{0.4}$. They also determined a relationship between drag coefficient and optical porosity, $C_D = C_{D0}(1 - \beta_p^{1.8})$, where C_{D0} is the zero-lift drag coefficient that is a constant equal to 1.08. In their study, denser canopies resulted in a smaller difference between values of α_p and β_p.

Bitog et al. (2011) conducted a wind tunnel experiment in which a black pine tree (*Pinus thunbergii*) was used to determine α_p and resistance factor of a tree shelterbelt. They found that mean porosities for one, two, and three trees at various tree densities were 0.91, 0.69, and 0.42, respectively, and drag coefficients were 0.55, 0.82, and 1.08, respectively.

2.2.5.2.2. Field Measurements on Vegetative Barriers

Grant and Nickling (1998) evaluated wind drag on artificial trees on a farm. They placed artificial Scots pine Christmas trees in a flat, grassy field (sod farm) and measured wind drag. They also used cup anemometers for wind speed determination and developed a relationship

between β_p (determined using photogrammetry) and α_p (determined using water displacement technique), which was found to be $\beta_p = {\alpha_p}^{2.782}$, where the exponent for β_p was 0.4, similar to 0.36 in the study by Guan et al. (2003). Their study predicted that the equation is different with various species of vegetation and that the exponent is dependent on leaf structure and depth to width ratio of the barrier. Taylor's (1988) C_D value of 0.6 agreed well with observed C_D values of surface-mounted cone and cylinders in their experiment although C_D values of the model Scots pine trees were close to twice the magnitude (approximately 1 to 1.6) to that of the cone and cylinders.

Nelmes et al. (2001) proposed a simple approach of measuring sheltering efficiency of Hawthorn hedges. They used two cup anemometers connected to data loggers that measured wind speed. Data acquisition was based on wind tunnel experiment optimization to gather information on optimal upstream and downwind locations for their anemometers and evaluate the velocity ratio parameter, *s*, which is a ratio of downstream to upstream total turbulent kinetic energy in the horizontal wind component. They found that the interpolated *s*-value from wind tunnel experiments ranged from 0.4 to 0.5, while field measurements showed a value of 0.46.

Tuzet and Wilson (2007) studied the effects of tall Cyprus hedges on wind flow. Profiles and transects were found to be qualitatively consistent with available literature profiles and showed promise for predicting behavior in relatively less ideal regimes for dense shelterbelts. They also observed that minimum wind speed of approximately 20-25% of the upwind value not affected by changes in wind speed direction and thermal stratification occurred at a distance 0.25H downwind from the shelterbelt.

2.2.5.2.3. Numerical Simulation of Vegetative Barriers

Schwartz et al. (1995) studied a model of forage sorghum in various configuration patterns with β_p ranging from 7 to 39%. They placed four rows of sorghum 1 m apart in a wind tunnel patterned to their field measurements. Results revealed a logarithmic profile at distances <0.2H windward and ≥4H leeward of sorghum model with porosities greater than 30%. In addition, wind speed tended to decrease or remain at a consistent magnitude as barrier porosity decreased up to 20% since no increase or decrease in wind speed was recorded at porosity values below 20%.

Hipsey et al. (2004) studied the effects of shelterbelt types (artificial and natural) on evaporation in small agricultural reservoirs near barriers. In their developed model, they deduced that wind speed was minimized above the water surface due to shelterbelts that effectively reduced evaporation on these water bodies by 15 to 25 % (artificial shelterbelts) and 28% (natural shelterbelts).

Gromke and Ruck (2008) evaluated C_D of small artificial tree-like structures in a wind tunnel and modeled the airflow to create simulations for various configurations. They varied crown porosities of the tree-like structures by imposing various types of crown materials as models, and they tested their effects on C_D, which were evaluated in a wind tunnel with velocities of 5 m s^{-1} to 14 m s^{-1}. Observed C_D values for the materials were 1 to 1.2 (wood wool), 0.8 to 1.1 (sisal fiber), and 0.9 to 1.0 (foam 10 pores per inch (p.p.i)). C_D were found to be velocity dependent at wind speed values of 5 m s^{-1} to 14 m s^{-1}. Compared to naturally occurring coniferous and deciduous trees, C_D values corresponded to wind speeds less than 10 m s^{-1}.

Buccolieri et al. (2009) simulated the effects of avenue-like trees planted along urban street canyons by comparing numerical simulation results using porous obstacles such as lattice

cages of known porosity, as detailed in Gromke and Ruck (2009). They used various crown porosities and stand densities in the model within simulated buildings to assess the effects of these parameters on perpendicular pollutant and air flow. Findings showed that the ratio of width of canyon street to building height (W/H) indicated pollutant accumulation at the pedestrian level, where larger values of W/H caused less effect of pollutant concentration at low wind speeds and slight suppression of pollutants due to trees subjected to high wind speeds.

Mercer (2009) modeled spray drift capture efficiency using three vegetation models [d_e = 1 mm (pine), d_e = 10 mm (intermediate), d_e = 50 mm (poplar)] with three droplet diameters (20, 50, and 100 μm). Results showed that efficient droplet capture occurs with β_p between 0.1 and 0.4, with optimal capture at 0.25. The pine model showed the largest capture efficiency, but droplet diameters less than 20 μm were not captured at all, and diameters greater than or equal to 100 μm were well-captured or settled out of the flow.

Salim et al. (2011) used FLUENT (2010) software for Large Eddy Simulation (LES) of dispersion and flow of street traffic pollutants to compare an unoccupied street canyon to a street canyon with trees planted with pore volume of 96%. They found increased concentrations of pollutants at the leeward side of street canyons with trees, as evidenced by a decrease in air ventilation, or momentum sink, within tree crowns.

Rowing competitions inspired Ferreira (2011) to study and determine optimal shelterbelts to protect a long channel area within the vicinity of rowing events. In the study, a wind tunnel equipped with model trees resembling Lombary poplars (*Populus nigra*) were placed on one row in the field site and bamboo or canes were placed for another row of shelterbelt. Various combinations with different β_p were investigated, and results determined that optimal wind conditions with nearly constant wind speed across the channel row were attained using a single

row of poplar trees (crown β_c = 60% and trunk β_t = 87%) downwind of the bamboo row (β_p = 35%).

2.2.6. Osage Orange (Maclura pomifera)

For the purposes of this study, a thin windbreak, defined as a shelterbelt in which wind variation was negligible due to the small ratio of shelterbelt width to its height (Wilson, 2005; Bouvet et al., 2007), was selected to allow validation of aerodynamic parameters (e.g., optical porosity) using numerical modeling in accordance with suggestions by various authors (Tiwary et al., 2005; Raupach et al., 2001; Wilson, 2005).

Osage orange is historically native to southern Oklahoma, a limited region in Arkansas, and parts of east Texas. However, in an exploration in 1673, Jacques Marquette and Louis Joliet discovered Osage orange trees in Osage Indian villages located on what is now southern Missouri, Arkansas, eastern Kansas, and Oklahoma. This species of tree proved to be very useful for early settlers of the United States as source of wood, shade, and protection (Barnett and Burton, 1997). In addition, native Indians used the branches for bows that were superior weapons for fighting and hunting. These bows were so precious that a barter transaction for a bow would cost a horse and a blanket. The characteristic strength of the bows prompted the French explorers to call the Osage orange trees bois d'arc, meaning "wood of the bow." With increased knowledge of the durability and strength of Osage orange trees, settlers realized that the trees were great sources of timber for anything that required hard, low-shrinkage wood. Osage orange trees constituted the rims and hubs of farm wagons because the wood could withstand heavy loads while maintaining flexibility to be bent into a circle. Osage orange tree wood was also found to be a good "shock absorber" without splitting or cracking and the trees were highly resistant to rot, allowing utilization for structures such as railroad ties, telephone poles, mine timber, street

paving blocks, bridge pilings, tool handles, and treenails. Consequently, vast harvesting of Osage orange trees occurred in parts of Texas, Arkansas, and Oklahoma for the purpose of selling the wood wholesale.

Averaging approximately 9.1 m in height upon maturation (Harrar and Harrar, 1962), Osage orange trees were eventually determined to be substantial field borders because they can contain livestock within the field without providing excessive shade for the crops. Between 1865 and 1939, approximately 64,000 km of Osage orange hedgerows were planted by private landowners in Kansas, and a majority of those durable Osage orange trees still serve as vegetative barriers for parts of Kansas. The Osage orange tree species paved the way for agricultural settlement because early settlers used hedges of Osage orange to fence out the animals for farming (Barnes, 1960).

2.3. Numerical Modeling Using CFD

CFD is a process of discretization and conversion of differential equations that govern transport of mass, momentum, and energy to their algebraic equation equivalent which are easily solved and are helpful in facilitating numerical solutions using computers (Figure 2.4). The inception of CFD occurred during the advent of computing technology during the 1960s. However, CFD did not become a significant component of study areas specializing in engineering problem solutions until the 1970s when emerging programming languages became the foundation for the creation of commercial software packages.

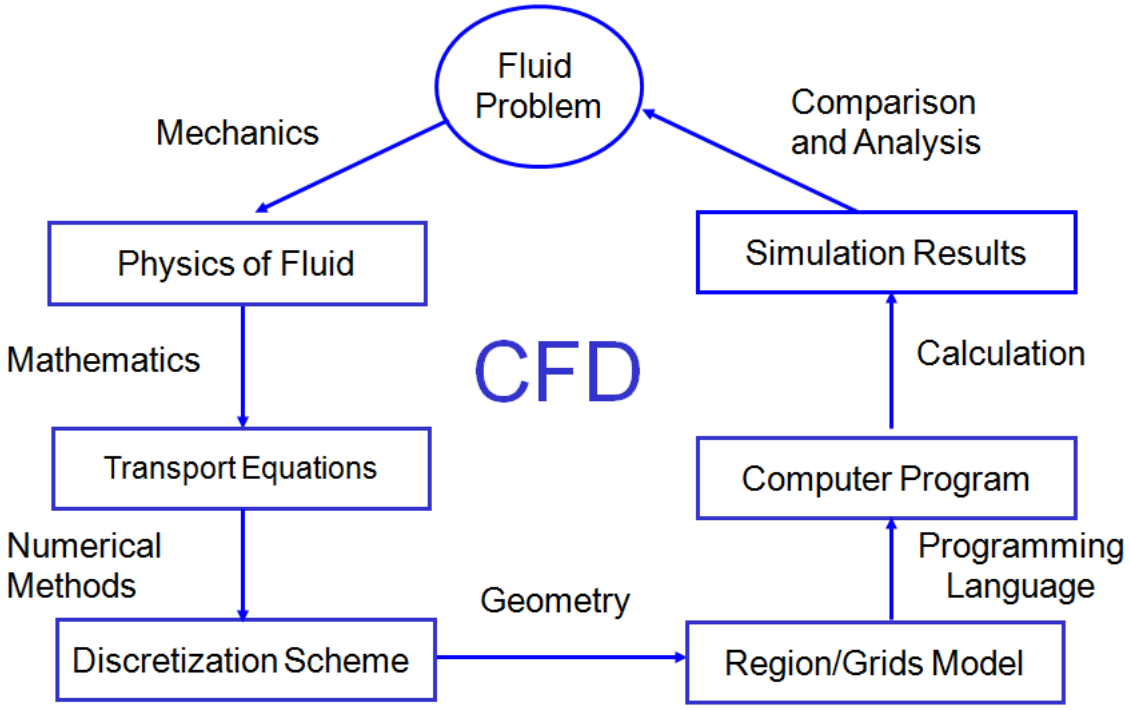

Figure 2.4. CFD process (Zuo, 2005).

What really made CFD special was it is more economical than performing actual experiments to provide essential information to an engineer for a solution to a specific problem (Date, 2005). During the past three decades, the application of CFD to engineering problems became prominent (Lee et al., 2013) and a necessity due to the requirement of "scaling" (a process of ensuring similarity of results despite the difference in size parameters (Krishna and van Baten, 2002), i.e., laboratory size reactors vs. commercial size reactors) from laboratory use of equipment towards use at the industrial scale. Not only did the scaling impose difficulty in design but it also increased uncertainty as to whether the large scale equipment was feasible or not. With this situation, CFD became useful in identifying and applying proper scaling laws to ensure geometric, kinematic, and dynamic similarities between models (pilot-scale) and the full-scale equipment.

2.3.1. Turbulence Modeling

Turbulence is a measure of disorderliness in fluid flows. Almost every naturally occurring flow that is disturbed is considered turbulent. A general form for the transport equation of mass, momentum, and energy can be written as follows (Predicala and Maghirang, 2003; Patankar, 1980):

$$\frac{\partial}{\partial t}(\rho\phi) + \frac{\partial}{\partial x_i}(\rho u_i \phi) - \frac{\partial}{\partial x_i}\left[\Gamma_\phi \frac{\partial \phi}{\partial x_i}\right] = S_\phi \tag{2.1}$$

where ρ is air density, ϕ is the transported fluid property (e.g., mass, momentum, energy), u_i is the velocity component in the x_i direction, i is the subscript that represents three directions (x, y, and z), Γ_ϕ is the diffusion coefficient, and S_ϕ is the source term. Terms on the left side of equation are accumulation, convection, and diffusion terms for ϕ. A detailed definition of Γ_ϕ and S_ϕ was presented by Predicala and Maghirang (2003).

Bonifacio (2013) described intermediate steps for deriving the Reynolds-Averaged Navier-Stokes (RANS) equation, the basis for turbulence models (e.g., k-ε model, k-ω model). The resulting RANS equation upon derivation is as follows:

$$\rho \frac{\partial \overline{u_J}}{\partial t} + \frac{\partial}{\partial x_i}\left(\rho\, \overline{u_i u_J}\right) = -\frac{\partial \bar{P}}{\partial x_j} + \frac{\partial}{\partial x_i}\left(\overline{\tau_{iJ}} - \rho\, \overline{u_i' u_J'}\right). \tag{2.2}$$

The average viscous stress component given by Ferziger and Peric (2002) was

$$\overline{\tau_{iJ}} = \mu\left(\frac{\partial \overline{u_J}}{\partial x_i} + \frac{\partial \overline{u_i}}{\partial x_j}\right) \tag{2.3}$$

where i is the subscript for all three directions (x, y, and z), j is the subscript for the evaluated direction (x, y, or z), P is evaluated pressure force in the j-direction, τ_{ij} is the viscous stress component, and μ is the dynamic air viscosity (Glasgow, 2010). Bars on Eqs. 2.2 and 2.3 are

average component values resulting from use of the Reynolds decomposition method. The continuity equation is given by (Bitog et al., 2012; Rosenfeld et al., 2010)

$$\frac{\partial \overline{u_i}}{\partial x_i} = 0 \tag{2.4}$$

Another commonly used two-equation RANS-based model is the Re-Normalization Group (RNG) *k*-ε model. This model is given by the following equations (Yeh et al., 2010; Bitog et al., 2012):

$$\frac{\partial}{\partial x_i}(\rho k u_i) = \frac{\partial}{\partial x_j}\left[\alpha_k \mu_{eff} \frac{\partial k}{\partial x_i}\right] + G - \rho\varepsilon \tag{2.5}$$

$$\frac{\partial}{\partial x_i}(\rho \varepsilon u_i) = \frac{\partial}{\partial x_j}\left[\alpha_\varepsilon \mu_{eff} \frac{\partial \varepsilon}{\partial x_i}\right] + C_{1\varepsilon}\frac{\varepsilon}{k}(G) - C_{2\varepsilon}^{*}\rho\frac{\varepsilon^2}{k} \tag{2.6}$$

$$G = 2\mu_t S_{ij} S_{ij} \tag{2.7}$$

where S_{ij} is the shearing-rate tensor and μ_t is the turbulent viscosity.

$$C_{2\varepsilon}^{*} = C_{2\varepsilon} + C_{2\varepsilon}' \tag{2.8}$$

$$C_{2\varepsilon}' = \frac{C_\mu \rho \eta^3 (1-\eta/\eta_0)}{1+\beta\eta^3} \tag{2.9}$$

$$\mu_t = \rho C_\mu \frac{k^2}{\varepsilon} \tag{2.10}$$

$$\eta = S\frac{k}{\varepsilon} \tag{2.11}$$

$$S = \sqrt{2S_{ij}S_{ij}} \tag{2.12}$$

$$k = \frac{3}{2}\left(V_{avg} I\right)^2 \tag{2.13}$$

where V_{avg} is average velocity, I is turbulence intensity, and k is turbulence kinetic energy ($m^2\ s^{-2}$).

$$\varepsilon = C_\mu^{3/4}\frac{k^{3/2}}{\ell} \tag{2.14}$$

where ε is turbulence dissipation rate ($m^2\ s^{-3}$).

Many studies have found the RNG $k-\varepsilon$ model to be the most applicable turbulence model for investigating complex wind flows around barriers (Lee and Lim, 2001; Packwood, 2000; Lee et. al., 2007; Li et al., 2007; Santiago et al., 2007; Bourdin and Wilson, 2008; Yeh et al., 2010; Bitog et al., 2012).

2.3.2. Governing Equations

2.3.2.1. Airflow through Artificial Standing Vegetation

Airflow through standing vegetation is three-dimensional (3D). As such, equations are based on 3D RANS steady-state, incompressible, isothermal assumptions for the airflow and the turbulent atmospheric layer was taken as neutrally stratified (Guo and Maghirang, 2012). The continuity equation (2.4) and momentum conservation equation (Cheng et al., 2003; Endalew et al., 2009) are given as

$$\frac{\partial u_i u_j}{\partial x_j} = -\frac{1}{\rho}\frac{\partial p}{\partial x_i} + \frac{1}{\rho}\frac{\partial}{\partial x_j}\mu\left(\frac{\partial u_i}{\partial x_j} + \frac{\partial u_j}{\partial x_i}\right) - \frac{\partial}{\partial x_j}\left(\overline{u_i' u_j'}\right) \tag{2.15}$$

2.3.2.2. Airflow through Porous Barrier

Representation of vegetative barriers as porous zones requires the addition of a sink term to the Navier-Stokes equation, resulting in the following:

$$\frac{\partial}{\partial t}(\gamma \rho u_i) + u_j \frac{\partial}{\partial x_j}(\rho u_i) = -\frac{\partial p}{\partial x_i} + \mu \frac{\partial \tau_{ij}}{\partial x_j} + S_i \tag{2.16}$$

The sink term in Eq. 2.16 accounts for the reduction of wind momentum due to vegetative barriers, which is the pressure loss within the vicinity of the canopy (Guo and Maghirang, 2012; Bitog et al., 2012).

2.3.2.3. Particle Collection through Porous Barrier

For the simulation of particle collection and airflow, the convection-diffusion equation for a passive scalar is implemented, modified to account for dispersion turbulence, given by the following equation (Takano and Moonen, 2013):

$$\frac{\partial C}{\partial t} = -\bar{u}_i \frac{\partial C}{\partial x_i} + \frac{\partial}{\partial x_i}\left[\left(D + \frac{\nu_t}{Sc_t}\right)\frac{\partial C}{\partial x_i}\right] \tag{2.17}$$

where C is concentration, D is diffusivity, ν_t is turbulent kinematic viscosity, and Sc_t is the turbulent Schmidt number. Tominaga and Stathopoulos (2007) conducted an evaluation of the effects of values of turbulent Schmidt numbers for various types of flow fields and it was found that a value of 0.63 is desirable in numerical modeling and comparison with experimental results.

2.3.3. Open-source Field Operation and Manipulation (OpenFOAM)

CFD software is widely used in engineering because it allows the end user to solve transport phenomena problems, mathematical problems, and electromagnetic problems. As shown in Figure 2.5, OpenFOAM is structured to include preprocessing and post-processing utilities and allow customization of numerical solvers to solve problems in continuum mechanics. This software is coded under the object oriented C++ programming language.

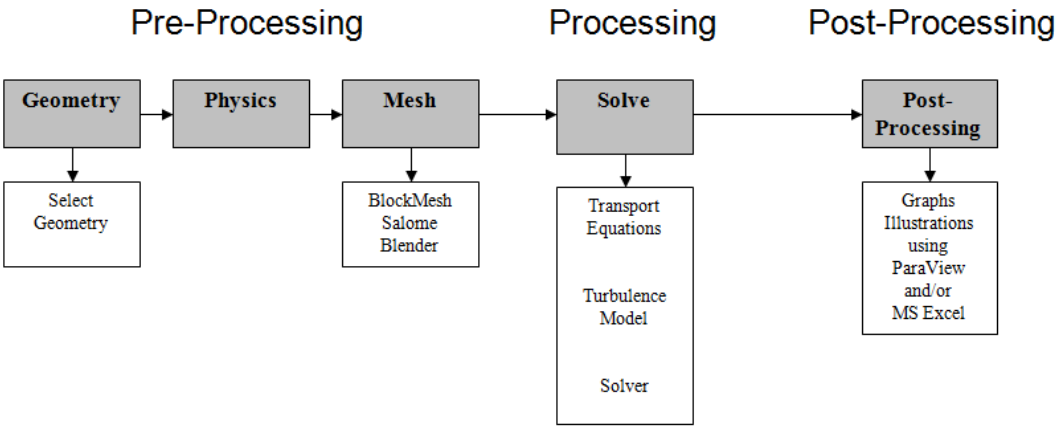

Figure 2.5. OpenFOAM structure (Date, 2005; OpenCFD, 2011).

OpenFOAM contains built-in geometry, a meshing tool (blockMesh and snappyHexMesh), and a post-processing tool (ParaView) to enable animation of computed results. Included in the C++ library is the ability of OpenFOAM to convert mesh from other software packages (e.g., Blender, Salome). The advantages of OpenFOAM include its versatility for solver capabilities in which numerous built-in example modules are readily available based on the type of solution required (e.g., incompressible flows, compressible flows, multiphase flows, electromagnetics, solid dynamics) and the option of customizing available solvers that fulfill needs of the end user. Although OpenFOAM requires knowledge of programming in C++, the user is not required to be an expert in programming the language as long as the basics of C++ are known.

Representation of equations in OpenFOAM resembles the original differential equation given in the following comparisons (OpenCFD Ltd., 2011):

Differential equation: $$\frac{\partial \rho U}{\partial t} + \nabla \cdot \varphi U - \nabla \cdot \mu \nabla U = -\nabla p \quad (2.18)$$

OpenFOAM representation (written in C++ code):

```
Solve
(
        fvm::ddt(rho,U)
    +   fvm::div(phi,U)
    -   fvm::laplacian(mu,U)
        ==
    -   fvc::grad(p)
);
```

OpenFOAM is run in a Linux-based system (also an open-source operating system (OS) environment) such as the ones readily available to download (Ubuntu, Fedora, and OpenSUSE). For Windows OS users, the virtual machine option that runs Linux as an interface is an option that enables the user to download and run OpenFOAM in Windows. Unfortunately, limited documentation is available for OpenFOAM, thereby requiring the evaluation of already-available solvers for use in various types of transport phenomena problems and modification of those solvers based on user needs. Practiced use of the various solvers is essential to increase knowledge of numerical modeling using OpenFOAM and to learn and document processes and options tweaked within the solver libraries.

2.3.3.1. OpenFOAM Preprocessing

The OpenFOAM structure includes a tool for creating simple geometries and meshing the computational domain using blockMesh. For complex geometries derived from third-party software, snappyHexMesh is desirable. Both blockMesh and snappyHexMesh are encoded in C++. Several third-party software packages (commercial and open-source), including the Salome, are available for creating base computer-aided design (CAD) geometry.

Use of blockMesh requires creation of geometry with deeper understanding of the code that creates the geometry because blockMesh is not a graphical interface friendly tool of creating geometries where shapes are ready to be inserted and that only measurements are required for input. In OpenFOAM, blockMesh is essential for creating the entire computational domain to prepare and set up computation boundaries. After the entire domain for simulation is created, barrier geometry is inserted within the entire domain using the snappyHexMesh tool, which combines the entire block domain and the barrier geometry and then creates the mesh necessary for computation. Because compatible formats of files are necessary for snappyHexMesh to run,

the American Standard Code for Information Interchange (ASCII) STereoLitography (.STL) file format was used for this study (other format could be Object (.OBJ) file format) (OpenCFD Ltd., 2011).

If investigation using checkMesh command reveals that a bad mesh is created, ParaView allows the user to review the faces that is problematic during mesh creation using a command within OpenFOAM that converts skewed faces into Visualization ToolKit (.VTK) file formats that are read through ParaView for easier manipulation. This then allows the user to manually fix the face, which is very tedious and cumbersome, or be advised regarding adjustments of the snappyHexMesh file.

2.3.3.2. OpenFOAM Processing

Numerical computation for OpenFOAM requires three folders (i.e., 0, constant, system) to execute a specific type of case (Bonifacio et al., 2014). The 0 folder contains initial and boundary conditions for computation. The constant folder contains files that define the geometry and boundary of the domain, barrier geometry (.STL files included), Reynolds-averaged stress (RAS) modeling properties that define cellzones considered porous, and type of turbulence modeling to be used. The system folder dictates how computation is done, how long computation lasts, and the number of iterations. Depending on the case, the three folders require unique files.

2.3.3.3. OpenFOAM Post-Processing

Simulation results can be shown in various types of media: photos, figures, graphs, and movies. OpenFOAM can be manipulated by operating and creating presentation types depending on user needs and requirements. Post-processing can be done in Paraview for the simulation, meshing, and streamline illustrations; graphs can be created using pyFoam (a python library

available for illustration of OpenFOAM data) and Microsoft Excel (Microsoft Corp., Redmond, WA). pyFoam can also be used during the processing/computation stage to monitor and visualize residual values for epsilon and kappa and pressure during iteration steps of the computation. This can help predict whether or not convergence is achieved (Hidalgo et al., 2014).

2.3.3.4. Simulations Using OpenFOAM

Simulation results using commercially available CFD software products have been widely documented (Parsons et al., 2004; Riddle et al., 2004; Bitog et al., 2011; Guo and Maghirang, 2012) and far outweigh the number of simulations done using OpenFOAM because a significant amount of time and effort are necessary to learn the basics of OpenFOAM and to extend use of the software to complex problems (Silva and Lage, 2011). However, many fluid fluid dynamicists use OpenFOAM because of its availability. As a result, OpenFOAM is increasing in popularity and is perceived to be cost-effective for end users.

Zhang et al. (2011) evaluated various types of open-source CFD software, including their own CFD-WindModel (WEM) based on Stam's (2003) source code. Zhang et al. (2011) also compared other CFD software, such as the Gerris project by Popinet (2003) and OpenFOAM. In their study, OpenFOAM offered the widest perspective in terms of power to solve fluid dynamics problems and better accuracy compared to the results offered by CFD-WEM and Gerris. The simplicity of CFD-WEM was encouraging even though it is still in raw development and could only be used in limited numerical simulation applications. The Gerris project failed to offer solutions to problems involving RANS implementation.

Lysenko et al. (2013) analyzed and validated flows through a bluff-body using OpenFOAM and Ansys FLUENT. The study involved laminar and turbulent flows across circular and triangular cylinders in which performance of the solvers in OpenFOAM were

evaluated and compared to simulation results of Ansys FLUENT and experimental data. Comparable results between OpenFOAM and Ansys FLUENT were obtained by comparing results of numerical simulation using various types of turbulence models. Solutions obtained by the two types of software were independent of the grid size, an essential finding that enables users to adapt OpenFOAM as a less expensive option than commercially available CFD software.

Higuera et al. (2013) used OpenFOAM with RANS modeling to evaluate many coastal engineering processes. Their study focused on the generation of realistic waves (i.e., wave run-up, breakage, and tow current) and validation of surface water hydrodynamics that were measured and compared between laboratory and simulation results. The κ-ω shear stress turbulence (SST) model was the basis for numerical analysis, and the simulation ran for a reasonable time despite the presence of a complex and large-case scenario.

Takano and Moonen (2013) conducted flow simulation over buildings with slanted roofs. Various shapes of roof within the buildings were considered to determine their effects on pollutant dispersion. Behavior differences of flow regime within roof configurations were taken into account. Single-vortex and two-vortex regimes within the roof depths with air flow showed contrasting results such that higher pollutant concentrations were found near the surface of the roof for the two-vortex regime, while pollutant concentration decreased for the single-vortex as the slope of the roof increased.

Bonifacio et al. (2014) compared the results of AERMOD to CFD using OpenFOAM for simulating particle transport from a ground-level source. They found that both methods had similar responses to wind speed and atmospheric stability effects, although downwind particle concentrations were lower for AERMOD than CFD. Height was found to be a variable for

predicting particle concentration using CFD instead of AERMOD, which showed no effects along the height gradient.

2.4. Summary

Wind erosion has long been a significant problem in arid and semi-arid states in the Great Plains, especially during hot, dry periods with increased wind intensity. Many studies have addressed this problem and many management practices have been developed to alleviate the effects of wind erosion. Establishment of vegetative barriers is a common, economical practice for controlling wind erosion for agricultural lands. In Kansas, the Osage orange (*Maclura pomifera*) deciduous tree species is widely used for vegetative barriers, but limited research is available regarding the benefits of wind erosion control in the aerodynamics perspective. Although many studies have focused on the effectiveness of vegetative barriers for combating wind erosion, quantification of the effectiveness of specific species of tree has been limited. To date, a documented account of Osage orange aerodynamics has not been provided.

CFD provides a cost-effective method of research in the aerodynamics perspective. Although many commercially available software products have been used in many types of field studies, increasing demand of CFD for aerodynamics research has caused increasing popularity inexpensive open-source alternative products.

2.5. References

Aggarwal, C.C. 2013. *Outlier analysis*. New York: Springer Science + Business Media.

Andreu, M.G., Tamang, B., Friedman, M.H., & Rockwood, D.L. 2009. The benefits of windbreaks for Florida growers. FOR192. Gainesville: University of Florida Institute of

Food and Agricultural Sciences. Available at: https://edis.ifas.ufl.edu/pdffiles/FR/FR25300.pdf. Accessed January 10, 2014.

Angelopoulou, E. & Wright Jr., J.R. 1999. Laser scanner technology. Technical Report MS-CIS-99-16. GRASP Laboratory, University of Pennsylvania, Philadelphia: PA. Available at http://repository.upenn.edu/cgi/viewcontent.cgi?article=1083&context=cis_reports&sei-redir=1#search="types laser scanner". Accessed 10 August 2011.

Baker, J.T., McMichael, B.L., Burke, J.J., Ephrath, J., Gitz, D.C., & Lascano, R.J. 2009. Sand abrasion injury and biomass partitioning in cotton seedlings. *Agron. J.* 101(6): 1297-1303.

Bao Y., Li, H., & Yang, J. 2009. Effects of shelterbelts on wind erosion control in the desertified cropland of north-western Shandong Province, China. In *Bioinformatics and Biomedical Engineering, (iCBBE) 2011 5th International Conference.* 10-12 May, Wuhan, China.

Barnes, L. 1960. An editor looks at early-day Kansas. *Kansas Historical Quarterly* 26: 267-301.

Barnett, J.P., & Burton, J.D. 1997. Osage orange: A pioneering stewardship species. *Tree Planters' Notes*. 48(3-4): 81-86.

Basher, L.R. & Painter, D.J. 1997. Wind erosion in New Zealand. Proceedings of the International Symposium on Wind Erosion, Manhattan, Kansas, 3-5 June 1997, USDA-ARS, Manhattan. Available at http://www.weru.ksu.edu/symposium/proceed.htm. Accessed 21 May 2011.

Bayraktar E., Mierka O., & Turek, S. 2012. Benchmark computations of 3D laminar flow around a cylinder with CFX, OpenFOAM and FeatFlow. *Int. J. Comput. Sci. Eng.* 7(3): 253–266.

Belnap, J., & Gardner, J.S. 1993. Soil microstructure of the Colorado Plateau: the role of the cyanobacterium *Microcoleus vaginatus*. *Great Basin Naturalist* 53: 40-47.

Belnap, J., & Gillette, R.J. 1997. Disturbance of biological soil crusts: Impacts on potential wind erodibility of sandy desert soils in Southeastern Utah. *Land Degrad. Dev.* 8: 355-362.

Belnap, J. & Gillette, R.J. 1998. Vulnerability of desert biological soil crusts to wind erosion: the influences of crust development, soil texture, and disturbance. *J. Arid Environ.* 39(2): 133-142.

Betteridge, K., MacKay, A.D., Shepherd, T.G., Barker, D.J., Budding, P.J., Devantier, B.P., & Costal, D.A. 1999. Effect of cattle and sheep treading on surface configuration of a sedimentary hill soil. *Aus. J. Soil Sci.* 37: 743-760.

Bielders, C.L., Michels, K., & Rajot, J.L. 2000. On-farm evaluation of ridging and residue management practices to reduce wind erosion in Niger. *Soil Sci. Soc. Am. J.* 64: 1776-1785.

Bird, P.R., Jackson, T.T., & Williams, K.W. 2002. Effect of synthetic windbreaks on pasture growth in south-western Victoria, Australia. *Aus. J. Exp. Agri.* 42(6): 831-839.

Bisal, F. 1968. Influence of plant residue on sand flow in a wind tunnel. *Can. J. Soil Sci.* 48(1): 49-52.

Bitog, J.P., Lee, I.B., Hwang, H.S., Shin, M.H., Hong, S.W., Seo, I.H., Mostafa, E., & Pang, Z. 2011. A wind tunnel study on aerodynamic porosity and windbreak drag. *Forest Sci. Tech.* 7(1): 8-16.

Bitog, J.P., Lee, I.B., Hwang, H.S., Shin, M.H., Hong, S.W., Seo, I.H., Kwon, K.S., Mostafa, E., & Pang, Z. 2012. Numerical simulation study of a tree windbreak. *Biosys. Eng.* 111(1): 40-48.

Boldes, U., Colman, J., & Marañon Di Leo, J. 2001. Field study of the flow behind single and double row herbaceous windbreaks. *J. Wind Eng. Ind. Aerodyn.* 89(7-8): 665-687.

Bonifacio, H.F., Maghirang, R.G., & Glasgow, L.A. 2014. Numerical simulation of transport of particles emitted from ground-level area source using AERMOD and CFD. *Eng. Appl. Comp. Fluid Mech.* 8(4): 488-502.

Bourdin, P. & Wilson, J.D. 2008. Windbreak aerodynamics: Is computational fluid dynamics realiable? *Boundary Layer Meteorol.* 126: 181-208.

Bouvet, T., Loubet, B., Wilson, J.D., & Tuzet, A. 2007. Filtering of windborne particles by a natural windbreak. *Boundary Layer Meteorol.* 123: 481-509.

Bowker, G.E., Gillette, D.A., Bergametti, G., Marticorena, B., & Heist, D.K. 2008. Fine-scale simulations of aeolian sediment dispersion in a small area in the northern Chihuahuan Desert. *J. Geophys. Res.* 113(F02S11): 1-12.

Brandle, J.R., Hodges, L., & Zhou, X.H. 2004. Windbreaks in North American agricultural systems. *Agroforestry Sys.* 61: 65-78.

Brenner, A.J., Jarvis, P.G., & van den Beldt, R.J. 1995. Windbreak-crop interactions in the Sahel. 1. Dependence of shelter on field conditions. *Agri. Forest Meteorol.* 75(4): 215-234.

Buccolieri, R., Gromke, C., Di Sabatino, S., & Ruck, B. 2009. Aerodynamic effects of trees on pollutant concentration in street canyons. *Sci. Total Environ.* 407: 5247-5256.

Buckley, R. 1987. The effect of sparse vegetation on the transport of dune sand by wind. *Nature* 325: 426-428.

Burel, F. & Baudry, J. 1995. Social, aesthetic and ecological aspects of hedgerows in rural landscapes as a framework for greenways. *Landscape and Urban Planning* 33: 327-340.

Burri, K., Gromke, C., Lehning, M. & Graf, F. 2011. Aeolian sediment transport over vegetation canopies: A wind tunnel study with live plants. *Aeolian Res.* 3(2): 205-213.

Burtch, R. 2002. LiDAR Principles and application. In: *Proceedings of IMAGIN Conference, April 29-May 1, 2002.* IMAGIN Conference, Traverse City, MI, USA.

Cable, T.T. 1999. Nonagricultural benefits of windbreaks in Kansas. *Great Plains Res.* 9: 41-53.

Campi, P., Palumbo, A.D., & Mastrorilli, M. 2009. Effects of tree windbreak on microclimate and wheat productivity in a Mediterranean environment. *European J. Agron.* 30(3): 220-227.

Cardillo G. 2006. Holm-Sidak t-test: a routine for multiple t-test comparisons. http://www.mathworks.com/matlabcentral/fileexchange/12786

Cary, J.W., Kohl, R.A., Westerman, D.T., & Rickman, R.W. 1975. Row cropping sandy soils under sprinklers using a winter grain cover to control wind erosion. Idaho Agr. Exp. Sta. Bull. No. 549.

Cavanagh, J.E., Peyman, Z.R., & Wilson, J.G. 2009. Spatial attenuation of ambient particulate matter air pollution within an urbanised native forest patch. *Urban Fores. & Urban Greening* 8(1): 21-30.

Cheng, Y., Lien, F.S., Yee, E., & Sinclair, R. 2003. A comparison of large eddy simulations with a standard $k - \varepsilon$ Reynolds-averaged Navier-Stokes model for the prediction of a fully developed turbulent flow over a matrix of cubes. *J. Wind Eng.* 91: 1301-1328.

Chepil, W.S., Siddoway, F.H., & Armbrust, D.V. 1962. Climatic factor for estimating wind erodibility of farm fields. *J. Soil Water Conserv.* 17(4): 162-165.

Chepil W. S. 1957. Width of field strips to control wind erosion. *Kansas Agric. Exp. Stn., Tech. Bull.* 92. p. 16 Dec

Cleugh, H.A. 1998. Effects of windbreaks on airflow, microclimates, and crop yields. *Agrofores. Sys.* 41: 55-84.

Cleugh, H., Prinsley, R., Bird, R.P., Brooks, S.J., Carberry, P.S., Crawford, M.C., Jackson, T.T., Meinke, H., Mylius, S.J., Nuberg, I.K., Sudmeyer, R.A., & Wright, A.J. 2002. The Australian national windbreaks program: Overview and summary of results. *Aus. J. Exp. Agri.* 42(6): 649-664.

Cornelis, W.M. & Gabriels, D. 2005. Optimal windbreak design for wind-erosion control. *J. Arid Environ.* 61(2): 315-332.

Coye, M.J. 1985. The health effects of agricultural production: I. The health of agricultural workers. *J. Public Health Policy* 6(3): 349-370.

Creswell, H.P., Painter, D.J., & Cameron, K.C. 1991. Tillage and water content effects on surface soil physical properties. *Soil Till. Res.* 21: 67-83.

Date, A.W. 2005. *Introduction to computational fluid dynamics*. Cambridge University Press.

DeWalle, D. & Heisler, G. 1988. Use of windbreaks for home energy conservation. *Agri. Ecosys. Environ.* 22-23: 243-260.

Dockery, D.W., Pope III, C.A., Xu, X., Spengler, J.D., Ware, J.H., Ferris, B.G., & Speizer, F.E. 1993. An association between air pollution and mortality in six United States cities. *New England J. Med.* 329(24): 1753-1759.

Dong, Z., Luo, W., Qian, G., & Wang, H. 2010. Evaluating the optimal porosity of fences for reducing wind erosion. *Sciences in Cold and Arid Regions* 3(1): 0001-0012.

Dong, Z., Gao, S., & Fryrear, D.W. 2001. Drag coefficients, roughness length and zero-plane displacement height as disturbed by artificial standing vegetation. *J. Arid Environ.* 49(3): 485-505.

Eldridge, D.J. & Leys, J.F. 2003. Exploring some relationships between biological soil crusts, soil aggregation and wind erosion. *J. Arid Environ.* 53(4): 457-466.

Endalew, A.M., Hertog, M., Delele, M.A., Baetens, K., Persoons, T., Baelmans, M., Ramon, H., Nicolai, B.M., & Verboven, P. 2009. CFD modelling and wind tunnel validation of airflow through plant canopies using 3D canopy architecture. *Int. J. Heat Fluid Flow* 30: 356-368.

Farmer, A.M. 1993. The effects of dust on vegetation - A review. *Environ. Pollut.* 79(1): 63-75.

Fécan, F., Marticorena, B.. & Bergametti, G. 1999. Parameterization of the increase of the Aeolian erosion threshold wind friction velocity due to soil moisture for arid and semi-arid areas. *Ann. Geophysicae* 17: 149-157.

Ferreira, A. 2011. Structural design of a natural windbreak using computational and experimental modeling. *Environ. Fluid Mech.* 11: 517-530.

Ferziger, J.H. & Peric, M. 2002. *Computational Methods for Fluid Dynamics*. 3rd ed. Heidelberg. Germany: Springer-Verlag.

Ffolliott, P. 1998. Multiple benefits of arid land agroforestry home gardens and riparian ecosystems. In *Farming the forest for specialty products*. Proceedings of the Conference on Enterprise Development Through Agroforestry, ed., Josiah, S. J., 41-46. St. Paul, MN: Center for Integrated Natural Resources and Agriculture Management, University of Minnesota.

Flerchinger, G.N., Sauer, T.J., & Aiken, R.A. 2003. Effects of crop residue cover and architecture on heat and water transfer at the soil surface. *Geoderma* 116(1-2): 217-233.

Fryrear, D.W. 1963. Annual crops as wind barriers. *Trans. ASAE* 6: 340-342.

Fryrear, D.W., & Saleh, A. 1996. Wind erosion: Field length. *Soil Sci.* 161: 398-404.

Funk, R. & Riksen, M. 2007. Measures to reduce wind erosion and related dust emissions. Proceedings of the DustConf 2007 International Conference on Air Pollution, Maastricht,

The Netherlands, 23-24 April 2007. Available at http://www.dustconf.com/CLIENT/DUSTCONF/UPLOAD/S9/FUNK_D_P.PDF Accessed 23 May 2011.

Funk, R., Skidmore, E.L., & Hagen, L.J. 2004. Comparison of wind erosion measurements in Germany with simulated soil losses by WEPS. *Environ. Model. Softw.* 19(2): 177-183.

Genis, A., Vulfson, L., & Ben-Asher, J. 2012. Combating wind erosion of sandy soils and crop damage in the coastal deserts: Wind tunnel experiments. *Aeolian Res.* 9: 69-73.

Gilmour, I.M., Jaakkola, M.S., London, S.J., Nel, A.E., & Rogers, C.A. 2006. How exposure to environmental tobacco smoke, outdoor air pollutants, and increased pollen burdens influences the incidence of asthma. *Environ. Health Perspectives* 114(4): 627-633.

Glasgow, L.A. 2010. *Transport Phenomena.* Hoboken, NJ: John Wiley & Sons, Inc.

Gomes, L., Arŕue, J.L., López, M.V., Sterk, G., Richard, D., Gracia, R., Sabre, M., Gaudichet, A., & Frangi, J.P. 2003. Wind erosion in a semiarid agricultural area of Spain: the WELSONS project. *Catena* 52: 235-256.

Gonzales, H. B. 2010. Cattle feedlot dust – Laser diffraction analysis of size distribution and estimation of emissions from unpaved roads and wind erosion. MS Thesis. Manhattan, Kan.: Kansas State University.

Gonzales, H.B., Maghirang, R.G., Wilson, J.D., Razote, E.B., & Guo, L. 2012. Measuring cattle feedlot dust using laser diffraction analysis. *Trans. ASABE.* 54(6): 2319-2327.

Grala, R.K., Tyndall, J.C., & Mize, C.W. 2010. Impact of field windbreaks on visual appearance of agricultural lands. *Agrofores. Sys.* 80: 411-422.

Grant, P.F. & Nickling, W.G. 1998. Direct field measurement of wind drag on vegetation for application to windbreak design and modeling. *Land Degradation and Development* 9: 57-66.

Greb, B.W. & Black, A.L. 1971. Vegetative barriers and artificial fences for managing snow in the Central and Northern Plains. pp. 96-111. *In: Proc. Snow and Ice in Relation to Wildlife and Recreation Symposium*, A. O. Haugen (ed.), Ames, IA.

Greeley, R. & Iversen, J.D. 1985. *Wind as a geological process*. New York: Cambridge University Press.

Gregory, J.M., Wilson, G.R., Singh, U.B., & Darwish, M.M. 2004. TEAM: Integrated, process-based wind-erosion model. *Environ. Model. Softw.* 19(2): 205-215.

Gregory, N.G. 1995. The role of shelterbelts in protecting livestock: A review. *New Zealand J. Agri. Res.* 38: 423-450.

Gromke, C. & Ruck, B. 2008. Aerodynamic modelling of trees for small-scale wind tunnel studies. *Forestry* 81(3): 243-258.

Gromke, C. & Ruck, B. 2009. On the impact of trees on dispersion processes of traffic emissions in street canyons. *Boundary Layer Meteorol.* 131: 19-34.

Guan, D., Zhang, Y., & Zhu, T. 2003. A wind-tunnel study of windbreak drag. *Agri. Forest Meteorol.* 118: 75-84.

Guo, L. 2011. Measurement and control of particulate emissions from cattle feedlots in Kansas. PhD dissertation. Manhattan, Kan.: Kansas State University.

Guo, L. & Maghirang, R.G. 2012. Numerical simulation of airflow and particle collection by vegetative barriers. *Eng. Applic. Comp. Fluid Mech.* 6(1): 110-122.

Hagen, L.J. 2001. Assessment of wind erosion parameters using wind tunnels. In *Sustaining the Global Farm,* Scott D.E., Mohtar, R.H., Steinhardt G.C. (eds.), 10th International Soil Conservation Organization Meeting, Purdue University and USDA-ARS National Soil Erosion Research Laboratory, 1999; 742-746.

Hagen, L.J. & Casada, M.E. 2013. Effect of canopy leaf distribution on sand transport and abrasion energy. *Aeolian Res.* 10: 37-42.

Hagen L. & Skidmore, E. 1971. Windbreak drag as influenced by porosity. *Trans. ASABE* 14(3): 464-465.

Hall, D.J. & Upton, S.L. 1988. A wind tunnel study of the particle collection efficiency of an inverted frisbee used as a dust deposition gauge. *Atmos. Environ.* 22(7): 1383-1394.

Hamza, M.A., & Anderson, W.K. 2005. Soil compaction in cropping systems – A review of the nature, causes and possible solutions. *Soil Till. Res.* 82: 121-145.

Hassine, A.B. & Lutts, S. 2010. Differential responses of saltbush *Atriplex halimus L.* exposed to salinity and water stress in relation to senescing hormones abscisic acid and ethylene. *J. Plant Physiol.* 167(17): 1448-1456.

Harrar, E.S. & Harrar, G.J. 1962. *Guide to the southern trees*. 2nd ed. New York: Dover. 256-259.

Heisler, G. & DeWalle, D. 1988. Effects of windbreak structure on wind flow. *Agri. Ecosys. Environ.* 22-23: 41-69.

Hidalgo, V.H. Luo, X.W., Yu, A., & Soto, R. 2014. Cavitating flow simulation with mesh development using Salome open source software, In: *Proceedings of the 11th International Conference on Hydrodynamics*, pp. 1-8. 19-24 October, Singapore.

Higuera, P., Lara, J.L., & Losada, I.J. 2013. Simulating coastal engineering processes with OpenFOAM. *Coastal Eng.* 71: 119-134.

Hipsey, M.R., Sivapalan, M., & Clement, T.P. 2004. A numerical and field investigation of surface heat fluxes from small wind-sheltered waterbodies in semi-arid Western Australia. *Environ. Fluid Mech.* 4: 79-106.

Hyams, D.G. 2013. Curve expert 1.4 software. www.curveexpert.net

Ivanov, A.F. 1984. Shelterbelts in the Kulunda steppe. *Lesn. Khoz.* 1984(9): 41-43.

Iversen, J.D. 1981. Comparison of wind-tunnel model and full-scale snow fence drifts. *J. Wind Eng. Ind. Aerodyn.* 8(3): 231-249.

Johnson, R.J. & Beck, M.M. 1988. Influences of shelterbelts on wildlife management and biology. *Agri. Ecosys. Environ.* 22-23: 301-335.

Judd, M.J., Raupach, M.R., & Finnigan, J.J. 1996. A wind tunnel study of turbulent flow around single and multiple windbreaks, part I. Velocity fields. *Boundary Layer Meteorol.* 80(1-2): 127-165.

Kenney, W.A. 1987. A method for estimating windbreak porosity using digitized photographic silhouettes. *Agri. Forest Meteorol.* 39: 91-94.

Kessler, J.J. 1992. The influence of karité (*Vitellaria paradoxa*) and néré (*Parkia biglobosa*) trees on sorghum production in Burkina Faso. *Agrofores. Sys.* 17(2): 97-118.

Khan, S.Z., Spreer, W., Pengnian, Y., Zhao, X., Othmanli, H., He, X., & Mller, J. 2015. Effect of dust deposition on stomatal conductance and leaf temperature of cotton in Northwest China. *Water* 7: 116-131.

Koda, E. & Ozinski, P. 2011. Slope erosion control with the use of fly-ash and sewage sludge. *Ann. Warsaw Univ. of Life Sci. – SGGW, Land Reclam*. 43 (2): 101-111.

Kort, J. 1988. Benefits of windbreaks to field and forage crops. *Agri. Ecosys. Environ.* 22-23: 165-191.

Kowalchuk, T.E. & de Jong, E. 1995. Shelterbelts and their effect on crop yield. *Can. J. Soil Sci.* 75(4): 543-550.

Krishna, R., & van Baten, J.M. 2002. Scaling up bubble column reactors with highly viscous liquid phase. *Chem. Eng. Technol.* 25 (10): 1015-1020.

Kulshreshtha, S. & Kort, J. 2009. External economic benefits and social goods from prairie shelterbelts. *Agrofores. Sys.* 75: 39-47.

Lal, R. 2001. Soil degradation by erosion. *Land Degrad. Develop.* 12: 519-539.

Lancaster, N. & Baas, A. 1998. Influence of vegetation cover on sand transport by wind: Field studies at Owens Lake, California. *Earth Surface Proc. Landforms* 23: 69-82.

Larney, F.J. & Bullock, M.S. 1994. Influence of soil wetness at time of tillage and tillage implement on soil properties affecting wind erosion. *J. Soil Till. Res.* 29: 83-95.

Larney, F.J., Bullock, M.S., Janzen, H.H., Ellert, B.H., & Olson, E.C.S. 1998. Wind erosion effects on nutrient redistribution and soil productivity. *J. Soil Water Conserv.* 53: 133-140.

Lee, S.J. & Lim, H.C. 2001. A numerical study on flow around a triangular prism located behind a porous fence. *Fluid Dyn. Res.* 28: 209-221.

Lee, I.B., Sase, S., & Sung, S.H. 2007. Evaluation of CFD accuracy for the ventilation study of a naturally ventilated broiler house. *Japan Agri. Res. Quarterly* 41(1): 53-64.

Lee, K.H., Ehsani, R., & Castle, W.S. 2010. A laser scanning system for estimating wind velocity reduction through tree windbreaks. *Comp. Elec. Agri.* 73(1): 1-6.

Lee, I.B., Bitog, J.P., Hong, S.W., Seo, I.H., Kwon, K.S., Bartzanas, T., & Kacira, M. 2013. The past, present and future of CFD for agro-environmental applications. *Comp. and Elec. Agri.* 93: 168-183.

Li, J., Okin, G.S., Alvarez, L., & Epstein, H. 2007. Quantitative effects of vegetation cover on wind erosion and soil nutrient loss in a desert grassland of southern New Mexico, USA. *Biogeochem.* 85(3): 317-332.

Lin, X.J., Barrington, S., Nicell, J., Choinière, D., & Vézina, A. 2006. Influence of windbreaks on livestock odour dispersion plume in the field. *Agri. Ecosys. Environ.* 116(3-4): 263-272.

Liu, L., Guan, D., Peart, M.R., Wang, G., Zhang, H., & Li, Z. 2013. The dust retention capacities of urban vegetation – a case study of Guangzhou, South China. *Environ. Sci. Pollut. Res.* 20(9): 6601-6610.

Loeffler, A.E., Gordon, A.M., & Gillespie, T.J. 1992. Optical porosity and windspeed reduction by coniferous windbreaks in Southern Ontario. *Agro. Sys.* 17(2): 119-133.

López, M.V., Sabre, M., Gracia, R., Arrué, J.L., & Gomes, L. 1998. Tillage effects on soil surface conditions and dust emission by wind erosion in semiarid Aragon (NE Spain). *Soil Tillage Res.* 45: 91-105.

Lychenko, D.A., Ertesvåg, I.S., & Rian, K.E. 2013. Modeling of turbulent separated flows using OpenFOAM. *Comp. & Fluids* 80: 408-422.

Lyles, L. 1975. Possible effects of wind erosion on soil productivity. *J. Soil Water Conserv.* 30(6): 279-283.

Lyles, L. 1976. Wind patterns and soil erosion on the Great Plains. In *Shelterbelts on the Great Plains,* 22-30. R.W. Tinus, ed. Denver, Colo.: Great Plains Agric. Council Publishing.

Lyles, L. & Allison, B.E. 1981. Equivalent wind-erosion protection from selected crop residues. *Trans. ASAE.* 24(2): 405-408.

Lyles, L. & Allison, B.E. 1976. Wind erosion: The protective role of simulated standing stubble. *Trans. ASAE.* 19(1):61-64.

Lyles, L., Tatarko, J., & Dickerson, J.D. 1984. Windbreak effects on soil water and wheat yield. *Trans. ASAE 20: 69-72.*

Mader, T.L., Dahlquist, J.M., Hahn, G.L., & Gaughan, J.B. 1999. Shade and wind barrier effects on summertime feedlot cattle performance. *J. Anim. Sci.* 77(8): 2065-2072.

Marshall, J.K. 1967. The effect of shelter on the productivity of grasslands and field crops. *Field Crop Abstracts* 20: 1-14.

Marticorena, B., Bergametti, G., Gillette, D., & Belnap, J. 1997. Factors controlling threshold friction velocity in semiarid and arid areas of the United States. *J. Geophys. Res.* 102(D19): 23,277-23,287.

Maurer, T., Herrmann, L., & Stahr, K. 2010. Wind erosion characteristics of Sahelian surface types. *Earth Surf. Process. Landforms* 35: 1386-1401.

Mayus, M., Van Keulen, H., & Stroosnijder, L. 1999. A model of tree-crop competition for windbreaks systems in the Sahel: description and evaluation. *Agrofores. Sys.* 43: 183-201.

McGowan H. & Ledgard, N. 2005. Enhanced dust deposition by trees recently established on degraded rangeland. *J. Royal Soc. of New Zealand* 35(3): 269-277.

Mercer, G.N. 2009. Modelling to determine the optimal porosity of shelterbelts for the capture of agricultural spray drift. *Environ. Model. and Softw.* 24(11): 1349-1352.

Merrill, S.D., Black, A.L., Fryrear, D.W., Saleh, A., Zobeck, T.M., Halvorson, A.D., & Tanaka, D.L. 1999. Soil wind erosion hazard of spring wheat-fallow as affected by long-term climate and tillage. *Soil Sci. Soc. Am. J.* 63: 1768-1777.

Michels, K., Sivakumar, M.V.K., & Allison, B.E. 1995a. Wind erosion control using crop residue I. Effects on soil flux and soil properties. *Field Crops Res.* 40(2): 101-110.

Michels, K., Sivakumar, M.V.K., & Allison, B.E. 1995b. Wind erosion control using crop residue II. Effects on millet establishment and yields. *Field Crops Res.* 40(2): 111-118.

Molion, L.C.B. & Moore, C.J. 1983. Estimating the zero-plane displacement for tall vegetation using a mass conservation method. *Boundary Layer Meteorol.* 26(2): 115-125.

Mulhearn, P.J. & Bradley, E.F.. 1977. Secondary flows in the lee of porous shelterbelts. *Boundary Layer Meteorol.* 12(1): 75-92.

Namikas, S.L. & Sherman, D.J. 1995. A review of the effects of surface moisture content on Aeolian sand transport. In *Desert Aeolian Processes*, 269-293. V.P. Tchakerian, ed. London: Chapman and Hall.

Nelmes, S., Belcher, R.E., & Wood, C.J. 2001. A method for routine characterization of shelterbelts. *Agri. Forest Meteorol.* 106: 303-315.

Nokkentved, C. 1938. Laevukningsundersogelser og typehestemmelser af laehegn. (Investigations of shelterbelts and estimation of types of shelterbelts.) (Danish) *Hedeselskabets Tidsskr. (Health Soc. Jour.)* 59(4): 75-142.

Nordstrom, K.F., & Hotta, S. 2004. Wind erosion from cropland in the USA: a review of problems, solutions and prospects. *Geoderma* 121: 157-167.

Norton, R.L. 1988. Windbreaks: Benefits to orchard and vineyard crops. *Agri. Ecosys. Environ.* 22-23: 205-213.

Nuberg, I.K. 1998. Effects of shelter on temperate crops: A review to define research for Australian conditions. *Agrofores. Sys.* 41: 3-34.

Oke, T.R. 1987. *Boundary layer climates*. Methuen & Co. Ltd., London, UK. pp. 475.

OpenCFD Ltd. 2011. OpenFOAM User Manual. Available at http://cfd.direct/openfoam/user-guide/ Accessed May 2015.

Packwood, A.R. 2000. Flow through porous fences in thick boundary layers: comparisons between laboratory and numerical experiments. *J. Wind Eng. Indus. Aerodyn.* 88: 75-90.

Palacin, J., Palleja, T., Tresanchez, M., Sanz, R., Llorens, J., Ribes-Dasi, M., Masip, J., Arno, J., Escola, A., & Rosell, J.R. 2007. Real-time tree-foliage surface estimation using a ground laser scanner. *IEEE Trans. Instrum. Meas.* 56(4): 1377-1383.

Palojarvi, P., Maatta, K., & Kostamovaara, J. 2002. Pulsed time-of-flight laser radar module with millimeter-level accuracy using full custom receiver and TDC ASICs. *IEEE Trans. Instrum. Meas.* 51(5): 1102-1108.

Parsons, D.R., Wiggs, G.F.S., Walker, I.J., Ferguson, R.I., & Garvey, B.G. 2004. Numerical modelling of airflow over an idealised transverse dune. *Environ. Model. Softw.* 19: 153-162.

Patankar, S. V. 1980. *Numerical heat transfer and fluid flow*. Washington, D.C.: Hemisphere.

Payton, I.J., Newell, C., & Beets, P. 2004. New Zealand carbon monitoring sytem: Indigenous forest shrubland data collection manual. Ministry for the Environment. Wellington, New Zealand.

Plate, E.J. 1971. The aerodynamics of shelterbelts. *Agri. Meteorol.* 8: 203-222.

Pope, C.A., Burnett, R.T., Thun, M.J., Calle, E.E., Krewski, D., Ito, K., & Thurston, G.D. 2002. Lung cancer, cardiopulmonary mortality, and long-tern exposure to fine particulate air pollution. *J. Am. Med. Assoc.* 287(9): 1132-1141.

Popinet, S., 2003. Gerris: a tree-based adaptive solver for the incompressible Euler equations in complex geometries. *J. Comp. Phys.* 190, 572–600.

Predicala, B.Z., & Maghirang, R.G. 2003. Numerical simulation of particulate matter emissions from mechanically ventilated swine barns. *Trans. ASABE* 46:1685-1694.

Qiu, Y., Guan, D., Song, W., & Huang, K. 2009. Capture of heavy metals and sulfur by foliar dust in urban Huizhou Guangdong Province China. *Chemosphere* 75: 447-452.

Raine, J.K. & Stevenson, D.C. 1977. Wind protection by model fences in a simulated atmospheric boundary layer. *J. Indust. Aerodyn.* 2: 159-180.

Raupach, M.R. 1992. Drag and drag partition on rough surfaces. *Boundary Layer Meteorol.* 60(4): 375-395.

Raupach, M.R., Woods, N., Dorr, G., Leys, J.F., & Cleugh, H.A. 2001. The entrapment of particles by windbreaks. *Atmos. Environ.* 35(20): 3373-3383.

Raupach, M.R., Leys, J.F., Woods, N., Dorr, G., & Cleugh, H.A. 2000. Modelling the effects of ripariian vegetation on spray drift and dust: The role of local protection. *Technical Report 29/00.* August 2000, CSIRO Land and Water. CSIRO, Canberra.

Raupach, M.R., & Findlater, P.A. 1993. Effect of saltation bombardment on the entrainment of dust by wind. *J. Geophys. Res.* 98(D7): 12,719-12,726.

Riddle, A., Carruthers, D., Sharpe, A., McHugh, C., & Stocker, J. 2004. Comparisons between FLUENT and ADMS for atmospheric dispersion modeling. *Atmos. Environ.* 38: 1029-1038.

Rosenfeld M., Marom, G., & Bitan, A. 2010. Numerical simulation of the airflow across trees in a windbreak. *Boundary Layer Meteorol.* 135(1): 89-107.

Salim, S.M., Buccolieri, R., Chan, A., Di Sabatino, S., & Cheah, S.C. 2011. Numerical simulation of atmospheric pollutant dispersion in an urban street canyon: Comparison between RANS and LES. *J. Wind Eng. Ind. Aerodyn.* 99: 103-113.

Salyani, M. & Wei, J., 2005. Effect of travel speed on characterizing citrus canopy structure with a laser scanner. *In: J.V. Stafford (Ed.) Precision agriculture '05*. Papers presented at the 5th European conference on precision agriculture, 2005 Uppsala, Sweden. Wageningen Academic Publishers, p. 185-192. Available at http://128.227.177.113/pa/Publications/Salyani_Wei_2005.pdf. Accessed 10 August 2011.

Sanford, P., Wang, X., Greathead, K. D., Gladman, J. H., & Speijers, J. 2003. Impact of Tasmanian blue gum belts and kikuyu-based pasture on sheep production and groundwater recharge in south-western Western Australia. *Australian J. Exp. Agri.* 43(8): 755-767.

Santiago, J.L., Martin, F., Cuerva, A., Bezdenejnykh, N., & Sanz-Andres, A. 2007. Experimental and numerical study of wind flow behind windbreaks. *Atmos. Environ.* 41: 6406-6420.

Saxton, K., Chandler, D., & Schillinger, W. 1999. Wind erosion and air quality research in the northwest U.S. Columbia plateau: Organization and progress. In *Sustaining the Global Farm: Selected Papers from the 10th Intl. Soil Conservation Organization Meeting (ISCO '99)*, 766-770. E.E. Stott, R.H. Mohtar & G.C. Steinhardt eds. West Lafayette, Ind.: USDA-ARS National Soil Erosion Laboratory.

Scanlon, T.J., Stickland, M.T., & Oldroyd, A.B. 2000. An investigation into the attenuation of wind speed by the use of windbreaks in the vicinity of overhead wires. *J. Rail and Rapid Transit* 214(3): 173-182.

Schwartz, R.C., Fryrear, D.W., Harris, B.L., Bilbro, J.D., & Juo, A.S.R. 1995. Mean flow and shear stress distributions as influenced by vegetative windbreak structure. *Agri. and Forest Meteorol.* 75: 1-22.

Sellier, D., Brunet, Y., & Faurcaud, T. 2008. A numerical model of tree aerodynamic response to a turbulent flow. *Forestry* 81(3): 279-297.

Shao, Y. 2008. *Physics and modelling of wind erosion*. 2nd Revised and Expanded Ed. Springer Science.

Shaw, D. 1988. The design and use of living snow fences in North America. *Agri. Ecosys. Environ.* 22-23: 351-362.

Shields Jr, F.D. & Wood, A.D. 2007. The use of large woody material for habitat and bank protection. Technical Supplement 14J. In: *Stream Restoration Design*, National Engineering Handbook Part 654, USDA-NRCS, Washington, D. C.

Siddoway, F.H., Chepil, W.S., & Armbrust, D.V. 1965. Effect of kind, amount, and placement of residue on wind erosion control. *Trans. ASAE.* 8(3): 327-331.

SICK Sensor Intelligence. 2008. LMS200/211/221/291 Laser measurement systems – Technical description. Available at https://www.mysick.com/saqqara/pdf.aspx?id=im0012759. Accessed 10 August 2011.

Skidmore, E.L., Kumar, M., & Larson, W.E. 1979. Crop residue management for wind erosion control in the Great Plains. *J. Soil and Water Conservation.* 34(2): 90-94.

Skidmore, E.L. 1976. Barrier-induced microclimate and its influence on growth and yield of winter wheat. Paper presented at the Shelterbelts on the Great Plains, Denver, Colorado. Wageningen Academic Publishers, p. 57-63. Available at http://128.227.177.113/pa/Publications/Salyani_Wei_2005.pdf. Accessed 10 August 2011.

Skidmore, E.L., Jacobs, H.S., & Hagen, L.J. 1972. Microclimate modification by slat-fence windbreaks. *Agron. J.* 64: 160-162.

Skidmore E.L. & Woodruff, N.P. 1968. Wind erosion forces in the United States and their use in predicting soil loss. In *Agriculture Handbook 346.* United States Department of Agriculture – Agricultural Research Service (USDA-ARS), Washington, D.C.

Shinoda, M., Gillies, J.A., Mikami, M., & Shao, Y. 2011. Temperate grasslands as a dust source: Knowledge, uncertainties, and challenges. *Aeolian Res.* 3(3): 271-293.

Silva, L.F.L.R. & Lage, P.L.C. 2011. Development and implementation of a polydispersed multiphase flow model in OpenFOAM. *Comp. & Chem. Eng.* 35(12): 2653-2666.

Smith, E.G. & English, B.C. 1982. Determining wind erosion in the Great Plains. CARD paper series 82-3, Center for Agricultural and Rural Development, Iowa State University, Ames.

Sow, M., Goossens, D., & Rajot, J.L. 2006. Calibration of the MDCO dust collector and of four versions of the inverted frisbee dust deposition sampler. *Geomorph.* 82: 360-375.

Stam, J. 2003. Real-time fluid dynamics for games. Proceedings of the Game Developer Conference. Available from: http:// www.autodeskresearch.com/pdf/GDC03.pdf. Accessed 5 January 2015.

Stoeckeler, J.H. 1962. Shelterbelt influence on Great Plains field environment and crops. *USDA Prod. Res. Rep. No.* 62, pp. 22.

Straight, R. & Brandle, J. 2007. *Windbreak density: Rules of thumb for design*. AF Note-36, UNL- East Campus, Lincoln, NE: USDA-NAC. Available at http://www.unl.edu/nac/agroforestrynotes/an36w03.pdf. Accessed 10 August 2011.

Stredova, H., Podhrazska, J., Litschmann, T., Streda, T., & Roznovsky, J. 2012. Aerodynamic parameters of windbreak based on its optical porosity. *Contributions to Geophys. and Geodesy* 42(3): 213-226.

Sudmeyer, R.A. & Scott, P.R. 2002. Characterization of a windbreak system on the south coast of Western Australia. 1. Microclimate and wind erosion. *Aus. J. Exp. Agri.* 42: 703-715

Swistock, B.R., DeWalle, D.R., & Farrand, E.P. 2005. Windbreaks and shade trees. Penn State Cooperative Extension, College of Agricultural Sciences, University Park, PA. Available at http://pubs.cas.psu.edu/freepubs/pdfs/uh172.pdf. Accessed 10 August 2011.

Takano, Y. & Moonen, P. 2013. On the influence of roof shape on flow and dispersion in an urban street canyon. *J. Wind Eng. Ind. Aerodyn.* 123: 107-120.

Tamang, B., Andreu, M.G., Friedman, M.H., & Rockwood, D.L. 2009. Windbreak designs and planting for Florida agricultural fields. FOR227. School of Forest Resources and Conservation Department, Florida Cooperative Extension Service, Institute of Food and Agricultural Sciences, University of Florida, FA.
Available at http://edis.ifas.ufl.edu/fr289. Accessed 10 August 2010.

Taylor, P.A. 1988.Turbulent wakes in the boundary layer, pp. 270-292. In W.L. Steffen and O.T. Denmead (eds.), *Flow and transport in the natural environment: Advances and applications*, Springer – Verlag, Berlin.

Thorne, M.E., Young, F.L., Pan, W.L., Bafus, R., & Alldredge, J.R. 2003. No-till spring cereal cropping systems reduce wind erosion susceptibility in the wheat/fallow region of the Pacific Northwest. *J. Soil and Water Conserv.* 58(5): 250-257.

Ticknor, K.A. 1988. Design and use of field windbreaks in wind erosion control systems. *Agri. Ecosys. Environ.* 22: 123-132.

Tiwary, A., Morvan, H.P., & Colls, J.J. 2005. Modelling the size-dependent collection efficiency of hedgerows for ambient aerosols. *Aerosol Sci.* 37: 990-1015.

Tominaga, Y. & Stathopoulos, T. 2007. Turbulent Schmidt numbers for CFD analysis with various types of flowfield. *Atmos. Environ.* 41: 8091-8099.

Toure, A.A., Rajot, J.L., Garba, Z., Marticorena, B., Petit, C., & Sebag, D. 2011. Impact of very low crop residues cover on wind erosion in the Sahel. *Catena.* 85: 205-214.

TSI Incorporated. 2010. DustTrak II™ Aerosol Monitor operating and service manual. P/N 6001893, Revision E, Shoreview, MN.

Tuzet, A. & Wilson, J. 2007. Measured winds about a thick hedge. *Agri. Forest Meteorol.* 145: 195-205.

Tyndall, J. & Colletti, J. 2007. Mitigating swine odor with strategically designed shelterbelt systems: A review. *Agrofores. Sys.* 69: 45-65.

Ucar, T. & Hall, F.R. 2001. Windbreaks as a pesticide drift mitigation strategy: a review. *Pest Manag. Sci.* 57(8): 663-675.

USDA NRCS, 2007. Soil erosion on cropland 2007. Technical Resources. http://www.nrcs.usda.gov/wps/portal/nrcs/detail/mo/technical/dma/nri/?cid=stelprdb1041887 (Accessed 19 November 2012)

Van Eimern, J., Karschon, R., Razumova, L.A., & Robertson, G.W. 1964. Windbreaks and shelterbelts. World Meteorological Organization Technical Note No. 59, pp. 188.

Versteeg, H.K. & Malalasekera, W. 1995. *An introduction to computational fluid dynamics*. The Finite Volume Method. Prentice-Hall, Englewood Cliffs, NJ. pp. 257.

Vigiak, O., Sterk, G., Warren, A., & Hagen, L.J. 2003. Spatial modeling of wind speed around windbreaks. *Catena* 52: 273-288.

Vomicil, J.A. & Ramig, R.E. 1976. Wind erosion control on irrigated Columbia basin land, A handbook of practices. Spec. Rep. 466 (Corvallis Oregon State University Extension Service).

Wang, X., Chen, F. & Dong, Z. 2006. The relative role of climatic and human factors in desertification in semiarid China. *Global Environ. Change* 16: 48-57.

Webb, N.P. & McGowan, H.A. 2009. Approaches to modelling land erodibility by wind. *Progress in Physical Geog.* 33(5): 587-613.

Webb, N.P., & Strong, C.L. 2011. Soil erodibility dynamics and its representation for wind erosion and dust emission models. *Aeolian Res.* 3: 165-179.

Wei, J. & Salyani, M. 2004. Development of a laser scanner for measuring tree canopy characteristics: Phase 1. Prototype development. *Trans. ASAE* 47(6): 2101-2107.

Wei, J. & Salyani, M. 2005. Development of a laser scanner for measuring tree canopy characteristics: Phase 2. Foliage density measurement. *Trans. ASAE* 48(4): 1595-1601.

Wenneker, M., Heijne, B., & van de Zande, J.C. 2005. Effect of natural windbreaks on drift reduction in orchard spraying. *Commun. Agric. Appl. Biol. Sci.* 70(4): 961-969.

Wilkinson, K.M. & Elevitch, C.R. 2000. Multipurpose windbreaks: Design and species for Pacific Islands. *Agroforestry Guides for Pacific Islands No. 8.* Permanent Agriculture

Resources, Holualoa, Hawaii, USA. Available at http://university.uog.edu/cals/people/Pubs/Agrofors/multwind.pdf. Accessed 10 August 2011.

Wilson, J.D. 1997. A field study of the mean pressure about a windbreak. *Boundary Layer Meteorol.* 85: 327-358.

Wilson, J.D. 2005. Deposition of particles to a thin windbreak: The effect of a gap. *Atmos. Environ.* 39: 5525-5531.

Wolfe, S.A., & Nickling, W.G. 1993. The protective role of sparse vegetation in wind erosion. *Progress Phys. Geog.* 17(1): 50-68.

Woodruff, N.P., Lyles, L., Dickerson, J.D., & Armbrust, D.V. 1974. Using cattle feedlot manure to control wind erosion. *J. Soil Water Conserv.* 29(3): 127-129.

Woodruff, N.P. & Siddoway, F.S. 1965. A wind erosion equation. *Soil Sci. Soc. Amer. Proc.* 29(5): 602-608.

Woodruff , N.P. & Armbrust, D.V. 1968. A monthly climatic factor for the wind erosion equation. *J. Soil and Water Cons.* 23(3): 103-104.

Woodruff, N.P., Read, R.A., & Chepil, W.S. 1959. Influence of a field windbreak on summer wind movement and air temperature. *Kans. Agri. Expt. Sta. Tech. Bul.* 100.

Yeh, C.P., Tsai, C.H., & Yang, R.J. 2010. An investigation into the sheltering performance of porous windbreaks under various wind directions. *J. Wind Eng. Ind. Aerodyn.* 98: 520-532.

Yousef, F., Visser, S.M., Karssenberg, D., Erpul, G., Cornelis, W.M., Gabriels, D., & Poortinga, A. 2012. The effect of vegetation patterns on wind-blown mass transport at the regional scale: A wind tunnel experiment. *Geomorphology.* 159-160: 178-188.

Yusaiyin, M. & Tanaka, N. 2009. Effects of windbreak width in wind direction on wind velocity reduction. *J. Fores. Res.* 20(3): 199-204.

Zhang, C.L., Zou, X.Y., Gong, J.R., Liu, L.Y., & Liu, Y.Z. 2004. Aerodynamic roughness of cultivated soil and its influences on soil erosion by wind in a wind tunnel. *Soil Till. Res.* 75: 53-59.

Zhu, J-J. 2008. Wind shelterbelts. In: Encyclopedia of Ecology. pp. 3803-3812.

Zobeck, T.M. 1991. Soil properties affecting wind erosion. *J. Soil Water Conserv.* 46(2): 112-118.

Zuo, W. 2005. Introduction to computational fluid dynamics. Available at http://www14.in.tum.de/konferenzen/Jass05/courses/2/Zuo/Zuo_paper.pdf Accessed January 2014.

CHAPTER 3 - Sand Transport and Abrasion within Simulated Standing Vegetation

3.1. Introduction

Wind erosion is a prominent problem in arid and semi-arid areas of the U.S., especially during the spring and summer. Weathering processes of soil as a result of extreme temperature changes and soil degradation have caused wind erosion in temperate grasslands (Shinoda et al., 2011). Wind erosion effects are more pronounced when vegetative cover is sparse, which has led to the practice of using crop residues to protect the topsoil from abrasion and depletion. The damage that can be experienced by young crops like wheat can greatly impact their early stages of growth. At that stage they are susceptible to damage by abrasion due to its not yet fully developed plant structure and greater exposure to saltation caused by gusts of wind. (Hagen and Casada, 2013)

Previous research has studied the effects of different types of vegetation (Farmer, 1993) and soil (Belnap and Gillette, 1998; Merrill et al., 1999) on wind erosion. Wind erosion's adverse effects include crop damage/loss (Genis et al., 2012; Baker et al., 2009), soil fertility reduction (Lyles, 1975), soil degradation (Lal, 2001), soil nutrient loss (Gomes et al., 2003), and redistribution of topsoil (Larney et al., 1998).

Wind erosion controls also have been studied (Woodruff et al., 1974; Skidmore et al., 1979; Michels et al., 1995a and 1995b; Bielders et al., 2000; Bao et al., 2009). Several wind tunnel studies have investigated control measures for different plant and stubble configurations. Bisal (1968) used freshly harvested wheat stubble (including the crown and a small portion of the root) with a constant height of 15 cm protruding above the sand surface. Densities of wheat stubble corresponding to different threshold velocities were determined, and results showed that

threshold velocities were 5.36 m s^{-1} for a density of 1,200 kg ha^{-1} and 8.49 m s^{-1} for a density of 7,200 kg ha^{-1}. Sand discharges (the mass of sand passing through a specific horizontal width per unit time) were also measured in the absence of wheat stubble and found to be 399 g min^{-1} at 5.36 m s^{-1} and 1,680 g min^{-1} at 8.49 m s^{-1}

Lyles and Allison (1976) studied the protection efficiencies of simulated standing stubbles (sorghum, corn, and wheat) with different heights, sizes, spacings, and orientations. They reported that wheat required less stubble mass than corn and sorghum to provide the same wind erosion protection because of its greater specific area to interact with the wind.

Using live plants in a wind tunnel, Burri et al. (2011) studied three canopy density levels for perennial ryegrass (*Lolium perenne*) with a configuration of 28 cm (spacing parallel to wind) by 14 cm (spacing perpendicular to the wind) along the wind tunnel. Quartz sand, ranging in size from 0.4 to 0.8 mm, was used for the entire tunnel floor. The authors observed that PM_{10} (particulate matter of aerodynamic diameter < 10 μm) concentrations and sediment mass fluxes have an inverse relationship with canopy density. The PM_{10} observed during the experiment was the result of further breakdown of the sand used in the experiment, and in medium- and high-density canopies, vertical distribution of sediment mass fluxes were influenced particularly by canopy movement in the wind and sand particle impact within the canopies.

The impact of crop residues on wind erosion was studied by Toure et al. (2011). The study showed that in the Sahel, where millet stalk quantity varies after the harvest season from less than 2% to 12% within a span of four months, even very low residue levels (2%) were sufficient to reduce wind erosion potential by a factor of four compared with bare conditions.

Youssef et al. (2012) conducted a wind tunnel study on the effects of different configurations of artificial vegetation on wind erosion. They used beach sand along the tunnel

floor and artificial plants (polyethylene ribbons attached to iron sticks) representative of the morphology of *Atriplex halimus* (a common plant used for revegetation on degraded lands (Hassine and Lutts, 2010)) at a downscaled ratio of 1:50 to simulate field conditions satisfactory for the boundary layer conditions existing within the tunnel. The authors found that vegetation pattern is a factor in creating turbulence, which causes higher mass fluxes of windblown particles; that is, if there are patches of vegetation throughout the entire floor area, the high values of the mass fluxes were concentrated close to the vegetation patches, especially when wind speeds were very high. This study also reported the effects of changing canopy configuration, namely: (a) "street"-type erosion (Bowker et al., 2008) brought about by a regular grid pattern, (b) deposition caused by redistribution of sand within the canopy perimeter and spatial sequencing of erosion, and (c) satisfactory sheltering zones compared with literature values of 10 to 20 times the height of windbreaks (Cornelis and Gabriels, 2005).

Although there are a number of studies on standing stubble, young plants, and artificial vegetation, studies quantifying abrasion energy in different configurations of residue or vegetation have been limited. In addition, previous wind tunnel studies were either limited by the space used within the tunnel (Lyles and Allison,1976; Genis et al., 2012) or the canopy models used within the tunnel were scaled down (Youssef et al., 2012). Hagen and Casada (2013) studied artificial dicotyledonous plants, which showed a direct increasing relationship between canopy leaf area index (LAI) and threshold velocity, whereas the opposite was found between LAI and sand transport capacity. A direct relationship was also observed between increasing wind speeds above the threshold and increasing total abrasion energy. Because the leaves of the artificial plants were not uniform, vertical abrasion profiles were affected by the position of leaves within the canopy, with leaves close to the sand surface deflecting a significant portion of

the wind stream upward and resulting in an upward deflection of impact energy. This deflection influenced the area just above the sand surface, which sustains maximum abrasion impact.

This study examined the effects of standing vegetation configurations (similar to wheat seedlings) on the mechanics of wind erosion and on the amount of abrasion occurring within a simulated plant canopy. This study was parallel to the work of Hagen and Casada (2013) that was focused on abrasion effects on broad-leaved (dicotyledonous) plant models, but in this case abrasion effects for simulated young wheat-like (monocotyledonous) plant models were determined. Specific objectives were to:

1) determine the wind profile and threshold velocities among different plant configurations for simulated standing vegetation; and
2) compare the relative abrasion energies at the sand surface and within simulated standing vegetation.

3.2. Materials and Methods

3.2.1. Wind Tunnel Description

This research was conducted from April 2012 to July 2012 at a wind tunnel facility (Figure 3.1) of the Center for Grain and Animal Health Research (CGAHR), USDA – ARS, Manhattan, Kansas. The tunnel is a variable-speed, push-type tunnel with dimensions of 15.3 m length, 1.52 m width, and 1.82 m height. Quartz sand of 0.29 to 0.42 mm diameter was placed (40 mm deep) along the entire floor of the tunnel. The wind tunnel was instrumented to measure atmospheric pressure (Model CS100, Campbell Scientific, Alberta, CA), air temperature, and relative humidity (Model CS500L, Campbell Scientific, Alberta, CA). The sensors were placed at the downwind portion of the tunnel where the samplers and system of pitot tubes were present. The tunnel was also equipped with sensors and samplers for measuring wind speed profile,

relative abrasion energy, and sand discharge. These were measured for the bare sand surface and sand surface covered with artificial vegetation densities and configurations.

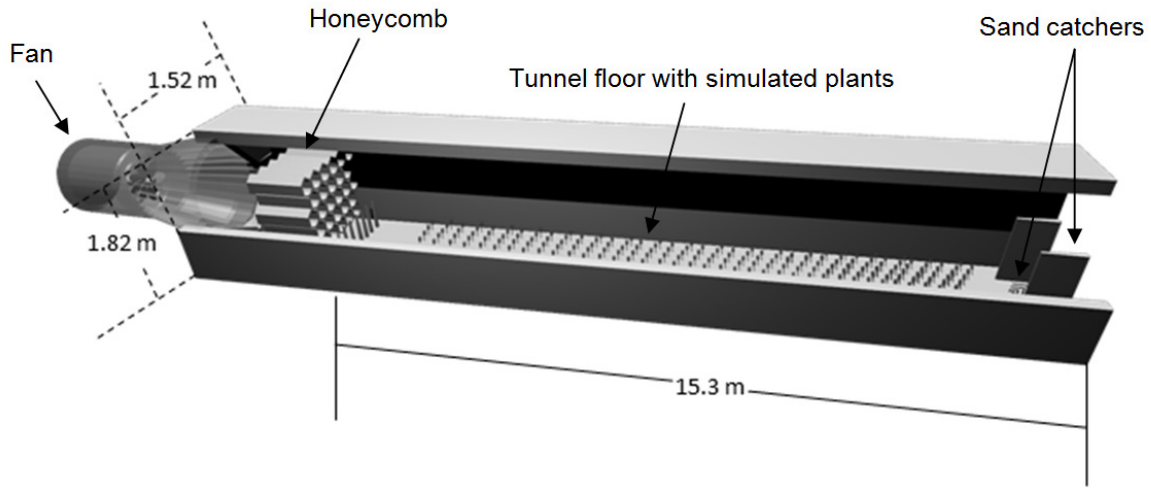

Figure 3.1. Wind tunnel schematic diagram.

3.2.2. Artificial Standing Vegetation

Plastic straws (split into 6 segments that corresponds to 80 mm height from the top while the remaining height corresponds to the stalk, which represents the leaf area of young wheat plants) were attached to a dowel rod (6 mm diameter) to represent artificial standing vegetation (Figure 3.2). Dowel rods were then inserted through the sand and into the tunnel floor at varying distances. The model canopy used for this experiment was based on characteristics of young wheat plants (Masle and Passioura, 1987) and compared and modified version to that of model wheat done by Shaw et al. (1995).

Figure 3.2. Dowel rods with plastic straws split 80 mm from the top to simulate young plants.

To determine the effects of vegetation density and height, three spatial configurations and two plant heights (150 mm and 220 mm) for the standing vegetation were compared (Figure 3.3). The test configurations and artificial vegetation characteristics are summarized in Table 3.1. The leaf area index (LAI) and silhouette area index (SAI) were calculated using the following equations:

$$\mathrm{LAI} = \frac{\mathrm{LA}}{\mathrm{FA}} \tag{3.1}$$

$$\mathrm{SAI} = \frac{\mathrm{FSA}}{\mathrm{FA}} \tag{3.2}$$

where LA is leaf area per plant, FSA is frontal stem and leaf areas per plant, and FA is floor area per plant.

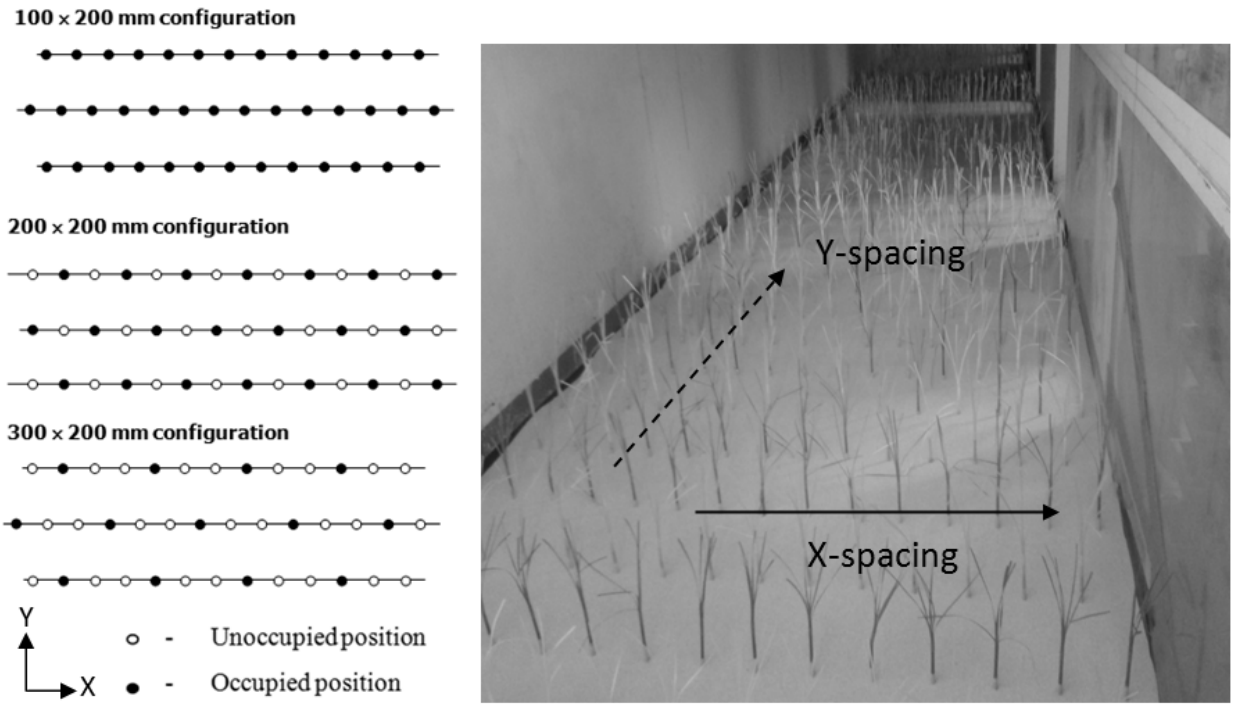

Figure 3.3. Three vegetation patterns used in the wind tunnel for abrasion and wind profile tests.

Table 3.1. Dimensions and spacing of artificial standing vegetation for wind tunnel tests.

X-spacing (perpendicular to wind) (mm)	Y-spacing (parallel to wind) (mm)	Maximum plant height (mm)	Frontal stem and leaves area per plant (mm^2)	Leaf area index (mm^2 mm^{-2})	Silhouette area index (mm^2 mm^{-2})
100	200	220	801	0.123	0.0775
100	200	150	141	0.123	0.0137
200	200	220	801	0.062	0.0388
200	200	150	141	0.062	0.0068
300	200	220	801	0.041	0.0258
300	200	150	141	0.041	0.0046

3.2.3. Wind Speed Profile

Wind speed profiles downwind in the tunnel were measured using a static-pitot tube system setup composed of 11 pitot tubes positioned in a line up from the tunnel floor (Figure 3.4). A separate static-pitot tube was used to measure the free stream velocity at a height of 95

cm above the sand surface and horizontally centered in the tunnel. These measurements ensured consistency of wind velocities within the different pressure transducers. The wind profiles were recorded at 3-min intervals using two wind velocities below the threshold for each tunnel configuration (bare sand, 100 × 200, 200 × 200, and 300 × 200 mm artificial vegetation configurations). The static-pitot tube pressures were obtained by pressure transducers (Model PX653-01D5V, Omega Engineering, Inc.) that operated with water pressure of 0 to 25.4 mm. The instantaneous static pressures measured were used to compute the instantaneous wind speeds within the tunnel using the Bernoulli equation.

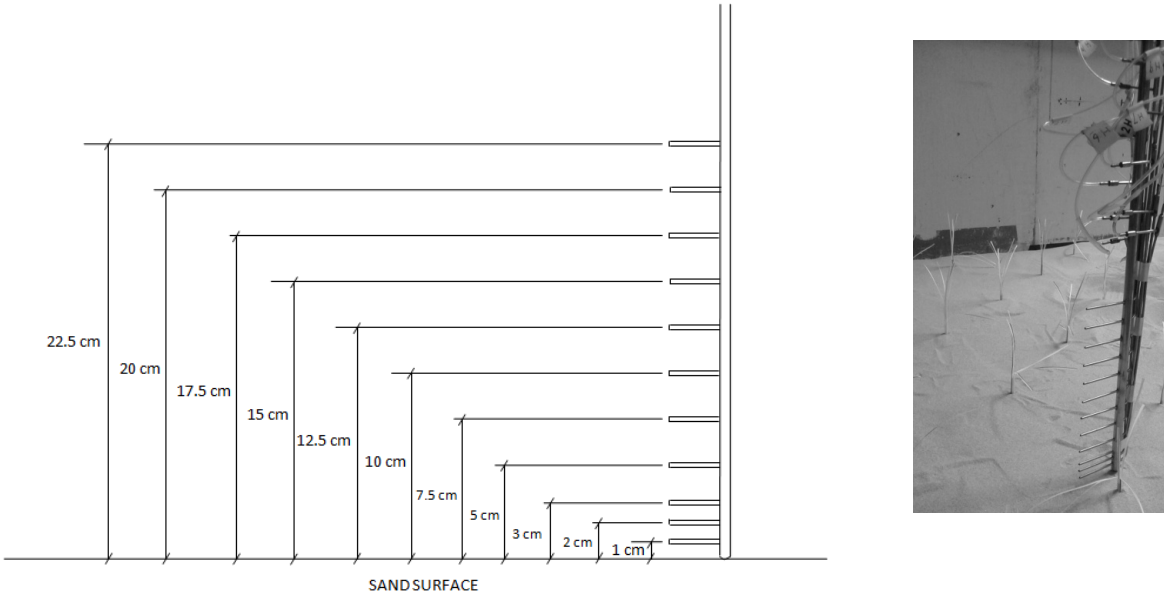

Figure 3.4. Static-pitot tube system arrangement for measuring wind profile.

The static pressures measured by the pressure transducers were calibrated using surgical syringes and a Dwyer inclined manometer air-filter gage (Model Series 250-AF) to ensure stable pressure and voltage during measurements (ADInstruments, 2009). The values were then converted to digital output via Labview software (Labview Student Ver. 2012, National Instruments). Pressure transducers were calibrated for every stubble configuration within the

wind tunnel. Prior to taking vertical wind profile measurements, the pitot tube system was tested horizontally to ensure the measurements agreed and no flow disturbances were experienced.

3.2.4. Sand Discharge

The sand discharge collection system (Figure 3.5) consisted of two vertical slot samplers and vertical sand profile samplers. The slot samplers are 96 to 100% saltation catch efficiency (Hagen and Casada, 2013) wedge-shaped samplers with a 5-mm front opening, 698-mm height, and 44-mm maximum width (downwind) and side vents covered with fine screens. The system was designed to collect the amount of sand discharge at the end of the tunnel during 3-min intervals in tubs beneath the sampler, below the tunnel floor. Vertical sand profile tube samplers Figure 5,a) had diameters of 16.1 mm, 13.2 mm, 13.2 mm, 13.2 mm, and 13.2 mm from the bottom tube to the top. These samplers collected sand at specific heights (8.05 mm, 29.0 mm, 58.4 mm, 108.4 mm, 163.4 mm, as measured from the center of the tubes to the tunnel floor surface). The vertical sand profile tube samplers were placed between the two vertical slots.

Five wind speeds with three replicates each were used for determining saltation discharge (three wind speeds at 0.25 m s^{-1} increments from the threshold wind speed for a specific tunnel configuration were referred to as lower wind speeds while two wind speeds at increments of 2.5 m s^{-1} from the threshold were referred to as higher wind speeds). Threshold for saltation was determined by observing the wind speed at which the sand grains started to move. The two high wind speeds were chosen to ensure enough sand transport occurred within each standing vegetation configuration. One of the lower wind speeds (referred to as low free stream wind speed - about 0.5 m s^{-1} above the saltation threshold wind speed) was used for comparison while the highest wind speed corresponding to each configuration was chosen for comparison and was referred to as high free stream wind speed. The amount of sand collected without a canopy (bare

sand) was used as a control to compare the sheltering performance at two different heights for a specific wind speed (arbitrarily chosen at 11 m s^{-1}, which is also above the threshold for all configurations).

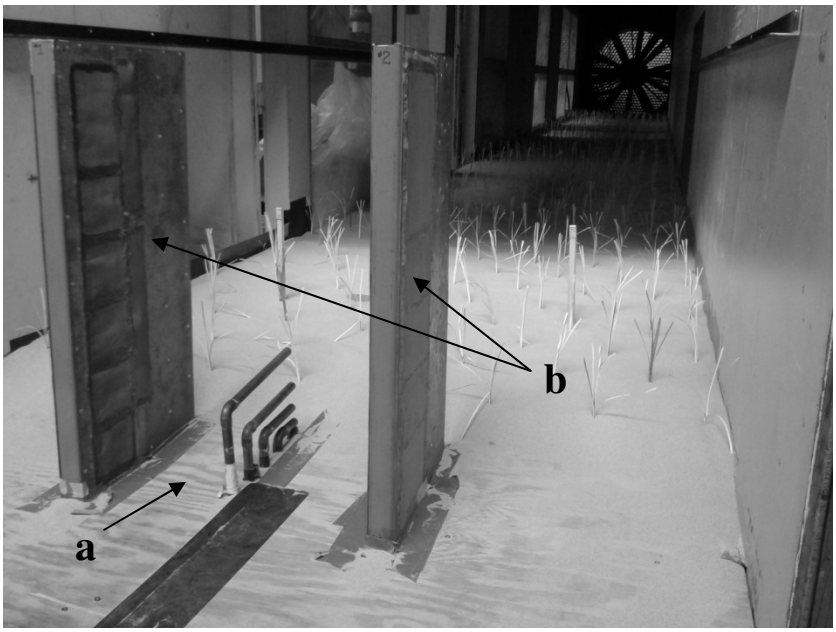

Figure 3.5. Sand discharge collection system: (a) vertical sand profile tubes and (b) two vertical slot samplers.

The sand discharge flux (g m^{-1} s^{-1}) through the two vertical sampler slots (q_{slot}) was calculated using the following equation:

$$q_{slot} = \frac{(m_{tub})}{(w_{slot})(t)} \tag{3.3}$$

where m_{tub} is the mass of sand collected in rectangular tub located underneath the vertical, rectangular slot samplers at the end of the tunnel; w_{slot} is the width of the vertical slot sampler (0.005 m); and t is the duration of sampling (180 s).

Similarly, the sand discharge flux (g m^{-1} s^{-1}) through the five central catch tubes (q_{ctube}) was calculated using the following equation:

$$q_{tube} = \frac{(m_{ctube})}{(d_{ctube})(t)} \quad (3.4)$$

where m_{ctube} is the mass of sand collected by the central catch tube that were connected to small containers underneath and d_{ctube} is the diameter of the central catch tube.

3.2.5. Abrasion Energy Assessment

Abrasion energy was assessed using two horizontal abrasion plate sensors mounted at the sand surface and two vertical abrasion stick sensors mounted in front of the simulated standing vegetation (Figure 3.6), near the downwind edge of the simulation vegetation, as described by Hagen and Casada (2013). The vertical abrasion sticks were placed just in front of the artificial vegetation to observe impact of sand upwind. Note that all plant configurations follow a pattern of alternating columns (Figure 3.6) parallel to the wind to minimize the street effect identified by Bowker et al. (2008).

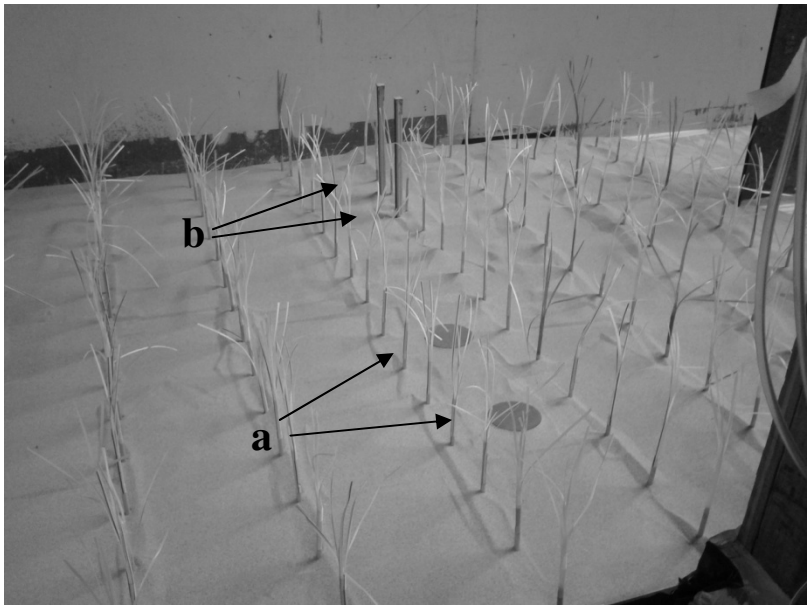

Figure 3.6. Measurement of abrasion energy: (a) horizontal abrasion plates and (b) vertical abrasion sensors.

The soil used for the abrasion sensors was composed of 90% Haynie very fine sandy loam and 10% Kahola silt loam collected near the research location. The soil was mixed with water to saturation and placed in channels (1.2 cm x 25 cm) and plates (8 cm diameter deep) and air-dried to form consolidated sticks and plates. The plates and sticks were tested and calibrated for soil consistency prior to tests by dropping sand grains at terminal velocity on the tilted surfaces of the abrasion sensors (Hagen and Casada, 2013). Repeatability and consistency between measured abrasion losses were observed during calibration.

The amount of abrasion was measured from the weight difference before and after each run for each of the horizontal abrasion plates and vertical abrasion sticks. This value represents the effective kinetic energy associated with the surface sand impact on the abrasion sensors. Abrasion losses observed from the vertical and horizontal abrasion sensors were computed using the following steps (Hagen and Casada, 2013):

(i) Computation of soil mass loss from abrasion (kg m^{-2})

$$\text{Soil mass loss from abrasion} = \frac{m_a}{A_a} \tag{3.5}$$

where m_a is the mass of soil loss from the abrasion sensor and A_a is the area of soil inside the abrasion sensor exposed to abrasion. Because two different abrasion sensors were used (vertical abrasion sticks and horizontal abrasion plates with areas of sand exposed), results were computed as follows:

$$A_{av} = (\ell_{av})(w_{av}) \tag{3.6}$$

$$A_{ah} = \frac{(\pi)(d_h)^2}{4} \tag{3.7}$$

where A_{av} is the area exposed for abrasion in vertical sticks sensor; ℓ_{av} length of soil (0.265 m) and w_{av} is the width of soil (0.012 m) within the vertical stick sensor; A_{ah} is the area exposed for abrasion in the horizontal plates sensor and d_h diameter of horizontal plate sensor (0.08 m).

(ii) Computation of predicted sand discharge

This step requires a value of sand discharge for the slot sampler in relation to the width of the abrasion sensor; the width used for horizontal plates was d_h while width of vertical abrasion stick (w_v) used was 0.012 m. The sand discharge computed using the mass collected by the rectangular tubs at the end of the tunnel located underneath the vertical slot samplers is called the effective saltation discharge (q_{eff}), which is computed as follows:

$$q_{eff} = \frac{(m_{tub})}{(w_{slot})} \tag{3.8}$$

The predicted sand discharge for the horizontal plate abrasion sensor (q_h)is as follows:

$$q_h = (q_{eff})(d_h) \tag{3.9}$$

The predicted sand discharge for the horizontal plate abrasion sensor (q_h)is as follows:

$$q_v = (q_{eff})(w_v) \tag{3.10}$$

The coefficient of abrasion (C_{an}) was computed from the quotient of soil loss from abrasion sensors (kg m^{-2}) and the effective saltation discharge (kg m^{-1}) derived from the collected sand by two vertical slot samplers at the end of the tunnel, thus C_{an} has units of m^{-1}. This value is actually a measure of the effective kinetic energy experienced by the abrasion sensor soil surface brought about by the emerging impact of sand through saltation (Hagen and Casada, 2013).

3.2.6. Wind Erosion Mechanism

Different aerodynamic parameters govern the determination of the extent of wind erosion. Threshold friction velocity, the minimum wind speed at which the soil/sand particles

start to move, is one of the most critical parameters that dictate the magnitude and frequency of erosion (Hagen, 2001; Marticorena et al., 1997). Several factors affect this parameter, namely, (a) type of soil, (b) the amount of moisture in the soil, (c) surface roughness for the location, and (d) friction velocity.

The log-law form proposed by Greeley and Iversen (1985) to compute wind profile parameters assumes constant temperature gradient and air density:

$$U = \left(\frac{U_{*v}}{K}\right)\ln\left(\frac{Z - D}{Z_o}\right) \tag{3.11}$$

where U is wind velocity, U_{*v} is the friction velocity above the vegetation, K is the von Karman constant (i.e., 0.41), D is the displacement height, Z is the height above the surface, and Z_o is the aerodynamic roughness. Surface threshold friction velocity, U_{ot}, was determined for the bare sand configuration together with equation (11) where D is set to zero. The displacement D was computed using the conservation of mass methodology used by Molion and Moore (1983), which proved to be better than graphical and other least-square error methods (Dong et al., 2001):

$$D = \left(Z_f - \frac{Z_f - Z_{os}}{\ln\left(\frac{Z_f}{Z_{os}}\right)}\right) - \frac{1}{2U}\left(\sum_{i=2}^{N}(U_i + U_{i+1})(Z_i - Z_{i-1}) + U_1 Z_1\right) \tag{3.12}$$

where Z_f is the roughness length of the vegetated surface, Z_{os} is the roughness length of the smooth surface, U is the free-stream wind velocity, U_i is the wind velocity at height Z_i, and N is the number of height levels. The method incorporates computation of D using an aerodynamic roughness estimate together with a trapezoidal rule for integrating wind profiles measured for various dowel canopy configurations and predicts the incompressible bulk flow displacement brought about by the artificial stubble. After D is known, estimation via the least squares method

detailed in Ling (1976) was done to calculate Z_o using multiple wind velocity profiles measured below the sand movement threshold velocity, which was also used for the computation of U_{*v} for various inputs of log-law profiles measured during the experiment.

3.2.7. Data Analysis

Wind profile, sand discharge, and abrasion energy data were screened for outliers using a distance distribution-based method under the extreme value analysis method described by Aggarwal (2013). One outlier from the 4 x 8 220-mm height configuration was not included in computation for abrasion energy. The mean values were compared using the normality and homogeneity of variances assumption, and a standard statistical test (e.g., paired t-test) was applied. T-tests using Microsoft Excel (Microsoft Corp., Redmond, WA.) and Holm's test through the MATLAB (MathWorks software, R2011a Student Version) code generated by Cardillo (2006) were used to compare the measured values between runs at different tunnel configurations. An analysis of variance (ANOVA) was done using Microsoft Excel (Microsoft Corp., Redmond, WA.) for determining the effect of different vegetation density and heights. A 5% level of significance was used for all cases. CurveExpert 1.4 (Hyams, 2013) was used to plot best-fit curves, which were compared with the curve fitting tool in Microsoft Excel (Microsoft Corp., Redmond, Wash.).

3.3. Results and Discussion

3.3.1. Wind Profiling

The sand used for the study had a mean threshold friction velocity (U^*_{ot}) of 0.24 m s^{-1} and was the basis for the computation of surface-to-above canopy friction velocities (U^*_{ot}/U^*_{v}). Unlike the soil loss ratio (Lyles and Allison, 1981), this parameter is not strongly affected by wind speed (Raupach, 1992).

Table 3.2 summarizes threshold wind speeds and their respective standard error of the mean (SEM) per stubble configuration. As expected, the configuration with a greater density of plastic straws along the tunnel floor area showed greater resistance to wind erosion, as evidenced by the highest mean threshold wind speed value (9.71 m s^{-1}).

Table 3.2. Computed dimensionless aerodynamic parameters and SEM of standing vegetation configurations.

Maximum leaf height (H) (mm)	Configuration	Threshold free-stream wind speed (m s^{-1})	Zo/H (mm/mm)	D/H (mm/mm)	U^*_{ot}/U^*_v (m s^{-1}/m s^{-1})
150	100 × 200	8.96 ± 0.02	0.059 ± 0.002 [a]	0.147 ± 0.004 [b]	0.261 ± 0.003 [b]
150	200 × 200	7.24 ± 0.01	0.088 ± 0.015 [a]	0.114 ± 0.006 [a]	0.329 ± 0.019 [a]
150	300 × 200	6.28 ± 0.01	0.068 ± 0.011 [a]	0.079 ± 0.016 [b]	0.399 ± 0.020 [b]
220	100 × 200	9.71 ± 0.01	0.105 ± 0.004 [b]	0.166 ± 0.006 [b]	0.221 ± 0.007 [b]
220	200 × 200	8.16 ± 0.02	0.104 ± 0.020 [b]	0.135 ± 0.015 [c]	0.247 ± 0.019 [c]
220	300 × 200	6.67 ± 0.01	0.119 ± 0.018 [b]	0.121 ± 0.011 [b]	0.279 ± 0.016 [b]

[*] **Different letters in the same column indicate significant difference ($p < 0.05$).**

As expected, roughness height (Z_o) increased with increasing vegetation height (H) for specific configurations, which was shown by the significant difference ($p < 0.05$) between the relative roughness height (Z/H) values of two heights used per configuration. Zero displacement height (D) also increased with increasing H. The ratio of threshold friction (U^*_{ot}) and friction (U^*_v) velocities decreased as the value of H increased. On the other hand, for the same value of H at different configurations, the value of D decreased as the configuration became less dense, but no trend was observed in the values for Z_o at the same height. The ratio of threshold friction (U^*_{ot}) and friction (U^*_v) velocities increased as the configuration became less dense, which was expected because a less dense configuration meant a smaller value of U^*_v.

This differed from the results of Hagen and Casada (2013) for simulated dicotyledonous plants (e.g. soybean plants). They observed an improved protection brought about by shorter canopies

compared to taller ones due to the large leaf area near the ground, which caused better sheltering and capture of saltating particles. The simulated standing vegetation used for this study did not intercept saltating particles like the simulated soybean vegetation, especially for shorter canopies because of their relative difference in leaf structure, that is, a greater leaf area near the ground compared to straws absorbs wind energy and intercepts saltating grains better.

3.3.2. Sand Discharge

The sand discharge was dependent on the presence of canopies similar to what Hagen and Casada (2013) observed. For this study sand discharge was also found to be dependent on canopy configuration. In general, taller standing vegetation (220 mm height) provided greater sheltering than shorter vegetation (150 mm) for all configurations, which was evident in the decrease in sand discharge (g m s^{-1}). These differences in sheltering were expected based on a larger total area of barrier for a given configuration providing a larger sheltering effect. Table 3.3 compares sand discharge for the catch tubes at 11 m s^{-1}. It was found that most of the configurations were significantly different from bare sand except for the 300 × 200 mm configuration at 150 mm canopy height ($p > 0.05$).

Table 3.3. Summary of sand discharge for catch tubes at 11 m s^{-1} wind speed.

Height of central portion of catch tube (mm)	Sand Discharge (g m^{-1} s^{-1})						
	Bare Sand	150 mm canopy height			220 mm canopy height		
		4x8	8x8	12x8	4x8	8x8	12x8
16.1	9.79	2.29 [a]	5.96 [a]	9.69 [a]	0.84 [a]	4.51 [a]	7.33 [a]
29.0	5.96	1.54 [b]	2.39 [b]	4.23 [b]	0.55 [b]	2.04 [b]	3.39 [b]
58.4	3.53	0.54 [c]	1.07 [b]	2.48 [b]	0.38 [b]	0.80 [c]	1.67 [c]
108	1.32	0.26 [c]	0.70 [c]	0.95 [c]	0.23 [c]	0.44 [c]	0.36 [d]
163	0.19	0.08 [d]	0.14 [c]	017 [c]	0.01 [d]	0.02 [d]	0.03 [e]

[*] **Different letters in the same column indicate significant difference ($p < 0.05$).**

Figure 3.7 shows that the lower two catch tubes collected most of the saltating sand (80-94%) while the higher two tubes collected minimal sand (1-5 %). The same behavior was observed up to a wind speed of about 15 m s^{-1}, which was the maximum tested wind speed.

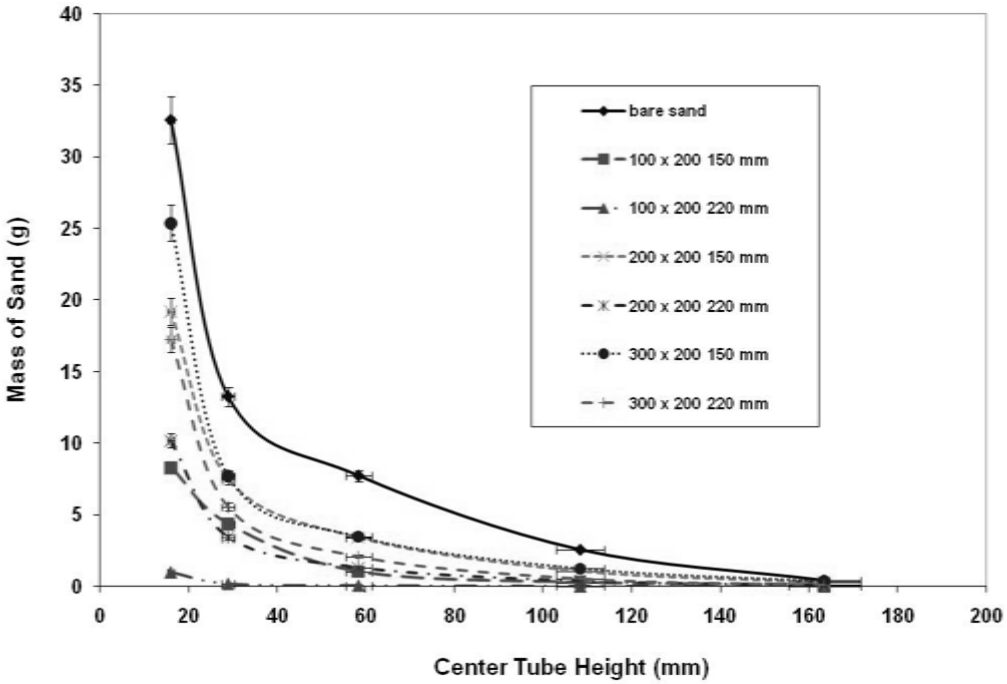

Figure 3.7. Center tube sand catch profiles (mean value for three replicates) at 11 m s^{-1} wind speed.

A comparison of wind speed with sand discharge (Figure 3.8) showed a difference in level of sheltering between the two (150 and 220 mm) leaf heights. For both heights, less sand discharge was observed with the denser configuration. Less steep curves were observed for taller leaf height configurations, which indicates greater sheltering was provided by all configurations with taller standing vegetation; taller vegetation resulted in reduced sand discharge at the end of the tunnel.

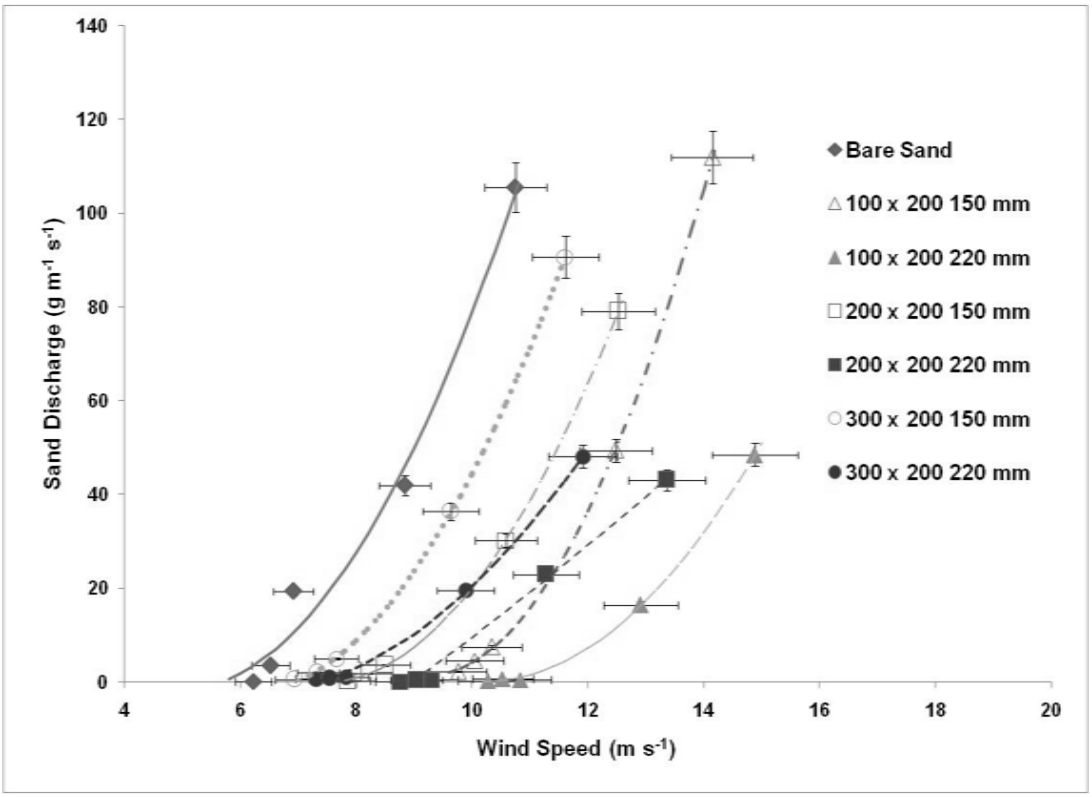

Figure 3.8. Mean sand discharge (three replicates) at various wind tunnel free stream velocities.

The greater the wind speed, the taller canopies' (220 mm) potential for reducing friction velocity was observed compared to the shorter canopies' (150 mm), which showed a potential to retard saltation at the sand surface. This is brought about by better sheltering by the taller canopies. This potential to decrease surface friction velocity is evident in the relatively less steep curve produced by the taller canopies in Fig. 3.8. The same trend for reducing surface friction velocity was observed by Hagen and Casada (2013) using simulated dicotyledonous plants.

3.3.3. Abrasion Energy Assessment

A comparison of the mean abrasion losses for all configurations for both low and high wind speeds are given in Table 3.4. The majority of configurations differed significantly ($p < 0.05$) from bare sand except for the 300 × 200 mm configuration for both heights, 150 and 220 mm, and the 200 × 200 mm configuration at 150 mm height.

Table 3.4. Mean abrasion mass loss per unit mass of sand abrader for six configurations.

Maximum leaf height (mm)	Tunnel configuration	Low free stream wind speed ($m\ s^{-1}$)	Low wind speed abrasion loss ($g\ g^{-1}$)	High free stream wind speed ($m\ s^{-1}$)	High wind speed abrasion loss ($g\ g^{-1}$)
bare sand	bare sand	8.84	0.009 [a]	10.75	0.015 [a]
150	100 × 200	12.48	0.005 [b]	14.15	0.008 [b]
150	200 × 200	10.59	0.006 [b]	12.53	0.009 [b]
150	300 × 200	9.63	0.008 [a]	11.61	0.013 [a]
220	100 × 200	12.91	0.003 [b]	14.89	0.006 [b]
220	200 × 200	11.28	0.004 [b]	13.37	0.008 [b]
220	300 × 200	9.89	0.006 [a]	11.91	0.011 [a]

[*] **Different letters in the same column indicate significant difference ($p < 0.05$).**

Table 3.4 shows a decreasing trend in total kinetic energy (mass loss) for each specific height with increasing standing vegetation density in the tunnel. Even at low wind speeds (8.84 $m\ s^{-1}$), abrasion loss for the bare sand was high (0.009 $g\ g^{-1}$) compared with other configurations (except the 300 × 200 mm configuration at 150 mm canopy height). A good example of greater sheltering by vegetation is the 100 × 200 mm configuration at 220 mm height, where half of the abrasion loss experienced at the bare sand configuration at 11 $m\ s^{-1}$ was experienced at a wind speed value of 15 $m\ s^{-1}$.

The presence of artificial standing vegetation within the tunnel produced lower values of C_{an} (Table 3.5). C_{an} of the bare sand configuration differed significantly ($p < 0.05$) from all other configurations, indicating that artificial standing vegetation minimized abrasion, which is the

same observation as Hagen and Casada (2013) for simulated dicotyledonous plants. The densest configuration (100 × 200 mm) was significantly different ($P < 0.05$) from the two other less dense configurations. This difference in C_{an} values resulted in a significant decrease in the abrasion coefficients, which could be associated with lower saltation discharge due to better sheltering. However, there was no significant difference between the taller (220 mm) and shorter (150 mm) heights in terms of abrasion coefficient values.

Table 3.5. Mean abrasion coefficients (C_{an}) and SEM values of standing vegetation configurations using horizontal abrasion plates.

Configuration	Abrasion coefficient (C_{an})	
	150 mm vegetation height	220 mm vegetation height
100 × 200	0.00425 ± 0.00007 [b]	0.00420 ± 0.00008 [b]
200 × 200	0.00485 ± 0.00016 [b]	0.00479± 0.00026 [b]
300 × 200	0.00540 ± 0.00001 [a]	0.00515 ± 0.00001 [a]
Bare sand	0.00648 ± 0.00024 [a]	

[*] **Different letters in the same column indicate significant difference ($p < 0.05$).**

The values of C_{an} were evaluated in relation to wind speed in Table 3.6. There was no significant difference ($P > 0.05$) in the values of C_{an} between the two wind speeds (low wind speed refers to measurements at 0.75 m s^{-1} above threshold while high wind speed to measurements at 5 m s^{-1} above threshold) for the tested configurations. There was also no significant difference between C_{an} values between the two heights with the same configuration. However, the most dense configuration (100 × 200 mm) was significantly different ($p < 0.05$) from the least dense (300 × 200 mm) for both heights tested. The lower values of C_{an} for the most dense configuration reflects the better sheltering offered by the dense configuration that was able to impede the movement of saltating particles (less kinetic energy transfer) more effectively than the least dense configuration. As a result, less abrasion was experienced, which could be due to the reduced amount of saltating particles hitting the abrasion sensor.

Table 3.6. Comparison of abrasion coefficients (C_{an}) of standing vegetation configurations at various wind speeds using horizontal abrasion plates.

Configuration	Abrasion coefficient (C_{an})			
	150 mm vegetation height		220 mm vegetation height	
	Low wind speed	High wind speed	Low wind speed	High wind speed
100 × 200	0.00424[a]	0.00434[a]	0.00420[a]	0.00430[a]
200 × 200	0.00470[b]	0.00507[b]	0.00458[b]	0.00503[b]
300 × 200	0.00539[b]	0.00541[b]	0.00513[b]	0.00516[b]

[*] **Different letters in the same column indicate significant difference ($p < 0.05$).**

3.4. Conclusions

Wind erosion parameters such as wind profiles, sand discharge, and abrasion energy were measured for simulated standing vegetation in a laboratory wind tunnel. The following conclusions were found:

- In general, canopy aerodynamic roughness was greater for the taller (220 mm) standing vegetation, which effectively promotes greater canopy sheltering downwind. This was evident from the greater threshold wind speeds of the taller standing vegetation for the wind tunnel configurations used in the experiment.
- Sand discharge depended on canopy density and height within the tunnel; the denser the canopy, the less sand discharge was observed. This effect of canopy density on sand discharge was true for both canopy height configurations.
- The abrasion coefficient was independent of wind speed, but was more dependent on the density of canopy. As the canopy density increases, both the wind profile and saltation behavior were changed, which caused less impact of saltating particles on the canopy and, thus, lower abrasion coefficients.

It was also observed that simulated young monocotyledonous plants did not intercept much of the saltating particles compared to simulated young dicotyledenous plants because of their relative difference in leaf structure for the younger stages of the plants. The measured wind

profiles for this experiment will be used in the validation of the numerical simulation study of airflow around canopies at different heights and configuration for the actual three-dimensional structure of the artificial standing vegetation. Such study will be essential in determining the needed structure to further protect young canopies within a field setting that will minimize abrasion damage to it by wind erosion.

3.5. References

ADInstruments. 2009. Pressure transducer calibration. Tech Note. 1-2. http://cdn.adinstruments.com/adi-web/techniques/tn-PressureTransducerCal-FAQ.pdf.

Aggarwal, C.C. 2013. Outlier analysis. Springer, New York.

Baker, J.T., McMichael, B.L., Burke, J.J., Ephrath J., Gitz, D.C., & Lascano, R.J. 2009. Sand abrasion injury and biomass partitioning in cotton seedlings. *Agron. J.* 101(6), 1297-1303.

Bao Y., Li, H., & Yang J. 2009. Effects of shelterbelts on wind erosion control in the desertified cropland of north-western Shandong Province, China. In *Bioinformatics and Biomedical Engineering, (iCBBE) 2011 5th International Conference.* 10-12 May, Wuhan, China.

Belnap, J. & Gillette, D.A. 1998. Vulnerability of desert biological soil crusts to wind erosion: the influences of crust development, soil texture, and disturbance. *J. Arid Environ.* 39(2): 133-142.

Bielders, C.L., Michels, K., & Rajot, J.L. 2000. On-farm evaluation of ridging and residue management practices to reduce wind erosion in Niger. *Soil Sci. Soc. Am. J.* 64: 1776-1785.

Bisal, F. 1968. Influence of plant residue on sand flow in a wind tunnel. *Can. J. Soil Sci.* 48(1): 49-52.

Bowker, G.E., Gillette, D.A., Bergametti, G., Marticorena, B., & Heist, D.K. 2008. Fine-scale simulations of aeolian sediment dispersion in a small area in the northern Chihuahuan Desert. *J. Geophys. Res.* 113(F02S11): 1-12.

Burri, K., Gromke, C., Lehning, M., & Graf, F. 2011. Aeolian sediment transport over vegetation canopies: A wind tunnel study with live plants. *Atmos. Environ.* 3(2): 205-213.

Cardillo, G. 2006. Holm-Sidak t-test: a routine for multiple t-test comparisons. http://www.mathworks.com/matlabcentral/fileexchange/12786.

Cornelis, W.M. & Gabriels, D. 2005. Optimal windbreak design for wind-erosion control. *J. Arid Environ.* 61(2): 315-332.

Dong, Z., Gao, S., & Fryrear, D.W. 2001. Drag coefficients, roughness length and zero-plane displacement height as disturbed by artificial standing vegetation. *J. Arid Environ.* 49(3): 485-505.

Farmer, A.M. 1993. The effects of dust on vegetation - A review. *Environ. Pollut.* 79(1): 63-75.

Genis, A., Vulfson, L., & Ben-Asher, J. 2012. Combating wind erosion of sandy soils and crop damage in the coastal deserts: Wind tunnel experiments. *Aeolian Res.* 9: 69-73.

Gomes, L., Arŕue, J.L., López, M.V., Sterk, G., Richard, D., Gracia, R., Sabre, M., Gaudichet, A., & Frangi, J.P. 2003. Wind erosion in a semiarid agricultural area of Spain: the WELSONS project. *Catena.* 52: 235-256.

Greeley, R. & Iversen, J.D. 1985. Wind as a geological process. New York: Cambridge University Press.

Hagen, L.J. & Casada, M.E. 2013. Effect of canopy leaf distribution on sand transport and abrasion energy. *Aeolian Res.* 10: 37-42.

Hagen, L.J. 2001. Assessment of wind erosion parameters using wind tunnels. In *Sustaining the Global Farm,* Scott D.E., Mohtar, R.H., Steinhardt G.C. (eds.), 10th International Soil Conservation Organization Meeting, Purdue University and USDA-ARS National Soil Erosion Research Laboratory, 1999; 742-746.

Hassine, A.B. & Lutts, S. 2010. Differential responses of saltbush *Atriplex halimus L.* exposed to salinity and water stress in relation to senescing hormones abscisic acid and ethylene. *J. Plant Physiol.* 167(17): 1448-1456.

Hyams, D.G. 2013. Curve expert 1.4 software. www.curveexpert.net

Lal, R. 2001. Soil degradation by erosion. *Land Degrad. Develop.* 12: 519-539.

Larney, F.J., Bullock, M.S., Janzen, H.H., Ellert, B.H., & Olson, E.C.S. 1998. Wind erosion effects on nutrient redistribution and soil productivity. *J. Soil Water Conserv.* 53(2): 133-140.

Ling, C.H. 1976. On the calculation of surface shear stress using the profile method. *J. Geophys. Res.* 15: 2581-2582.

Lyles, L. 1975. Possible effects of wind erosion on soil productivity. *J. Soil Water Conserv.* 30(6): 279-283.

Lyles, L. & Allison, B.E. 1976. Wind erosion: The protective role of simulated standing stubble. *Trans. ASAE.* 19(1):61-64.

Lyles, L. & Allison, B.E. 1981. Equivalent wind-erosion protection from selected crop residues. *Trans. ASAE.* 24(2): 405-408.

Marticorena, B., Bergametti, G., Gillette, D., & Belnap, J. 1997. Factors controlling threshold friction velocity in semiarid and arid areas of the United States. *J. Geophys. Res.* 102(D19): 23,277-23,287.

Masle, J. & Passioura, J.B. 1987. The effect of soil strength on the growth of young wheat plants. *Aus. J. Plant Path.* 14(6): 643-656.

Merrill, S.D., Black, A.L., Fryrear, D.W., Saleh, A., Zobeck, T.M., Halvorson, A.D., & Tanaka, D.L. 1999. Soil wind erosion hazard of spring wheat-fallow as affected by long-term climate and tillage. *Soil Sci. Soc. Am. J.* 63: 1768-1777.

Michels, K., Sivakumar, M.V.K. & Allison, B.E. 1995a. Wind erosion control using crop residue I. Effects on soil flux and soil properties. *Field Crops Res.* 40(2): 101-110.

Michels, K., Sivakumar, M.V.K., & Allison, B.E. 1995b. Wind erosion control using crop residue II. Effects on millet establishment and yields. *Field Crops Res.* 40(2): 111-118.

Molion, L.C.B. & Moore, C.J. 1983. Estimating the zero-plane displacement for tall vegetation using a mass conservation method. *Boundary Layer Meteorol.* 26(2): 115-125.

Raupach, M.R. 1992. Drag and drag partition on rough surfaces. *Boundary Layer Meteorol.* 60(4): 375-395.

Shaw, R.H., Brunet, Y., Finnigan, J.J., & Raupach, M.R. 1995. A wind tunnel study of airflow in waving wheat: Two-point velocity statistics. *Boundary Layer Meteorol.* 76: 349-376.

Shinoda, M., Gillies, J.A., Mikami, M., & Shao, Y. 2011. Temperate grasslands as a dust source: Knowledge, uncertainties, and challenges. *Aeolian Res.* 3(3): 271-293.

Skidmore, E.L., Kumar, M., & Larson, W.E. 1979. Crop residue management for wind erosion control in the Great Plains. *J. Soil Water Conserv.* 34(2): 90-94.

Thom, A.S. 1971. Momentum absorption by vegetation. *Quart. J. R. Met. Soc.* 97: 414-428.

Toure, A.A., Rajot, J.L., Garba, Z., Marticorena, B., Petit, C., & Sebag, D. 2011. Impact of very low crop residues cover on wind erosion in the Sahel. *Catena.* 85: 205-214.

Woodruff, N.P., Lyles, L., Dickerson, J.D., & Armbrust, D.V. 1974. Using cattle feedlot manure to control wind erosion. *J. Soil Water Conserv.* 29(3): 127-129.

Yousef, F., Visser, S.M., Karssenberg, D., Erpul, G., Cornelis, W.M., Gabriels, D., & Poortinga, A. 2012. The effect of vegetation patterns on wind-blown mass transport at the regional scale: A wind tunnel experiment. *Geomorph.* 159-160: 178-188.

CHAPTER 4 - Porosity and Drag Determination of a Single Row Shelterbelt (*Maclura pomifera*)

4.1. Introduction

Arid and windy regions, such as the Great Plains in the United States, are susceptible to wind erosion. Methods such as conservation tillage, strip cropping, and vegetative barriers have been implemented to minimize wind erosion effects. Farmers often use vegetative barriers (also called windbreaks or shelterbelts) because they are perceived to improve aesthetics of farm land and shelter downwind crops from wind erosion. Other benefits of shelterbelts include changing microclimate of soils (Cleugh, 1998; Campi et al., 2009), increased crop yield (Sun and Dickinson, 1997; Sudmeyer et al., 2002), crop protection (Kort, 1988; Bird et al., 1992), restoration of soil fertility (Sudhishri et al., 2008), livestock protection (Gregory, 1995; Ffolliott, 1998), increased livestock performance (Mader et al., 1999), and aesthetic benefits (Burel and Baudry, 1995; Grala et al., 2010).

Shelterbelt effectiveness is commonly measured by its sheltering efficiency downwind of the barrier via reduced wind speed (Kozmar et al., 2012). This effectiveness is dependent on factors such as the tree species, shape, height, length, width, orientation, canopy density, and porosity (Brandle et al., 2004; Cornelis and Gabriels, 2005; Koh et al., 2014). Porosity is an essential parameter that defines the relative sheltering efficiency of shelterbelts (Hagen and Skidmore, 1971). Solid barriers promote excessive recirculation (zones of low velocity and increased turbulence) upwind and downwind of the barrier (Stunder and Arya, 1988). However, porous barriers do not experience recirculation as long as the porosities would not promote or limit recirculation (Hagen and Skidmore, 1971; Wilson, 1987; Cornelis and Gabriels, 2005). Excessively low porosity induces fast recovery of leeward wind speed, potentially promoting

increased turbulence similar to a solid barrier, but excessively high porosity is unnecessary because it does not effectively shelter the leeward side of a shelterbelt.

Both aerodynamic (α_p) and optical (β_p) porosities of the shelterbelt can be defined. Aerodynamic porosity (volumetric porosity) is the true porosity, which considers the complete three-dimensionality of shelterbelts but is difficult to compute. According to Heisler and Dewalle (1988), α_p can be approximated from β_p for narrow and thin shelterbelts. Thus, optical porosity is a two-dimensional approximation of the true porosity. A thin shelterbelt is defined as a shelterbelt across which wind variation is negligible due to the small ratio of shelterbelt width to its height (Wilson, 2005; Bouvet et al., 2007). Guan et al. (2003) gave the following equation for α_p:

$$\alpha_p = \frac{\int_0^H \bar{u} dz}{\int_0^H \bar{u}_0 dz} \tag{4.1}$$

where H is the height of the barrier, $\bar{u}$ is the leeward (bleed speed) wind speed, and $\bar{u}_0$ is the mean windward wind speed. Optical porosity is obtained from the following equation:

$$\beta_p = \frac{(Background\ area)}{(Total\ area)} \tag{4.2}$$

Guan et al. (2003) obtained the background area (representing gaps outside the area occupied by the tree including leaves, branches, stems, and trunk) from image analysis of digitized photographs. They used a systematic approach of taking photographs of tree sections in accordance with guidelines proposed by Loeffler et al. (1992). Although β_p is convenient to use because it does not require wind measurement, a relationship between α_p and β_p is necessary, especially for deciduous trees that experience porosity variations throughout the year.

Accurate choice of barrier species is essential for alleviating the effects of wind erosion (Hagen and Skidmore, 1971; Steffens et al., 2012). Although numerous studies of shelterbelts

have been conducted, the structure complexity of various tree species has led to limited research on shelterbelt types that have been established on the perimeter of agricultural lands in Kansas. Barrier porosity is specific to the tree type (Hagen and Skidmore, 1971; Wang and Takle, 1996; Vigiak et al., 2003; Bitog et al., 2011; Koh et al., 2012) due to variety of shape, height, and porosity dictated by various foliage structures. The Osage orange (*Maclura pomifera*) tree, or hedge apple, a common shelterbelt in Kansas, is a species that does not shed its leaves during the dormant season (deciduous). This tree can grow to a height of 8 - 15 m with round, bumpy fruit that measures 7 - 16 cm in diameter. Although use of Osage orange as a shelterbelt is prevalent in agricultural lands in Kansas, limited information is available on its sheltering efficiency and aerodynamic properties. In addition to defining seasonal changes that this species of tree experiences yearly, a need exists to define the aerodynamic parameters that characterize Osage orange's effectiveness as shelter for crops and soil downwind during its two leaf conditions: leaf-on and leaf-off.

Specific objectives of the study were to:

1) determine optical porosity of Osage orange barrier section using image analysis;
2) determine aerodynamic porosity and drag coefficients of Osage orange during leaf-on and leaf-off conditions using wind profile measurements; and
3) measure the effects of shelterbelt leaf condition on wind speed reduction.

4.2. Materials and Methods

4.2.1. Site Description

This research was conducted from October 2013 to December 2013 at a farm near Riley, Kansas (39°18'49.1"N 96°54'29.2"W) where Osage orange was used as the shelterbelt (Figure 4.1).

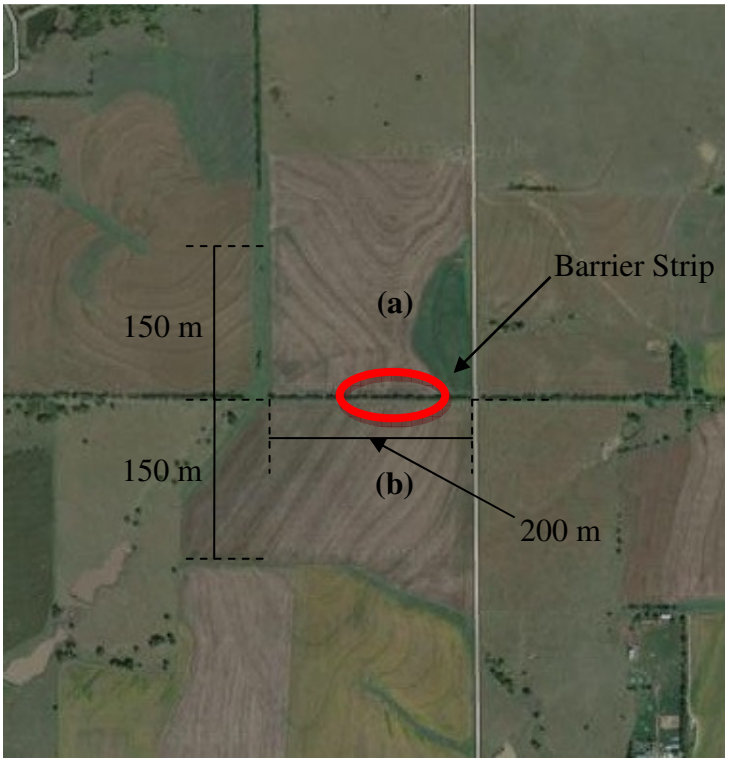

Figure 4.1. Aerial view of the field site (via Google Maps): (a) north side and (b) south side.

The site was chosen based on the following criteria proposed by Loeffler et al. (1992): (a) flat terrain to avoid topographical effects on wind speed patterns close to the shelterbelt; (b) absence of obstructions such as buildings near the vicinity to avoid adverse effects on wind speed patterns along the shelterbelts; (c) similar vegetation height on both sides of the shelterbelt to maintain constant surface roughness; and (d) minimum length:height ratio of 10:1 to avoid edge and vortex effects at the ends of the shelterbelt.

The chosen fields were not completely flat (slight angle of 10°), but the towers were placed at angled regions and the cup anemometers were horizontally aligned as wind measurements were taken. The two fields with the shelterbelt separating them in the middle was

located at an elevation of 508 m, had total dimensions of 300 m in length (north to south), 200 m (east to west) in width. Field crops grown in the rotation included winter wheat, corn, and sorghum. In addition to a shelterbelt within the field, no-till management was employed to minimize the effects of wind erosion and improve field production. The experimental shelterbelt row (running from east to west) was located between two fields designated as south side (upwind field) and north side (downwind field) (Figure 4.1). The average measured tree height (H) was H = 8.5 m ± 0.6 m, which was used as a basis in data analysis. During the field measurement for the leaf-on stage of the Osage orange barrier, the west side of the downwind field was planted with wheat, so wind speeds were determined at the eastern portion of the downwind field where live soybean stubble was present at the time (freshly harvested soybean about 0.1 m height); the upwind field was bare at the time of sampling. During the leaf-off stage of testing, the downwind field had dead soybean stubble at the east side, while the east side of the upwind field was freshly planted with wheat (0.05 m). Figure 4.2 shows the leaf-on and leaf-off stages during measurements.

Prevailing wind directions for the field site were south-southwest for the summer and north-northwest for the winter. Data were collected in the presence of a direct south wind or a south-southwest wind for both tests (summer and fall).

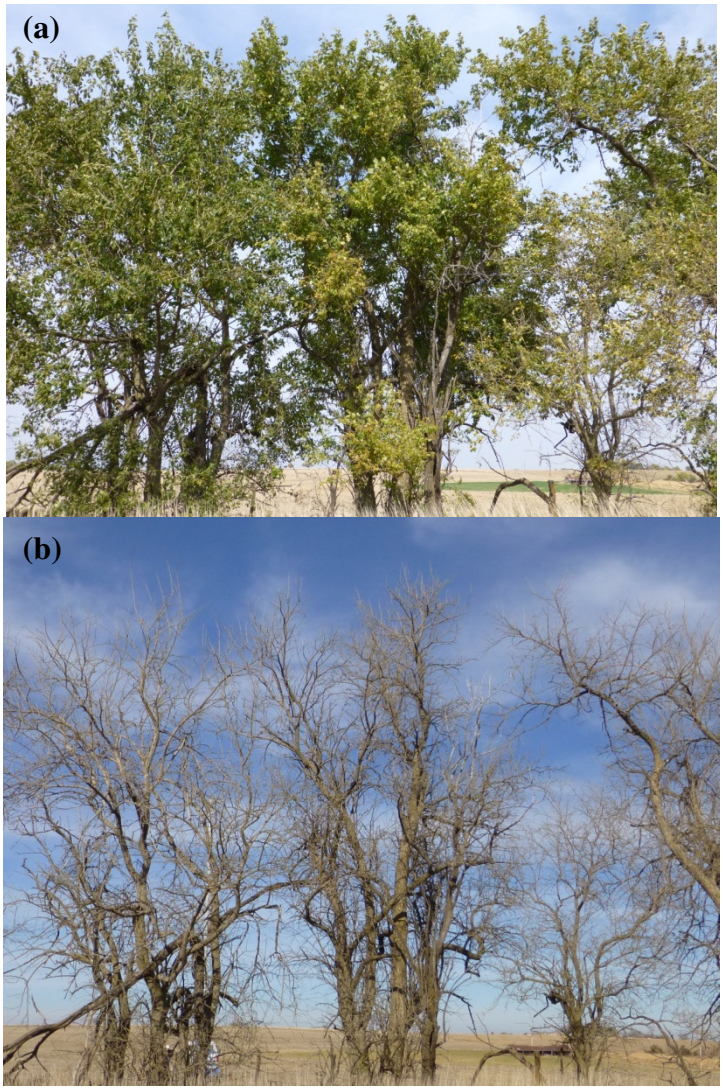

Figure 4.2. Leaf-on (a) and leaf-off (b) conditions tested for the Osage orange barrier.

4.2.2. Wind Profiles

Two towers were positioned with one on each side of the shelterbelt. Given the prevailing winds, the north side was chosen as the downwind side and the south side was chosen as the upwind side. The downwind tower was a movable tower placed at 1, 2, 4, 7, 10, 15, and 20H away from the chosen barrier section, based on distances used by Stredova et al. (2012). Distances of 15H and 20H were included to determine the extent of wind speed recovery

downwind. This tower was equipped with Sierra Misco 1005 DC (NovaLynx Corporation, CA) cup anemometers installed on mounting arms along the height of the tower (Figure 4.3) at heights of 1.5, 3.35, 4.9, 6.4, 8.2, and 15 m above ground. The upwind tower was a stationary tower located 85 m upwind from the barrier. The upwind tower was also equipped with cup anemometers installed along the height of the tower similarly to the downwind tower (Figure 4.3) but including an additional cup anemometer at 18 m above the ground.

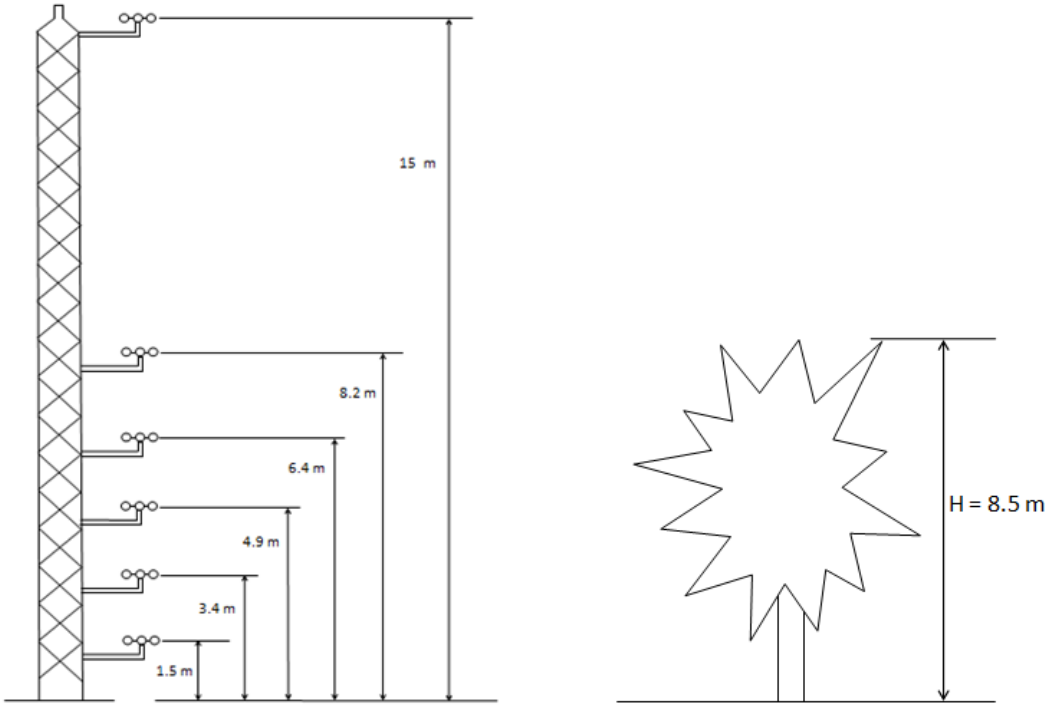

Figure 4.3. Schematic diagram for the cup anemometer placed on upwind and downwind towers.

Anemometer heights in the field were similar to heights used by Sellier et al. (2008). Wind profiles were recorded continuously for 10 min and replicated three times for each distance downwind from the shelterbelt. The set of six cup anemometers was connected to a Universal Serial Bus (USB) Data Acquisition (DAQ) Board (Model 2408, Measurement Computing) that was then connected to a laptop loaded with LabView software (LabView 2012, Professional

Edition) to monitor and record real-time wind speed data. The DAQ board had 16 single-ended (8 differential) analog inputs, 24-bit resolution for ultra-accurate voltage measurement up to 1 kS/sec.

4.2.3. Calibration of Anemometers

Prior to mounting on the towers, the cup anemometers were calibrated to wind speeds measured with pitot-static tubes in the outdoor wind tunnel of the USDA – ARS in Manhattan, Kansas. Pitot tubes were attached to pressure transducers calibrated using surgical syringes and a Dwyer inclined manometer air-filter gauge (Model Series 250-AF) to ensure stable pressure and voltage readouts during measurements. Values were then converted to digital output via a Labview program (Labview Student Ver. 2012, National Instruments, CA). The anemometers were individually tested as well as side by side in the tunnel through a range of velocities (2 m s^{-1} to 15 m s^{-1}). The anemometers that were placed adjacent to each other within the tunnel during calibration showed a noticeable effect to the recorded free stream velocity (recorded wind velocities were lowered for each anemometer that tested side by side). Therefore, the calibration data for individually placed anemometers within the tunnel were used. Voltage corresponding to the degree of spin (i.e., voltage ranging from 1.5 V to 3.3 V, corresponding to 310 to 630 rpm) for each cup anemometer was the basis of calibration.

4.2.4. Porosity Determination

Optical and aerodynamic porosity measurements were compared. To estimate β_p, two image analysis methods done using both software products (SigmaScan Pro and MATLAB) were evaluated, and porosity values were compared for leaf-on and leaf-off conditions of the Osage orange tree barrier. Photographs (captured using a 14.1 mega pixel Panasonic Lumix ZS20

camera (Panasonic, Corp.) with a 24 mm wide angle lens that has a 14.1 mega pixel 1/2.33"-type metal oxide semiconductor (MOS) sensor and optical zoom lens of 20x (24-480 mm)) of trees were taken in accordance with Kenney's (1987) guidelines in which photos were taken one tree height away from the barrier strip and during calm conditions. As mentioned by Zhu (2008), photos were not taken in the presence of excessive brightness (light condition which could increase reflection from tree elements thus promoting overexposure and unbalanced color of photographs when processed). Photographs considered for β_p computation were cropped from the ground to the apex of the Osage orange crown, similar to the method of Vigiak et al. (2003).

Figure 4.4 shows examples of digital image analysis using SigmaScan Pro and MATLAB. Sigmascan Pro was used to analyze digital images of true red, green, blue (RGB) model color and determine optical porosity value by separating the background (white) from the foreground (red) areas represented by the number of pixels. Total area determined to be the total number of pixels in the original photograph and background area was obtained by the difference between the total area pixels of the original image and the foreground area pixels.

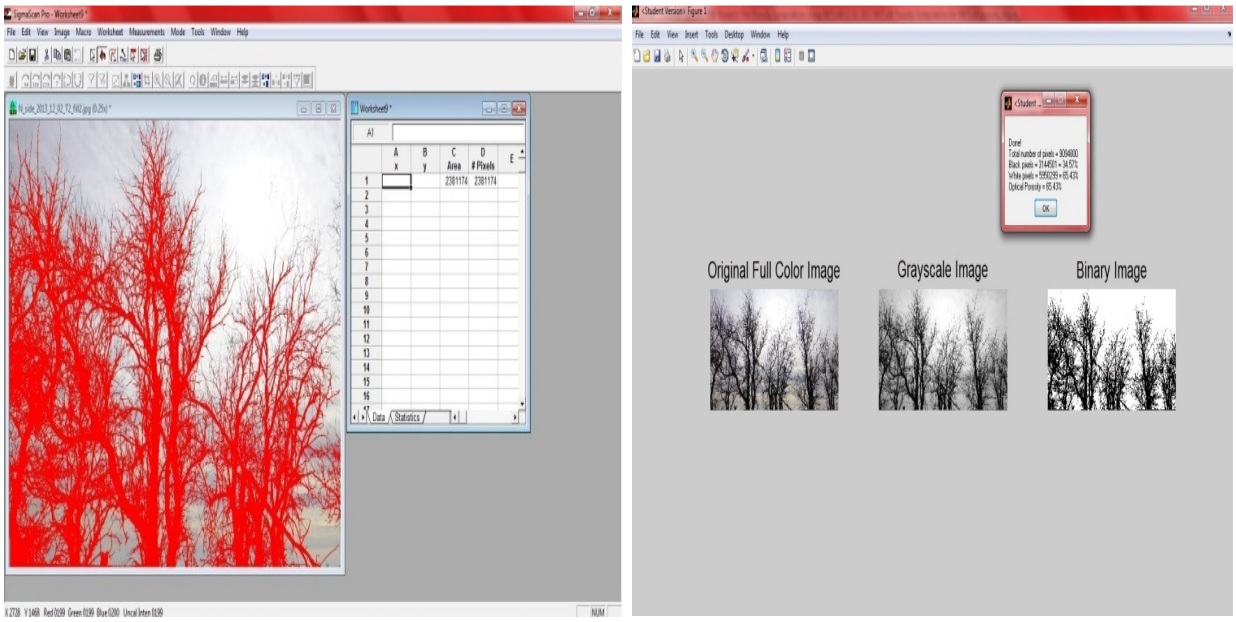

Figure 4.4. Optical porosity determination using SigmaScan Pro and MATLAB.

In contrast, the MATLAB image analysis toolbox (programmed and executed to analyze binary images) converted the original image to grayscale and then to binary images of specific pixel numbers that comprise the total area, background area, and foreground area in which β_p computation is performed.

The two image analysis procedures differ in that MATLAB uses the original color photograph that must be converted to a grayscale image and then to a binary image (black and white) before recognizing the background (white) from foreground (black) areas. SigmaScan Pro performs an immediate identification of foreground pixels after identifying the representative pixel color for the foreground that serves as the threshold pixel value. The selected object and other objects that surpass the threshold pixel value are then filled with red color. If some portions of the original image are still not separated from the background, further separation can be done by continuously clicking the desired object to be included as the foreground. Foreground selection is often dependent on the type of picture being considered (i.e., presence of small branches greatly affects picture threshold selection).

Computation for α_p was based on the ratio of the mean downwind to upwind velocities (Guan et al., 2003; Bitog et al., 2011). For thin shelterbelts (single row), Heisler and Dewalle (1988) stated that α_p and $\beta_p$values can approximate each other. Discrepancies between α_p and β_p values occur due to inherent porosities and obscuration of light elements by leaves and branches (Grant and Nickling, 1998). In a field setting, wind velocities vary from the ground surface upwards; therefore, values of α_p also vary depending on the selected H value (H = 8.5 m for this study).

4.2.5. Shelterbelt Drag Coefficient

Based on measured values of wind velocities, shelterbelt drag is measured by how much resistance the trees offer towards the incoming airflow (upwind air) in terms of the drag coefficient (C_D). Raine and Stevenson (1977) stated that changes in airflow through shelterbelts are described by momentum shifts within the barrier as the barrier resists the incoming airflow.

From available literature, C_D can be computed as the ratio of wind load and dynamic force upwind of the barrier (Cullen, 2005; Koizumi et al., 2010; Bitog et al., 2011). For field conditions, the method of Hagen and Skidmore (1971) based on Woodruff et al. (1963) methodology was adapted due to its simplicity and applicability, where the drag coefficient is estimated using the following equation:

$$C_D = \frac{2D_b}{(\rho_{air}\bar{u}^2 H)} \tag{4.3}$$

where D_b is the drag force of the shelterbelt, H is the shelterbelt height, ρ_{air} is air density, and $\bar{u}$ is mean upwind wind speed over the wake depth.

Wake depth is the vertical distance at which upwind velocity is equal to downwind velocity. Drag force was obtained using the difference of momentum transfer between the upwind and downwind sides of the barrier, as explained by Woodruff et al. (1963) and defined by the following equation:

$$D_b + D_g = \int_0^z \left[\left(P_{up} + \frac{1}{2}\rho_{air}u_{up}^2\right) - \left(P_{down} + \frac{1}{2}\rho_{air}u_{down}^2\right)\right] dz \tag{4.4}$$

where D_p is drag force of the barrier, D_g is drag force of the ground, z is vertical distance along the barrier height, P_{up} and P_{down} are pressure values upwind and downwind, and u_{up} and u_{down} are wind velocities upwind and downwind of the shelterbelt. To calculate the drag coefficients, a simplified equation derived by Hagen and Skidmore (1971) was used to neglect pressure effects

assuming that the ground drag was negligible compared to the barrier drag (Eq. 4.5). Values for the drag coefficients computed for this study were based on drag forces calculated using downwind velocities at the 7H and 10H distances away from the barrier to obtain a valid assumption that pressure forces are negligible and that no end effects were present for the shelterbelt (Hagen and Skidmore, 1971).

$$D_b = \int_0^z \left[\left(\frac{1}{2\rho_{air}u_{up}^2}\right) - \left(\frac{1}{2\rho_{air}u_{down}^2}\right)\right] dz \quad (4.5)$$

4.2.6. Meteorological Data

To monitor weather data at the site, a weather station (Model Vantage Pro2, Davis Instruments) was equipped with a solar panel and an integrated sensor suite consisting of temperature and humidity sensors, anemometer, and rain gauge. A weather-resistant shelter housed electronic components within the sensor suite operated via solar power. A battery-operated wireless console (with a range of wireless connection up to 300 m) gathered data from the weather station.

4.2.7. Data Analysis

Data for wind profiles were screened, and wind speeds that corresponded to situations with stoppages of the cup anemometer (limited by a minimum of 2 m s^{-1}) were eliminated from analysis. Wind speed reductions were obtained from three replications of wind profiling tests at each cup anemometer level per distance away from the barrier downwind. For comparison of the two image analysis methods, optical porosities were obtained from three photographs at each location (North and South sides) for each of the leaf-on and leaf-off conditions. To compare porosities α_p and β_p, the photographs originally used for image analysis comparison were each

divided into five sections corresponding to the region or height at which the bottom five anemometers recorded data for wind speeds (a total of six anemometers were used during field tests). Computation of the drag coefficients was based on velocity profiles at the 7H and 10H profiles, corresponding to three replicates each per leaf condition. Mean values of wind velocities, optical porosities, and drag coefficients were compared using the normality and homogeneity of variances assumption, and a standard statistical test (paired t-test using Microsoft Excel (Microsoft Corp., Redmond, WA)). Analysis of variance (ANOVA) was done to determine the effect of vegetation density and heights. A 5% level of significance was used for all cases. CurveExpert 1.4 (Hyams, 2013) was used to plot best-fit curves, which were compared to the curve fitting tool in Microsoft Excel (Microsoft Corp., Redmond, WA).

4.3. Results and Discussion

4.3.1. Wind Profile

Windrose plots during the entire field tests for leaf-on and leaf-off conditions are shown in Figure 4.5. The percentages represent the amount of time the wind blew from a specific direction, and the colors indicate the magnitude of wind speed. Tests were conducted with ample wind (3 to 7 m s^{-1}) to obtain wind profiles for the various distances away from the barrier for the two leaf conditions of the Osage orange barrier. During tests for the leaf-off condition, the wind direction and speed changed more than wind profiles taken during the leaf-on condition of the Osage orange barrier. Wind speeds ranged from 6 to 7 m s^{-1} during the leaf-on condition and from 3 to 6 m s^{-1} during the leaf-off condition.

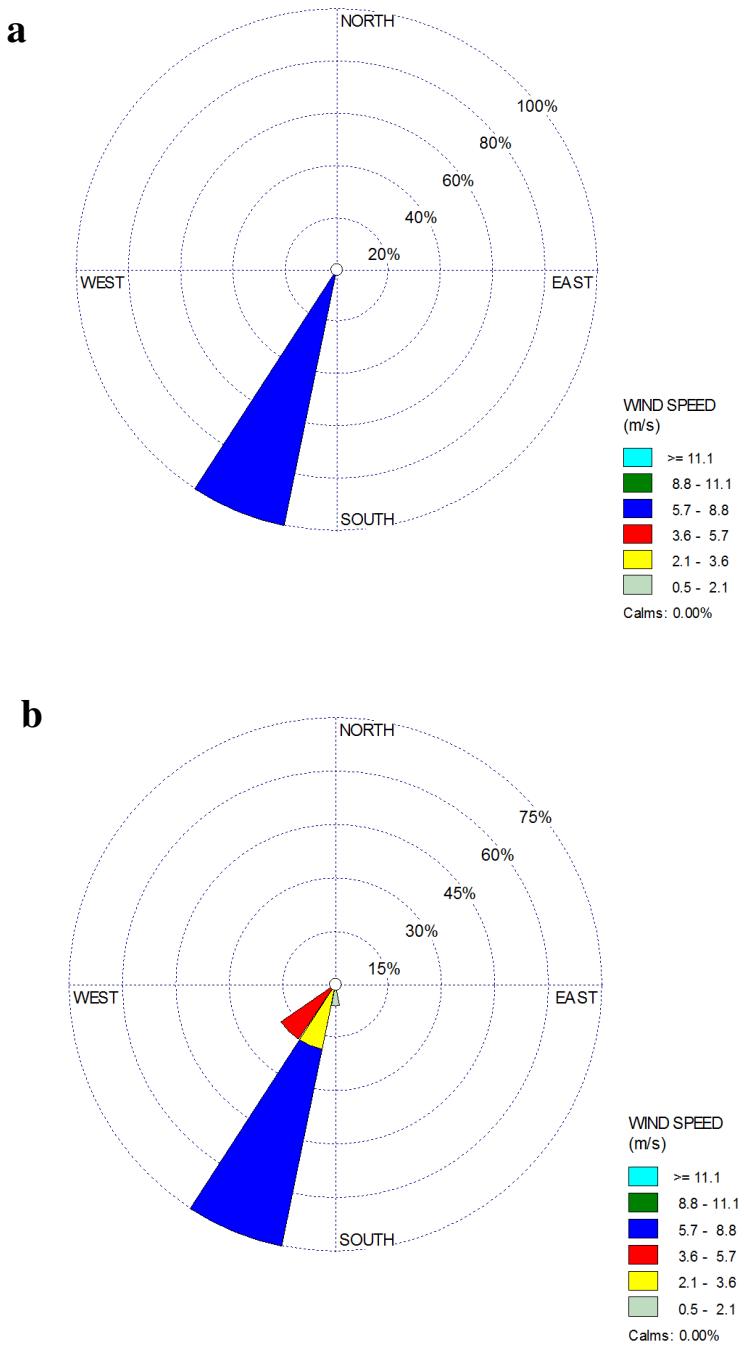

Figure 4.5. Windrose plots during field tests for (a) leaf-on and (b) leaf-off conditions of the Osage orange barrier.

A comparison of normalized wind speeds between the two leaf conditions demonstrating the effects of Osage orange barrier height downwind of the barrier strip is shown in Figure 4.6. Normalization was completed by dividing the leeward velocities (throughflow velocities, U_b) by the windward velocities; xH is the distance away from the barrier at multiples of height H. The plot was derived from the mean of three replications of wind profiles at various distances away from the barrier. Without leaves, a deciduous tree barrier, such as the Osage orange barrier, is able to lower wind speeds downwind, although not as effectively as with leaves, as evidenced by increased throughflow velocities (U_b) with respect to approach velocities ($U_{approach}$) within the barrier. In addition, velocities downwind recover faster (velocity values almost similar upwind and downwind of barrier from 12H onwards) for the leaf-off condition as compared to the leaf-on condition. In general, the Osage orange barrier effectively shelters downwind agricultural land beyond 10H which is considered a common estimate of shelterbelts' sheltering effectiveness.

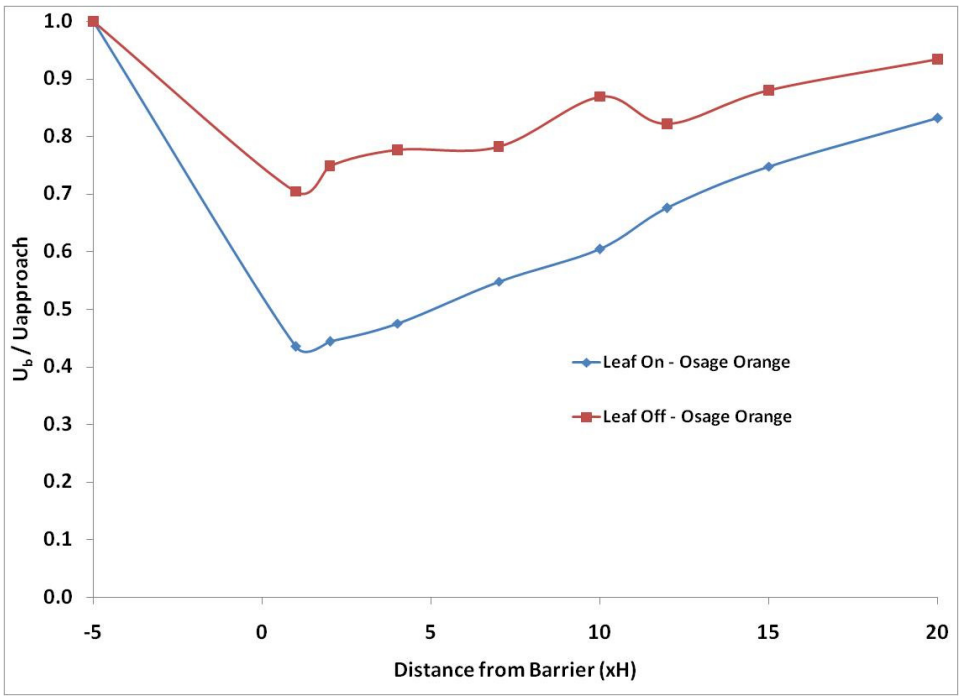

Figure 4.6. Normalized mean wind speed comparison between leaf-on and leaf-off stages of the Osage orange barrier. H is the mean tree height.

Wind speeds at heights and distances perpendicular to the Osage orange shelterbelt were taken, and speed reductions are shown in Figures 4.7 (leaf-on condition) and 4.8 (leaf-off condition). According to the wind profile of the Osage orange barrier with leaves (Figure 4.7), the reduction in wind speed occurred primarily on the middle part of the barrier at the crown (portion of tree where leaves and branches extend from the trunk). This was expected because the presence of leaves provides more obstruction of airflow compared to the lower portion of the Osage orange tree where the trunks are located and gaps exist, thereby providing less reduction in the lower portion of the barrier. Figure 4.7 shows that, for the 1H distance from the barrier row, the upper portion of the barrier (8.2 m above ground where mean barrier height is 8.5 m) had lower wind speed reduction than the middle crown portion, potentially due to faster recovery of wind speed at that height because of less leaves that retard airflow.

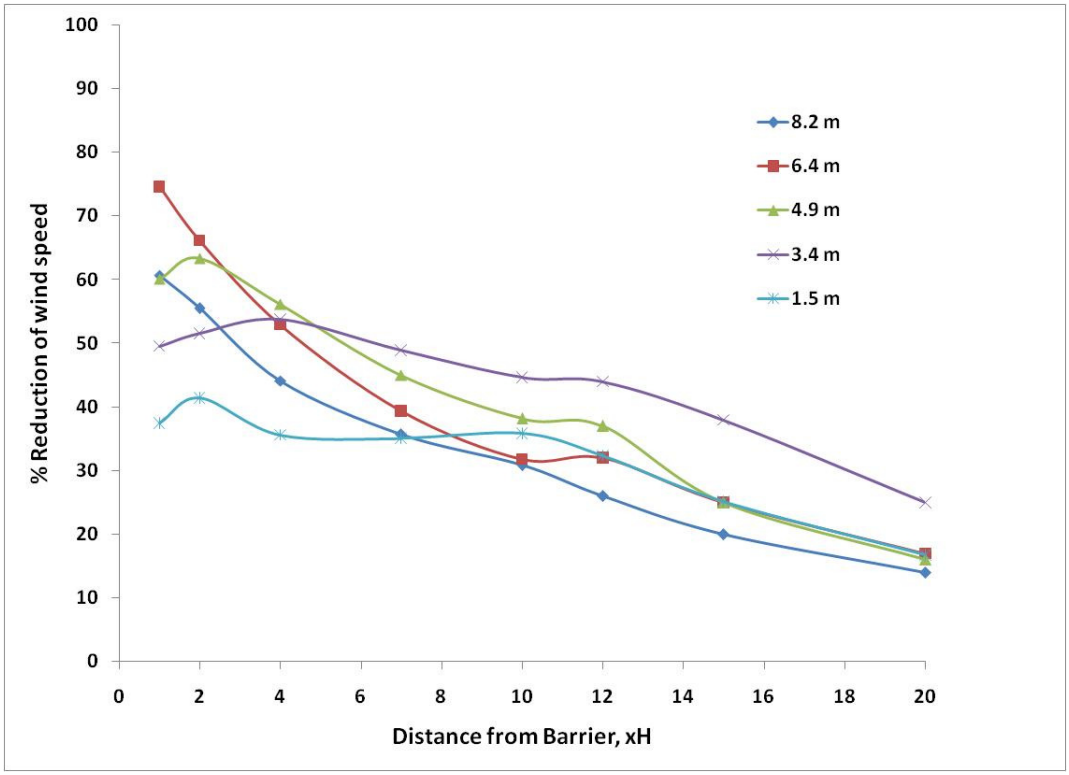

Figure 4.7. Percent reduction in wind speed downwind of the Osage orange barrier (leaf-on condition). H is the mean tree height.

For the leaf-off condition, Figure 4.8 shows that the lower portions of the barrier bring about greater lowering of wind speeds downwind of the Osage orange barrier. Because leaves were absent on the lower portion of the trees, the presence of larger branches and the trunk provided significant reduction in wind speeds, especially close to the downwind side of the barrier row as compared to the upper portion of the barrier where thinner branches did not provide significant wind speed reduction. Similar to Figure 4.5, faster re-establishment of the wind profile was achieved for the leaf-off condition because less elements (i.e., lack of leaves and presence of more gaps) hindered the flow of air and induced the formation of a recirculation zone behind the shelterbelts (Schwartz et al., 1995).

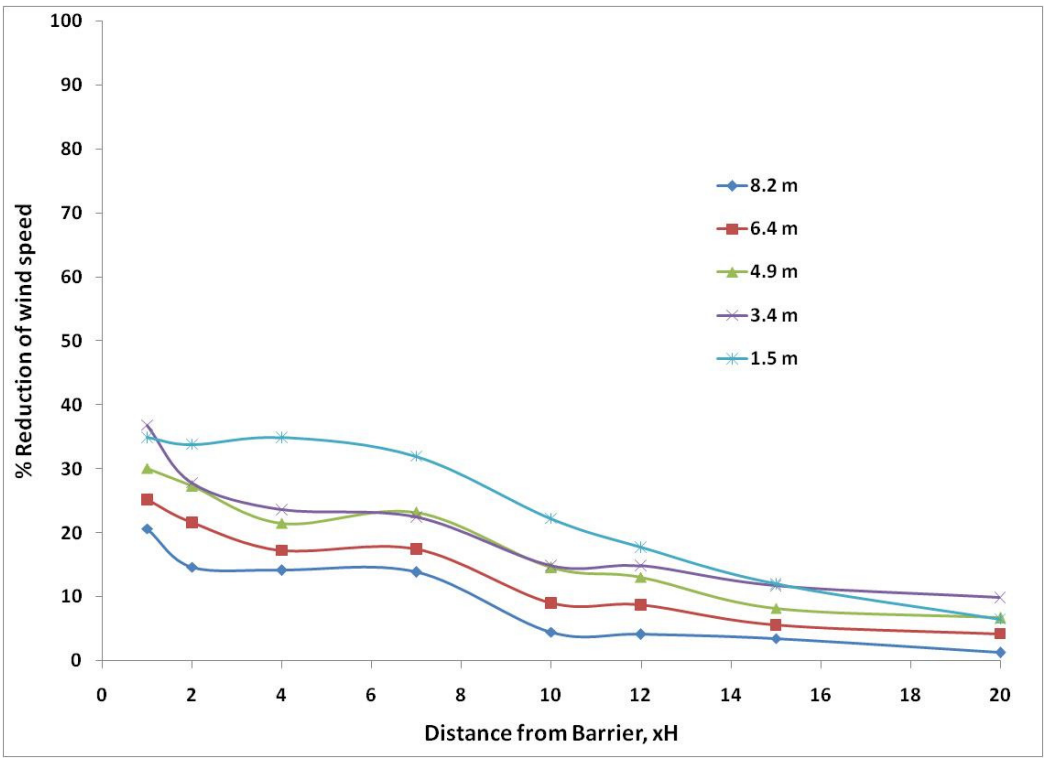

Figure 4.8. Percent reduction in wind speed downwind of the Osage orange barrier (leaf-off condition). H is the mean tree height

4.3.2. Porosity Determination

The two image analysis methods showed no significant difference ($p > 0.05$) with respect to the computed mean β_p of the Osage orange barrier for a specific barrier condition, but they showed significant difference ($p < 0.05$) between the two leaf conditions (leaf-on and leaf-off) (Table 4.1). β_p for both locations (north and south sides) where the pictures were taken also did not show any significant difference ($p > 0.05$) for a specific leaf condition. Values presented in Table 4.1 indicate the overall mean of β_p values measured based on image analysis of the entire tree.

Table 4.1. Comparison of mean optical porosities (β_p) obtained using MATLAB and SigmaScan Pro.

Photo Orientation	MATLAB	SigmaScan Pro 5
Leaf-on N Side	27.2^{Aa}	23.1^{Aa}
Leaf-off N Side	64.0^{Ba}	63.0^{Ba}
Leaf-on S Side	28.4^{Aa}	22.5^{Aa}
Leaf-off S Side	59.9^{Ba}	58.2^{Ba}

***different letters indicate significant differences from each other (uppercase letter between rows and lowercase letter between columns)**

No significant difference ($p > 0.05$) was observed for measured values between the monochrome (MATLAB) and color (SigmaScan Pro) analysis methods. Discrepancies in computed values of β_p could be due to overestimation of the β_p values using binary images in the monochrome method analysis. Results showed that the binary image produced by the monochrome method did not include portions of the original image, especially small branches and leaves that were part of the foreground. However, use of the color method allowed adjustable separation of background and foreground images by filling every pixel based on the desired RGB color model value set. (RGB calibration is done automatically by the SigmaScan Pro software when the target object or pixel in the image of specific shade is chosen). As a result,

values of β_p that were considered for the rest of this study were based on the color method analysis.

A relationship between α_p and β_p is shown in Figure 4.9. Curve-fit results ($\alpha_p = {\beta_p}^{0.65}$ and $R^2 = 0.78$) show a good correlation between computed values of α_p using wind profiles from the leaf-on and leaf-off stages of the Osage orange barrier with observed values of β_p using image analysis. During curve-fit tests, the empirical equation obtained by Guan et al. (2003), $\alpha_p = {\beta_p}^{0.4}$, was found to differ slightly from the empirical equation obtained in this study. An exponent of 0.65 rather than 0.4 was found to be a better fit for the Osage orange tree barrier. The difference could be attributed to the various types of measurements that were done: Guan et al. (2003) used a wind tunnel with highly controlled conditions, while this study conducted full-scale tests within a field setting. In addition, a real tree shelterbelt was used for this study compared to the artificial custom model used by Guan et al. (2003) and the artificial Scots pine Christmas tree used by Grant and Nickling (1998). As Grant and Nickling (1998) stated, the exponent for the empirical equation depends on the composition of leaves and the breadth and width ratio of the shelterbelt under consideration. This study showed that the methodology of Guan et al. (2003) can be applied in a field setting as long as field conditions are conducive for obtaining wind profiles (not too strong nor too calm and within 6-12 m s^{-1}, similar to the Hagen and Skidmore (1971) experiment). Photographs for β_p determination should be taken during calm winds (based on Loeffler (1992) and Kearney (1987) suggestions) to prevent excessive motion of leaves and branches that allow more gaps or less gaps in photos and potentially lead to inconsistent β_p readings.

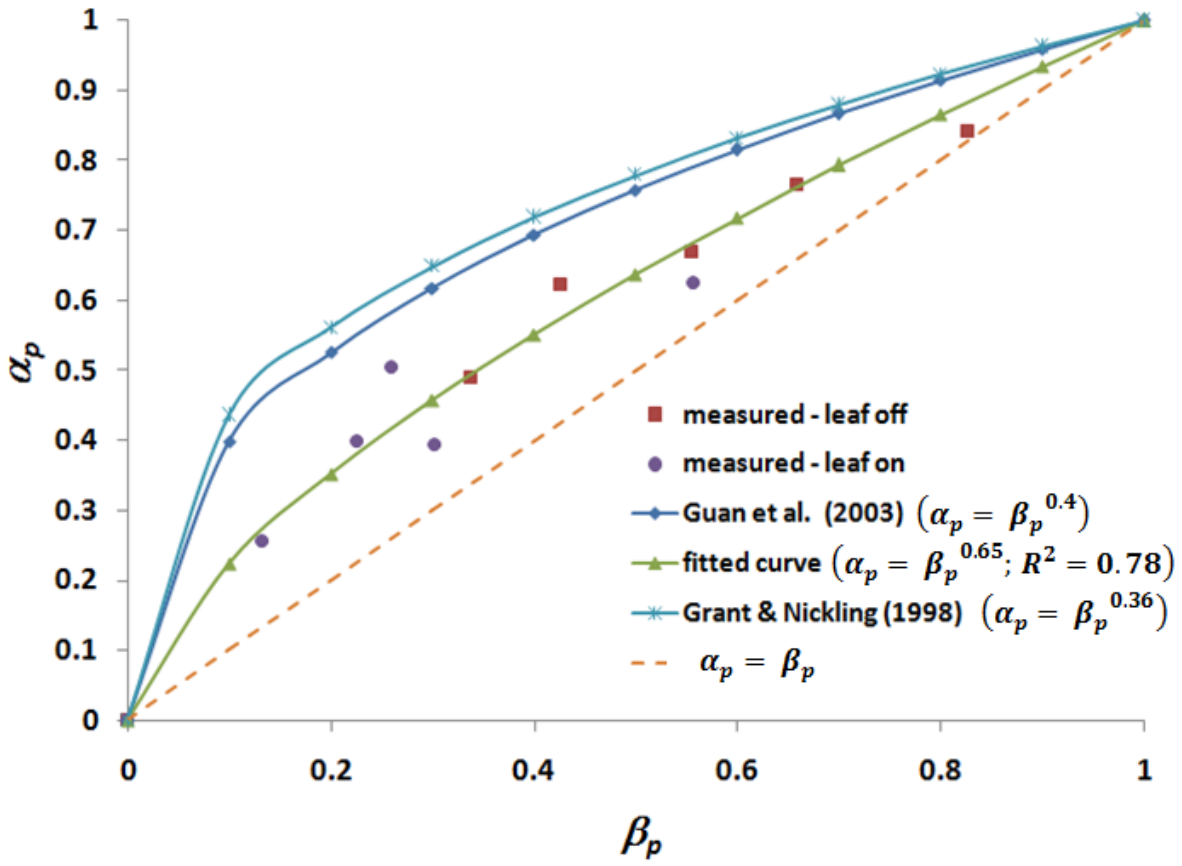

Figure 4.9. Relationship between measured aerodynamic (α_p) and optical (β_p) porosities of the Osage orange barrier.

The scatter of points in Figure 4.9 from measured values during the leaf-on and leaf-off stages could be a result of difficulties encountered during the field tests. This study was limited by availability of anemometers because no measurements were taken for wind speeds along the width of the shelterbelt section with vertical gradient measurements. During the experiment, only a single location (along the width or section of the barrier strip) was chosen and only various distances away from the barrier and vertical gradient wind speeds were collected and considered to obtain aerodynamic parameters. Even if multiple measurements are present along the width of the barrier with simultaneous vertical gradient measurements, acquisition of representative values for α_p is difficult because of intermittent changes in wind speeds upwind of the barrier,

especially during field experiments during leaf-off conditions, as evidenced by the windrose plot (Figure 4.5). In addition, the presence of holes and gaps within the barrier at locations of expected increased bleed wind speed (same observation as Guan et al, 2003) and the structure complexity of the Osage orange barrier during the leaf-on stage with the presence of leaves and tiny branches causes changes in wind speeds as they are oscillating. As such, the presence of dynamic movements of leaves and branches complicate the measurements of downwind profiles close to the barrier that are necessary to compute value of α_p.

4.3.3. Shelterbelt Drag Coefficient

A comparison of values of C_D (based on Hagen and Skidmore (1971) methodology) between leaf-on and leaf-off conditions of the Osage orange barrier is shown in Figure 4.10. Throughout field measurements, wind speeds varied from 4 m s^{-1} to approximately 7 m s^{-1}, similar to Hagen and Skidmore (1971) and Meroney (1968) tests. Drag coefficients were independent of wind speeds, especially those less than 6 to 8 m s^{-1}. Expected $C_D's$ based on Hagen and Skidmore (1971) for a given shelterbelt porosity were close to C_D values pertaining to specific β_p values of the Osage orange tree barrier. Despite marked differences between rigid shelterbelts and trees having continuously moving leaves and branches during field tests, C_D values obtained were similar over the range of wind speeds tested during experimentation.

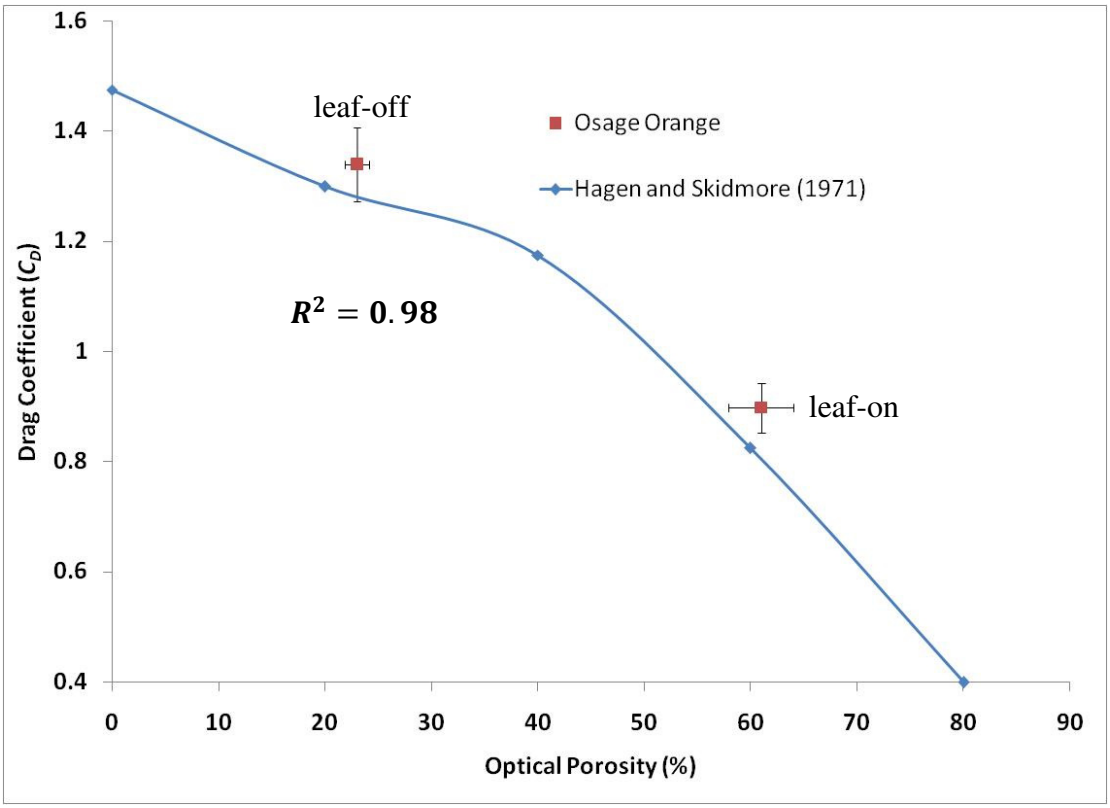

Figure 4.10. Plot of drag coefficient vs. optical porosity.

The trend of decreasing C_D with increasing shelterbelt porosity could be further explained by changes in wind momentum as it encounters the shelterbelt and flows continuously downwind of the barrier. Schwartz et al. (1995) detailed what happens behind various types of model shelterbelts, where they found some portions had recirculation phenomenon leeward of the barrier while others did not. This recirculation zone could cause large eddies immediately downwind of the shelterbelts, thereby greatly affecting wind behavior behind the shelterbelt. The presence of gaps or large holes within the shelterbelt cause jetting of air through the barrier which forms eddies behind the barriers. Upwind of the barrier, loss of air momentum is caused by the presence of vegetative elements (i.e., leaves, branches, trunk) during leaf-on condition of the barrier, consequently amplifying multiple transfers of momentum among elements within the shelterbelt (Grant and Nickling, 1998), especially at the crown portion of the Osage orange tree.

This momentum transfer creates a barrier resistance to airflow that causes drag coefficient values to increase. As the leaves fall off, porosity increases, resulting in a decrease in the drag coefficient.

4.4. Conclusions

Deciduous trees such as Osage orange are commonly used as shelterbelts in Kansas. Aerodynamic (α_p) and optical (β_p) porosities of this species were estimated using wind profiles and image analysis, respectively, and an empirical equation relating the two porosities was derived ($\alpha_p = {\beta_p}^{0.65}$; $R^2 = 0.78$). Vertical wind profiles were also used to estimate drag coefficients that determined how much resistance the barrier offered incoming airflow to protect agricultural lands downwind of the barrier during leaf-on and leaf-off stages of the tree. A good correlation between optical porosity and drag coefficient was also obtained ($R^2 = 0.98$). Aerodynamic parameters (porosities and drag coefficients) obtained in this study are essential for validating numerical simulations for further optimization of shelterbelt sheltering efficiency.

4.5. References

Bird, P.R., Bicknell, D., Bulman, P.A., Burke, S.J.A., Leys, J.F., Parker, J.N., van der Sommen, F.J., & Voller, P. 1992. The role of shelter in Australia for protecting soils, plants and livestock. *Agrofores. Sys.* 20: 59-86.

Bitog, J.P., Lee, I.B., Hwang, H.S., Shin, M.H., Hong, S.W., Seo, I.H., Mostafa, E., & Pang, Z. 2011. A Wind tunnel study on aerodynamic porosity and windbreak drag. *Forest Sci. Tech.* 7(1): 8-16.

Brandle, J.R., Hodges, L., & Zhou, X.H. 2004. Windbreaks in North American agricultural systems. *Agrofores. Sys.* 61: 65-78.

Bouvet, T., Loubet, B., Wilson, J.D., & Tuzet, A. 2007. Filtering of windborne particles by a natural windbreak. *Boundary Layer Meteorol.* 123: 481-509.

Burel, F. & Baudry, J. 1995. Social, aesthetic and ecological aspects of hedgerows in rural landscapes as a framework for greenways. *Landscape and Urban Planning* 33: 327-340.

Campi, P., Palumbo, A.D., & Mastrorilli, M. 2009. Effect of tree windbreak on microclimate and wheat productivity in a Mediterranean environment. *Eur. J. Agron.* 30: 220-227.

Cleugh, H.A. 1998. Effects of windbreaks on airflow, microclimates, and crop yields. *Agroforestry Sys.* 41: 55-84.

Cornelis, W.M. & Gabriels, D. 2005. Optimal windbreak design for wind-erosion control. *J. Arid Environ.* 61: 315-332.

Cullen, S. 2005. Trees and wind: A practical consideration of the drag equation velocity exponent for urban tree risk management. *J. Arboriculture* 31(3): 101-113.

Ffolliott, P. 1998. Multiple benefits of arid land agroforestry home gardens and riparian ecosystems. In *Farming the forest for specialty products*. Proceedings of the Conference on Enterprise Development Through Agroforestry, ed., Josiah, S. J., 41-46. St. Paul, MN: Center for Integrated Natural Resources and Agriculture Management, University of Minnesota.

Grala, R.K., Tyndall, J.C., & Mize, C.W. 2010. Impact of field windbreaks on visual appearance of agricultural lands. *Agroforest Sys.* 80: 411-422.

Grant, P.F. & Nickling, W.G. 1998. Direct field measurement of wind drag on vegetation for application to windbreak design and modeling. *Land Degrad. Develop.* 9: 57-66.

Gregory, N.G. 1995. The role of shelterbelts in protecting livestock: A review. *New Zealand J. Agri. Res.* 38: 423-450.

Guan, D., Zhang, Y., & Zhu, T. 2003. A wind-tunnel study of windbreak drag. *Agri. Forest Meteorol.* 118: 75-84.

Hagen, L. & Skidmore, E. 1971. Windbreak drag as influenced by porosity. *Trans. ASAE* 14: 464-465.

Heisler, G. & DeWalle, D. 1988. Effects of windbreak structure on wind flow. *Agri. Ecosys. Environ.* 22-23: 41-69.

Hyams, D.G. 2013. Curve expert 1.4 software. www.curveexpert.net

Kenney, W.A. 1987. A method for estimating windbreak porosity using digitized photographic silhouettes. *Agri. Forest Meteorol.* 39: 91-94.

Koh, I., Park, C.R., Kang, W. & Lee, D. 2014. Seasonal effectiveness of a Korean traditional deciduous windbreak in reducing wind speed. *J. Ecol. Environ.* 37(2): 91-97.

Koizumi, A., Motoyama, J., Sawata, K., Sasaki, Y., & Hirai, T. 2010. Evaluation of drag coefficients of poplar-tree crowns by a field test method. *J. Wood Sci.* 56: 189-193.

Kort, J. 1988. Benefits of windbreaks to field and forage crops. *Agri. Ecosys. Environ.* 22-23: 165-191.

Kozmar, H., Procino, L., Borsani, A., & Bartoli, G. 2012. Sheltering efficiency of wind barriers on bridges. *J. Wind Eng. Ind. Aerodyn.* 107-108: 274-284.

Lee, K.H., Ehsani, R., & Castle, W.S. 2010. A laser scanning system for estimating wind velocity reduction through tree windbreaks. *Comp. Elect. Agri.* 73: 1-6.

Loeffler, A.E., Gordon, A.M., & Gillespie, T.J. 1992. Optical porosity and windspeed reduction by coniferous windbreaks in Southern Ontario. *Agro. Sys.* 17(2): 119-133.

Mader, T.L., Dahlquist, J.M., Hahn, G.L., & Gaughan, J.B. 1999. Shade and wind barrier effects on summertime feedlot cattle performance. *J. Anim. Sci.* 77(8): 2065-2072.

Meroney, R.N. 1968. Characteristics of wind and turbulence in and above model forests. *J. Appl. Meteor.* 7: 780-788.

Raine, J.K., & Stevenson, D.C. 1977. Wind protection by model fences in a simulated atmospheric boundary layer. *J. Ind. Aerodyn.* 2(2): 159-180.

Schwartz, R.C., Fryrear, D.W., Harris, B.L., Bilbro, J.D., & Juo, A.S.R. 1995. Mean flow and shear stress distributions as influenced by vegetative windbreak structure. *Agri. Forest. Meteorol.* 75(1-3): 1-22.

Sellier, D., Brunet, Y., & Faurcaud, T. 2008. A numerical model of tree aerodynamic response to a turbulent flow. *Forestry* 81(3): 279-297.

Steffens, J.T., Wang, Y.J., & Zhang, K.M. 2012. Exploration of effects of a vegetation barrier on particle size distributions in a near-road environment. *Atmos. Environ.* 50: 120-128.

Stredova, H., Podhrazska, J., Litschmann, T., Streda, T., & Roznovsky, J. 2012. Aerodynamic parameters of windbreak based on its optical porosity. *Contributions to Geophys. Geodesy.* 42(3): 213-226.

Stunder, B.J.B. & Arya, S.P.S. 1988. Windbreak effectiveness for storage pile fugitive dust control: A wind tunnel study. *J. Air Pollut. Control. Assoc.* 38: 135-143.

Sudhishri, S., Dass, A., & Lenka, N.K. 2008. Efficacy of vegetative barriers for rehabilitation of degraded hill slopes in eastern India. *Soil Till. Res.* 99(1): 98-107.

Sudmeyer, R.A., Crawford, M.C., Meinke, H., Poulton, P.L., & Robertson, M.J. 2002. Effect of artificial wind shelters on the growth and yield of rainfed crops. *Aus. J. Exp. Agric.* 42: 841-858.

Sun, D., & Dickinson, G.R. 1997. Early growth of six native Australian tree species in windbreaks and their effect on potato growth in tropical northern Australia. *For. Ecol. Manage.* 95: 21-34.

Vigiak, O., Sterk, G., Warren, A., & Hagen, L.J. 2003. Spatial modeling of wind speed around windbreaks. *Catena* 52: 273-288.

Wang, H., & Takle, E.S. 1996. On three-dimensionality of shelterbelt structure and its influences on shelter effects. *Boundary Layer Meteorol.* 79: 83-105.

Wilson, J.D. 1987. On the choice of a windbreak porosity profile. *Boundary Layer Meteorol.* 38: 37-49.

Woodruff, N.P., Fryrear, D.W., & Lyles, L. 1963. Engineering similitude and momentum transfer principles applied to shelterbelt studies. *Trans. ASAE.* 6(1): 41-47.

Zhu, J-J. 2008. Wind shelterbelts. In: Encyclopedia of Ecology. pp. 3803-3812.

CHAPTER 5 - Dust Reduction Efficiency of a Single Row of Vegetative Barrier (*Maclura pomifera*)

5.1. Introduction

Agricultural lands that are exposed to dry, windy conditions are susceptible to wind erosion. Vegetative barriers (also called windbreaks or shelterbelts) involving a row or multiple rows of trees are typically used to prevent or minimize wind erosion.

Vegetative barriers are beneficial aesthetically (Grala et al., 2010) and for reducing wind speed that causes changes in the microclimate of soils (Cleugh, 1998), thereby affecting productivity and soil fertility (Kort, 1998; Bird et al., 1992, Sudmeyer et al., 2002), and livestock health and recreation (Ffolliott, 1998; Mader et al., 1999). Vegetative barriers can also mitigate odor (Tyndall and Colletti, 2007), sounds (Harris and Cohn, 1985; Ozer et al., 2008), spray drifts (Lazzaro et al., 2008; Vischetti et al., 2008), and air pollutant emissions (Kulshreshtha et al., 2009; Brantley et al., 2014).

Previous studies have assessed airflow (Hagen and Skidmore, 1971; Fryrear and Skidmore, 1985; Gregory, 1995; Brandle et al., 2004; De Zoysa, 2008; Guo, 2008; El-Flah, 2009) and particulate matter (PM) mitigation (Grantz et al., 1998; Dierickx, 2003; Burley et al., 2011; Lin and Khlystov, 2012) with vegetative barriers. A good sampling methodology by Tiwary et al. (2008) evaluated the effectiveness of a Hawthorn hedge for collecting ambient PM. Two gravimetric PM_{10} (PM with equivalent aerodynamic diameter of 10 μm or less) samplers were placed at a height of approximately 70% of the total tree height, at the crown of the tree (consists of foliage and branches extending from the trunk), for upwind and downwind locations. Their study quantified filtration collection efficiency ($CE_{Filtration}$) of the Hawthorn tree, and they found 30-38 % of ambient PM_{10}.

Complexity of flow within the canopy is important (Raupach et al., 2001). Complex flow through canopies results from great turbulence as vegetative elements hinder the incoming flow and initiate tortuosity and effective mixing of PM (Tiwary et al., 2008). Details of flow through canopies for various species differ because elements that comprise them differ. Most vegetative barrier species are not documented with respect to their aerodynamic characteristics and resulting ability to reduce wind and collect or mitigate PM emissions within their surroundings.

One of the oldest species of trees used as vegetative barriers against wind erosion in Kansas are deciduous trees known as Osage orange (*Maclura pomifera*). Known for their relative strength and durability, Osage orange became the raw materials for weapons (bows for American Indians who inhabited the Kansas region in the 1800s), wagon wheels, and fence posts (Smith and Perino, 1981). Although these trees are commonly used as barriers, their effectiveness in terms of PM mitigation has not been quantified.

The objective of this study was to quantify the effects of the presence of Osage orange trees as vegetative barriers for wind erosion control. Specific objectives were to:

1) determine effects of the presence of Osage orange barrier on particle size distribution (PSD); and
2) determine particle concentration reduction efficiency ($C_{Reduction}$) due to the Osage orange barrier.

5.2. Materials and Methods

5.2.1. Site Description

This research was conducted from August 2014 to September 2014 at a farm near Riley, Kansas (39°18'49.1"N 96°54'29.2"W). The experimental fields, located at an elevation of 580 m, had a combined dimensions of 300 m in length and 200 m in width where the vegetative barrier

runs from east to west that separates into two distinct fields for sampling - the upwind and downwind fields. The fields were planted with a winter wheat, corn, and sorghum rotation. No-till management was employed on the crop rotation to maintain soil productivity and decrease soil vulnerability to wind erosion. The vegetative barrier row used for the experiment was located between two fields referred to as the north side and south side (Figure 5.1). The vegetative barrier strip measured 2.5 m in width with an average height (H) of H = 8.5 ± 0.6 m. During the dust tests, both sides of the field had wheat stubble cut to a height of approximately 0.1 m.

Prevailing wind direction for the field site was south-southwest for the summer and north-northwest for the winter. Data were collected with direct south wind (summer test) when the Osage orange barrier retained foliage.

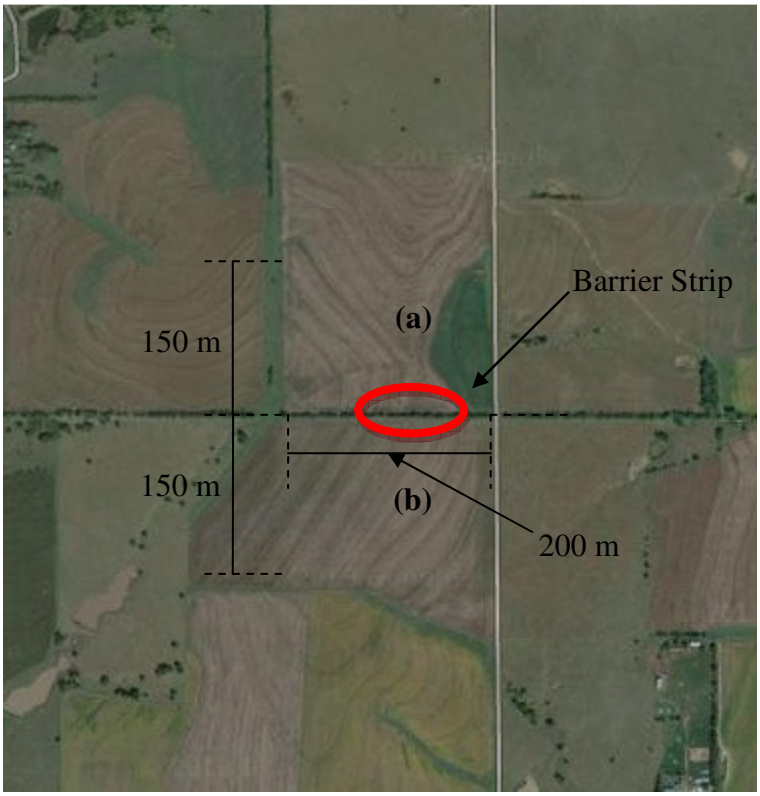

Figure 5.1. Aerial view of the field site (via Google Maps): (a) north side and (b) south side.

5.2.2. Dust Generation

A fluidized bed dust generator was developed to disperse dust particles into the air upwind of the barrier. The generator consists of a screw-type feeder, centrifugal pump, electric generator, and dust outlet. The feeder has control settings to generate the desired amount of dust. The centrifugal pump, powered by the electric generator, forces air through a bed of dust particles and moves the generated dust to the dust outlet (Prenni et al., 2000). The dust particles were obtained by grinding soil (25% clay, 9% sand, and 66% silt) and drying the ground soil in the oven for at least 24 h at 60 °C prior to grinding.

To ensure the efficiency of the barrier, a dust line source was needed. Two designs were tested in combination with the fluidized bed dust generator. The first involved mounting the dust generator with one dust outlet on a moving truck. Preliminary tests were conducted in which the truck that was driven back and forth along a 10-m distance to create a line-source of dust generation. The truck was driven at a distance equivalent to 5 times the average tree height (H = 8.5 m). Preliminary results indicated that an insufficient amount of dust sample was collected even upwind of the barrier (1H away from barrier upwind) possibly due to non-uniformity in the dust plume. Difficulties in controlling the speed of the truck with the mounted dust generator were also encountered, and the location available for sampling had ridges that caused an up and down motion of the truck, promoting non-uniformity in the plume. Feeding soil into the dust generator required full stoppage of the truck, consequently promoting bias for regions along the designated line of dust source where concentration of particles may have increased. In addition, use of vehicle posed a challenge because of instantaneous changes in wind direction at the site during sampling. Therefore, this approach was abandoned.

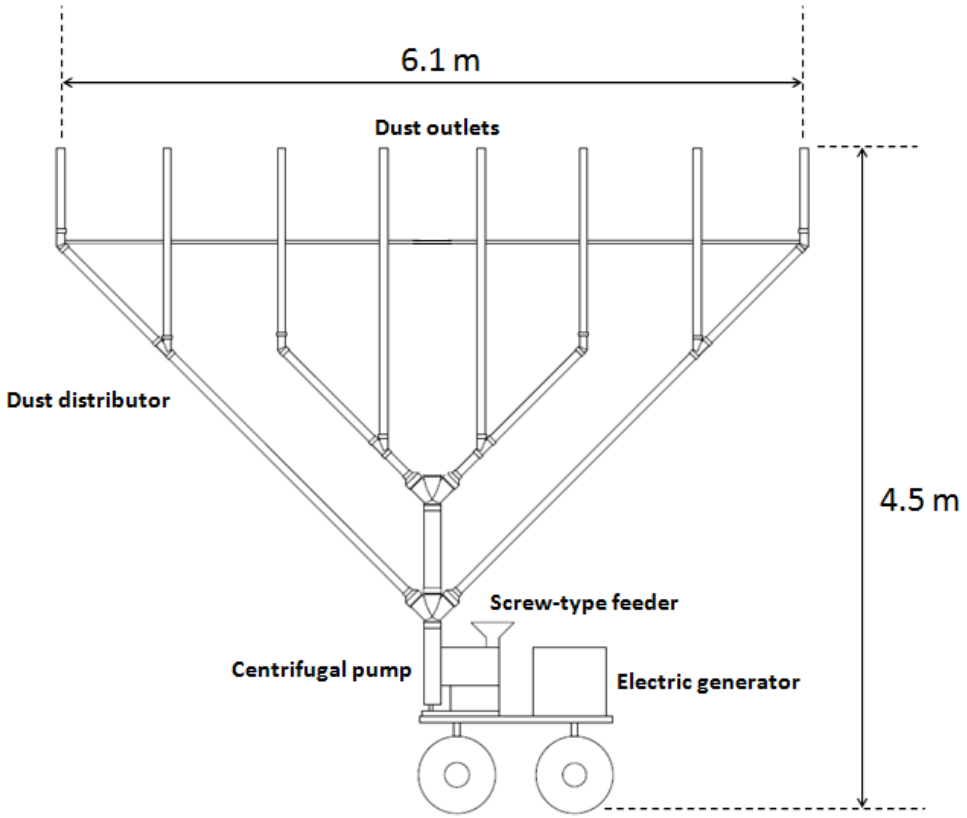

Figure 5.2. Dust generator showing major components.

In the second design, a dust distributor (Figure 5.2) was fabricated and connected to the fluidized bed dust generator to provide multiple point sources. The distributor was designed to have approximately equal pressure drop from pipes and for all emission points producing equal emission and concentrations from each emission point. Computations of velocities of dust within the dust distributor were based on airflow rate measurements made with a flow meter for the inlet. Velocities were obtained with the following equation:

$$Q_{air} = u\left(\pi \frac{d^2}{4}\right) \tag{5.1}$$

where Q_{air} is the air volumetric flow rate ($m^3\ s^{-1}$), u is air velocity ($m\ s^{-1}$), and d_{pipe} is pipe diameter (m). Sudden but minor wind direction shifts often occurred during the course of the experimental runs and, at such instances, the distributor ensured that the source of dust remained

aligned with the upwind and downwind samplers. Preliminary tests with this dust distributor were successful in generating measurable amount of dust upwind and downwind of the tree barrier and was then used for the remainder of the test.

5.2.3. Field Sampling

The field was equipped with a weather station (Model Vantage Pro2, Davis Instruments) that had a solar panel and an integrated sensor suite (combination of temperature and humidity sensors, anemometer, and rain gauge). The weather station was operated by battery and solar power and was connected to a wireless receiver that could be operated up to 300 m away from the sensor for data collection.

Wind profiles for Osage orange barriers were obtained prior to PM sampling, as discussed in Chapter 4. Sampling layout is shown in Figure 5.3. Towers were positioned close to the barrier approximately 1H away on both sides. This distance was chosen to prevent effects of recirculation regions before and after the row of Osage orange barrier that could induce particle re-entrainment and affect measured particle concentrations (Huang et al., 2005). Heights (1.5, 3, 4.5, and 6 m above ground, as shown in Figure 5.4) of anemometer and PM samplers were based on the methodology used by Tiwary et al. (2008) and Sellier et al. (2008). PM sampler inlets were placed using metal brackets along the tower at the same heights as the Sierra Misco 1005 DC cup anemometers (NovaLynx Corporation, CA) (Figure 5.3) on each tower at the north and south sides.

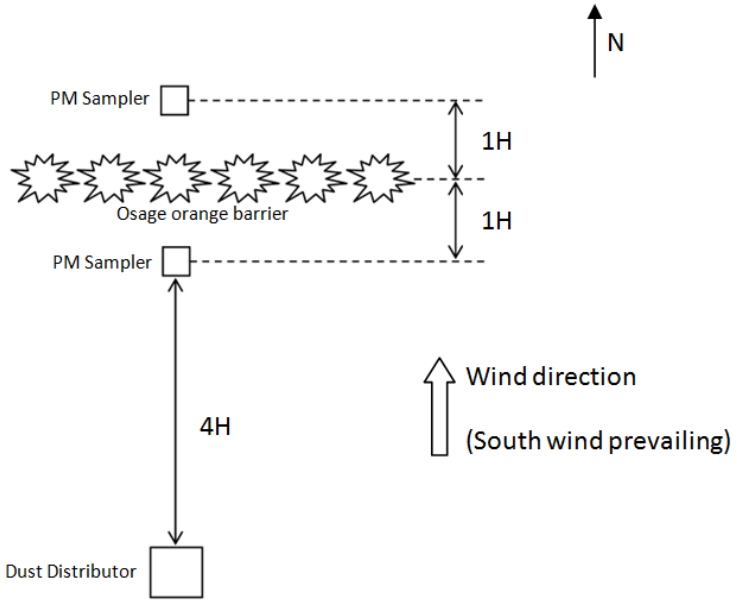

Figure 5.3. Field experiment layout.

Dust was collected using low volume samplers (Model Airmetrics Minivol^{TM} TAS, Oregon) equipped with total suspended particles (TSP) inlets. Due to restrictions from the amount of dust generated as affected by the maximum feeding rate of the feeder and amount of sample the laser diffraction analysis requires, tests were set at 1.5-h runs. This length of time was long enough to collect sufficient amount of dust for PSD analysis given the maximum feed rate of ground soil that was possible for the dust generator. The sampling technique followed Tiwary et al. (2008), except with additional samplers placed at various heights 1H away from the tree barrier with the topmost level of sampler representative of the majority of the crown portion of the Osage orange barrier.

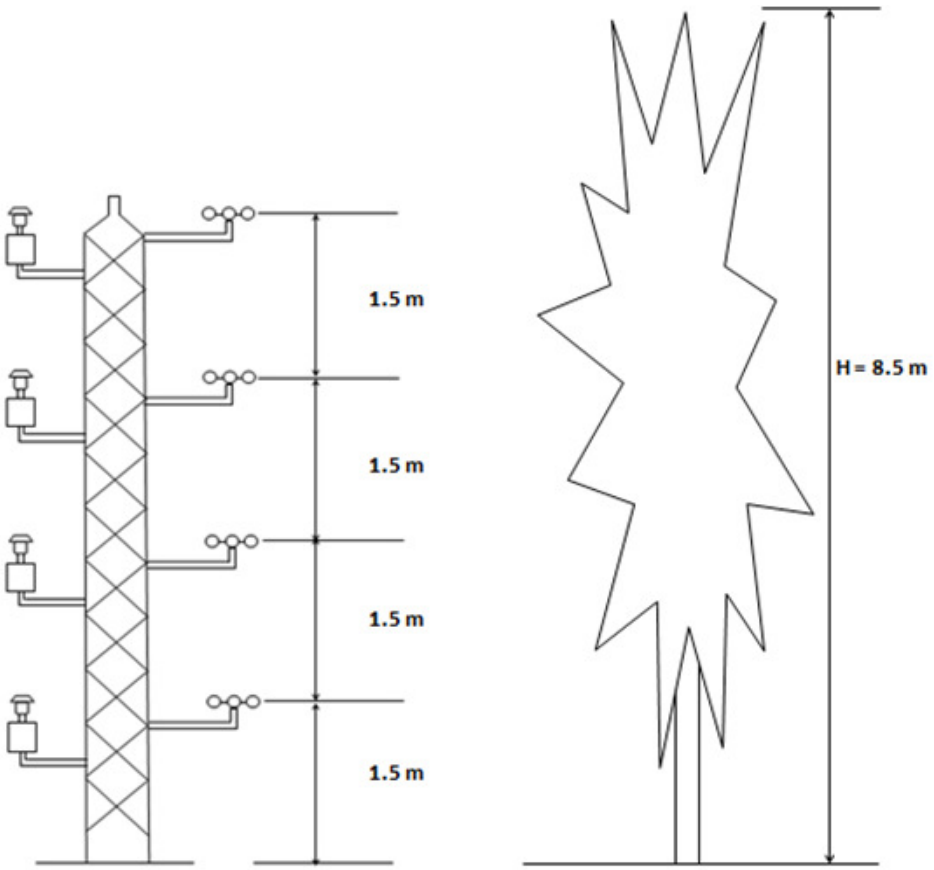

Figure 5.4. Schematic diagram of PM samplers and cup anemometers.

Polytetrafluoroethylene (PTFE) filters used for sampling were conditioned for 24 h at 25 °C and 40% RH in a chamber prior to weighing before and after sampling for mass determination of dust particles (Cavanagh et al., 2009; Gonzales et al., 2012). Mass of dust collected was the difference of mass of conditioned filter before and after sampling, while concentrations were derived by dividing the mass of dust collected by the total volume of air sampled and then recorded by the PM sampler.

5.2.4. Particle Size Distribution (PSD) Analysis

Sampled particles were characterized using a Beckman Coulter LS 13 320 laser diffraction instrument. Dust collected in the filters was washed using isopropyl alcohol and

individually placed in plastic 50 mL centrifuge tubes. The mixture was then centrifuged using an Eppendorf centrifuge (Model 5810 R) at 4000 RPM for 5 min. A vortex mixer was also used to prevent formation of aggregates. The laser diffraction instrument conducted sonication during measurements for PSD of the soil sample (Gonzales et al., 2012).

Ground soil from the Kansas State University North Agronomy farm was analyzed using wet analysis (LS 13320 Beckman Coulter laser diffraction instrument). PSD of the original dust sample is shown in Figure 5.5. Large particles dominated as evidenced by the skewness of the graph towards the larger sizes. The geometric mean diameter (GMD) of the original sample was 79.2 μm with a geometric standard deviation (GSD) of 4.3.

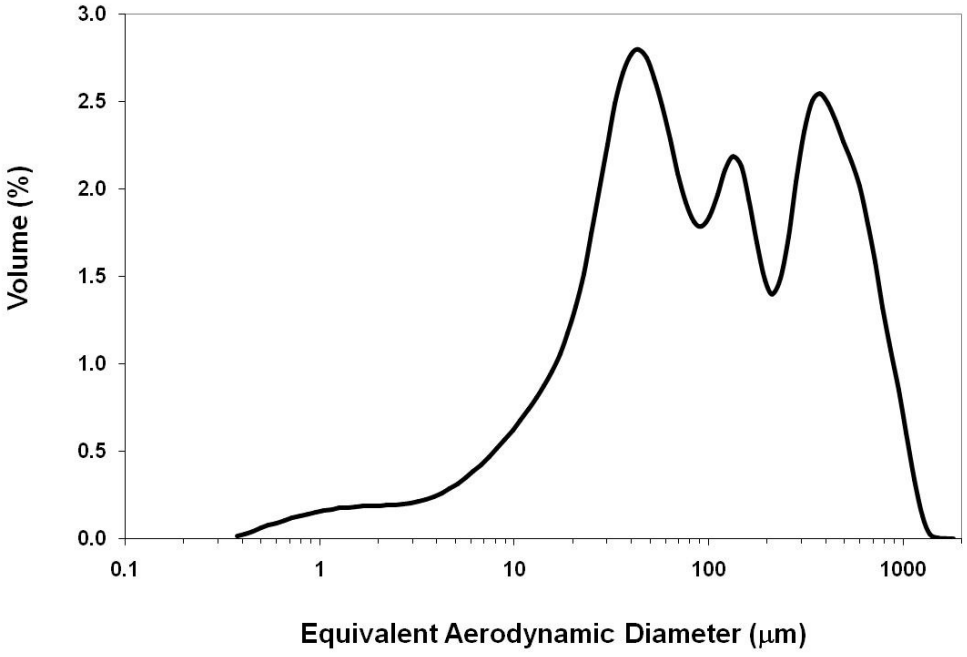

Figure 5.5. Particle size distribution of the dust sample fed through the dust generator.

To ensure uniformity and sample quality, the same person always ground the soil. The feed to the grinder was executed slowly to better generate small particles. Prior to field work, aggregated soils formed, even after soils passed through the grinder, if the soils did not have

enough time for drying (typical drying at 60 °C for two days), especially if soils were taken from a relatively moist or damp region of the farm in the case of significant precipitation at the time of soil sampling.

The GMD and GSD were obtained using laser diffraction data, and PM_{10} and $PM_{2.5}$ concentrations were estimated using the particle fraction method (Gonzales et al., 2012). Aerodynamic diameters were obtained using particle density of 1.4 ± 0.1 g cm^{-3}, identical to Gonzales et al. (2012). Based on values of dust concentrations upwind and downwind the Osage orange barrier, the equation for particle concentration reduction was parallel to the collection efficiency of filtration from previous studies (Tiwary et al., 2005; Tiwary et el., 2008), computed using the following equation:

$$C_{Reduction} = \frac{C_{up} - C_{down}}{C_{up}} \quad (5.2)$$

where C_{up} and C_{down} are the dust concentrations upwind and downwind of the Osage orange barrier.

5.2.5. Data Analysis

Mean values of mass concentrations were obtained from 12 filter samples each for upwind and downwind positions and were used for analysis representing three replicates. The filter samples with dust were used for laser diffraction analysis, and values of velocity reduction and collection efficiency were compared. Analysis of variance (ANOVA) and paired t-test were done using Microsoft Excel (Microsoft Corp., Redmond, WA) to determine differences in mass concentrations, wind speed reduction, GMD, and % $C_{Reduction}$. A 5% level of significance was used for all cases. CurveExpert 1.4 (Hyams, 2013) was used to plot best-fit curves that were compared to the curve fitting tool in Microsoft Excel (Microsoft Corp., Redmond, WA.).

5.3. Results and Discussion

5.3.1. Particle Characterization

A summary of the PSD of sampled dust at various heights for each of the two locations (upwind and downwind of the Osage orange barrier) is shown in Figure 5.6. A majority of large particles were dominant at the lower level (Level 1, 1.5 m above the ground), while most of the small particles were dominant at the highest level (Level 4, 6 m above the ground) for both locations.

Figure 5.7 shows the comparison of PSD at each level along the tree height between upwind and downwind locations. In general, reduction of large particles occurred more efficiently, as indicated by the shift of the size distribution plot towards the left (towards small sizes). This trend was more pronounced for the lower portions of the tree (Level 1 and Level 2), as evidenced by the sharp decrease in sizes where all plots were skewed towards the small particles. However, although large particles were also collected in the upper levels (Level 3 and Level 4), particle size changes were not as pronounced as the lower levels.

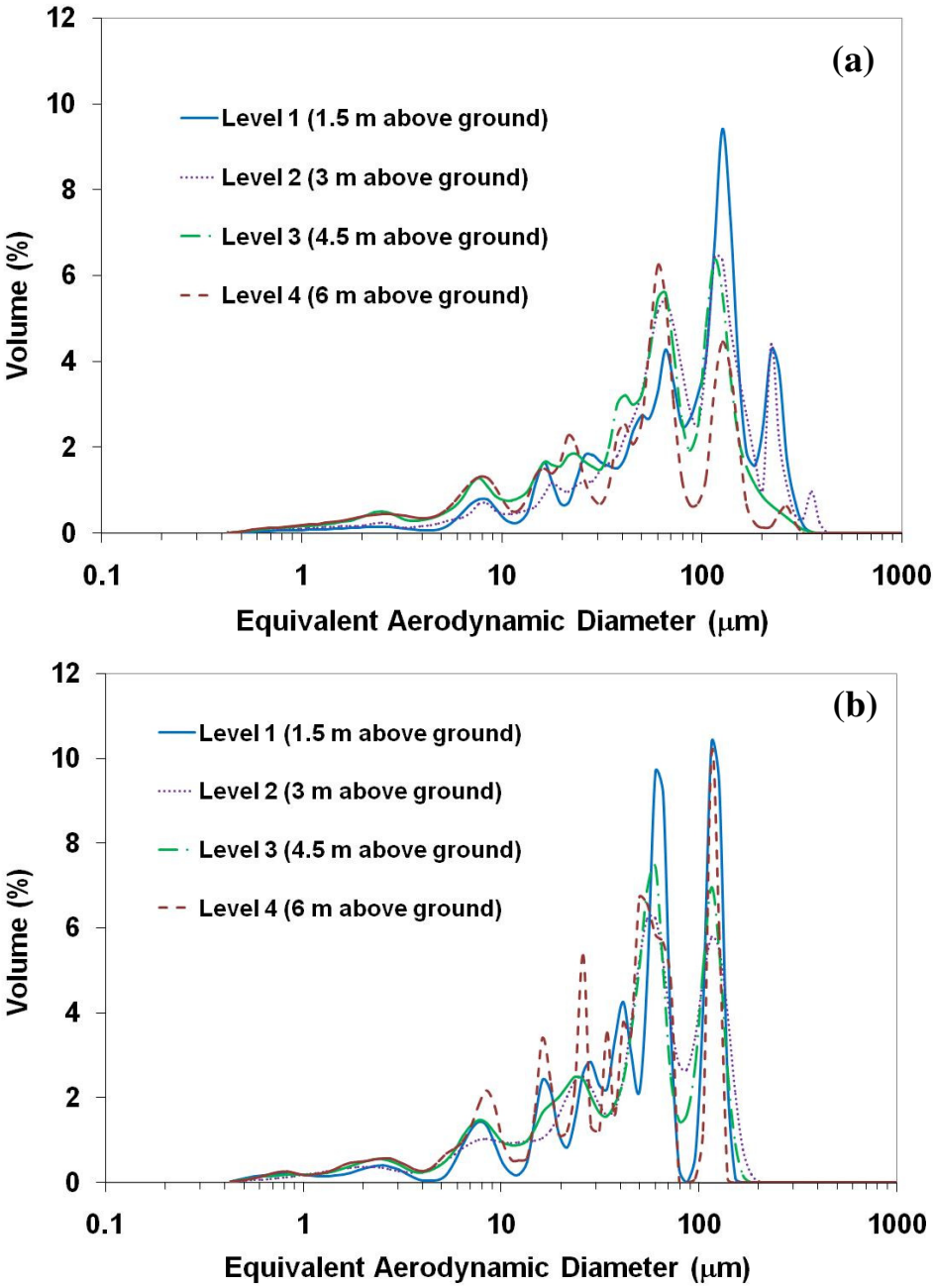

Figure 5.6. Comparison of collected dust particle size distribution between various heights for each location: (a) upwind and (b) downwind.

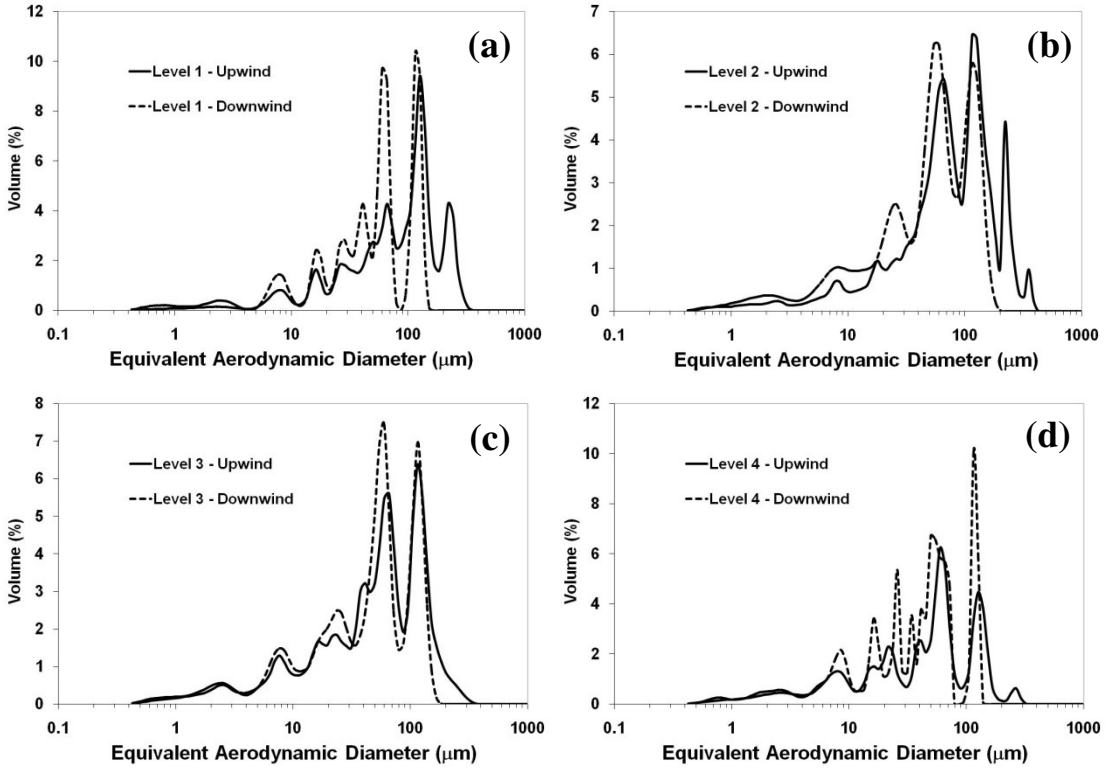

Figure 5.7. Particle size distribution comparison at specific heights: (a) Level 1 = 1.5 m, (b) Level 2 = 3.0 m, (c) Level 3 = 4.5 m, and (d) Level 4 = 6.0 m above the ground.

A comparison of the GMD for the various heights is summarized in Table 5.1. GMD values for the uppermost levels (Level 3 and 4) at the windward portion of the barrier were significantly different ($p < 0.05$) from GMD values of the three other heights. This was expected because the dust was distributed into the air approximately 4.5 m above the ground (in line with the PM sampler of Level 3 for comparison, as shown in Figure 5.8) and the samplers were located 4 H away from the source (Figures 5.3 and 5.4), meaning that large particles were not expected to dominate the topmost sampler level (Level 4) because the particles were expected to have settled as explained by Lundgren et al. (1984). However, no significant differences ($p < 0.05$) were observed between GMD values between various heights for the downwind portion of

the barrier, indicating that most large particles that dominated the lower three levels compared to the topmost level upwind of the barrier were collected by the Osage orange barrier.

Table 5.1. Mean GMD, GSD and standard error of the mean (SEM) at various heights upwind and downwind of the Osage orange barrier (three replicates per run).

Height Above Ground (m)	GMD ± SEM (μm)		GSD ± SEM	
	Upwind	Downwind	Upwind	Downwind
1.5	65.6 ± 7.8[a]	44.6 ± 0.5[a]	3.2 ± 0.7[a]	3.6 ± 0.1[a]
3.0	61.4 ± 10.3[a]	40.3 ± 4.4[a]	3.5 ± 0.2[a]	3.6 ± 0.1[a]
4.5	49.3 ± 12.9[b]	38.3 ± 0.9[a]	4.0 ± 0.2[a]	3.9 ± 0.1[a]
6.0	34.4 ± 5.9[b]	34.4 ± 4.0[a]	4.3 ± 0.2[a]	3.7 ± 0.3[a]

[*]**different letters within a column indicate significant difference ($p < 0.05$)**

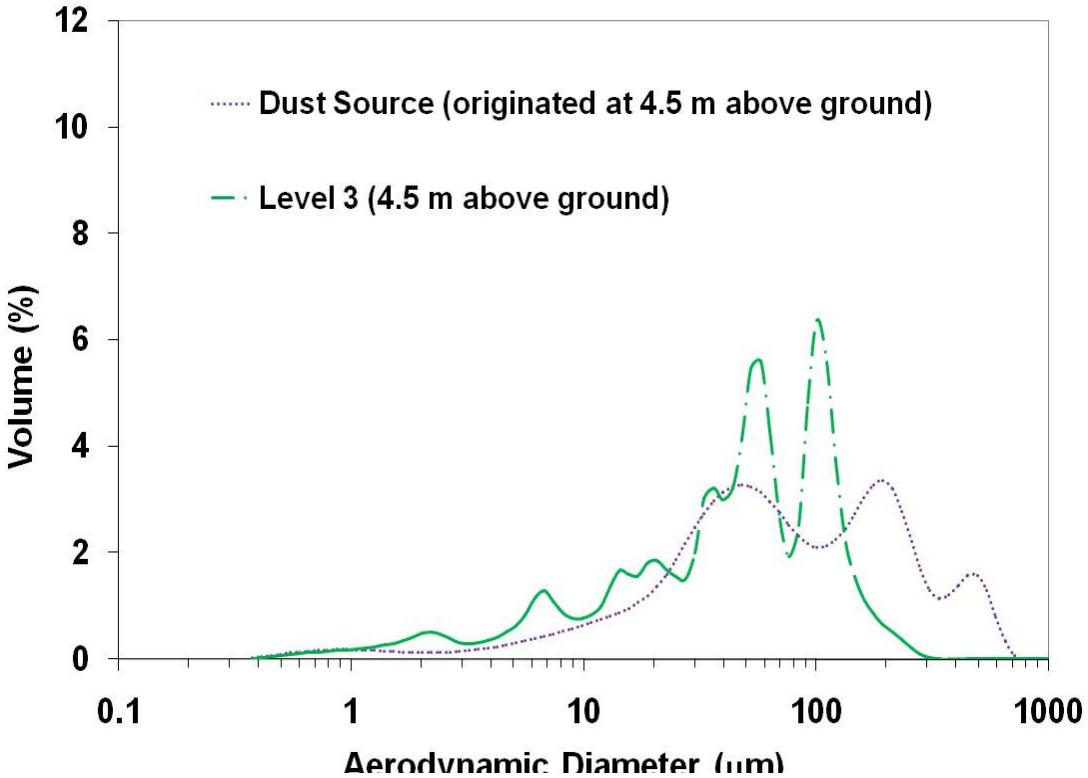

Figure 5.8. PSD of dust source and collected dust 4H apart upwind of the barrier.

The relationships between wind speed and GMD at different height levels are shown in Figure 5.9. From a previous study by Gonzales et al. (2012), the GMD was expected to increase or decrease depending on wind speed. For this study, similar trends for all heights were observed in which a decrease in wind-induced resuspension occurred at lower wind speeds, as explained by Jones et al. (2010), consequently leading to a decreased GMD (Lundgren et al., 1984) because large particles settle faster than small particles, even after a short distance. For greater wind speeds, a higher probability existed that large particles were suspended by wind at greater distances, resulting in higher measured GMD.

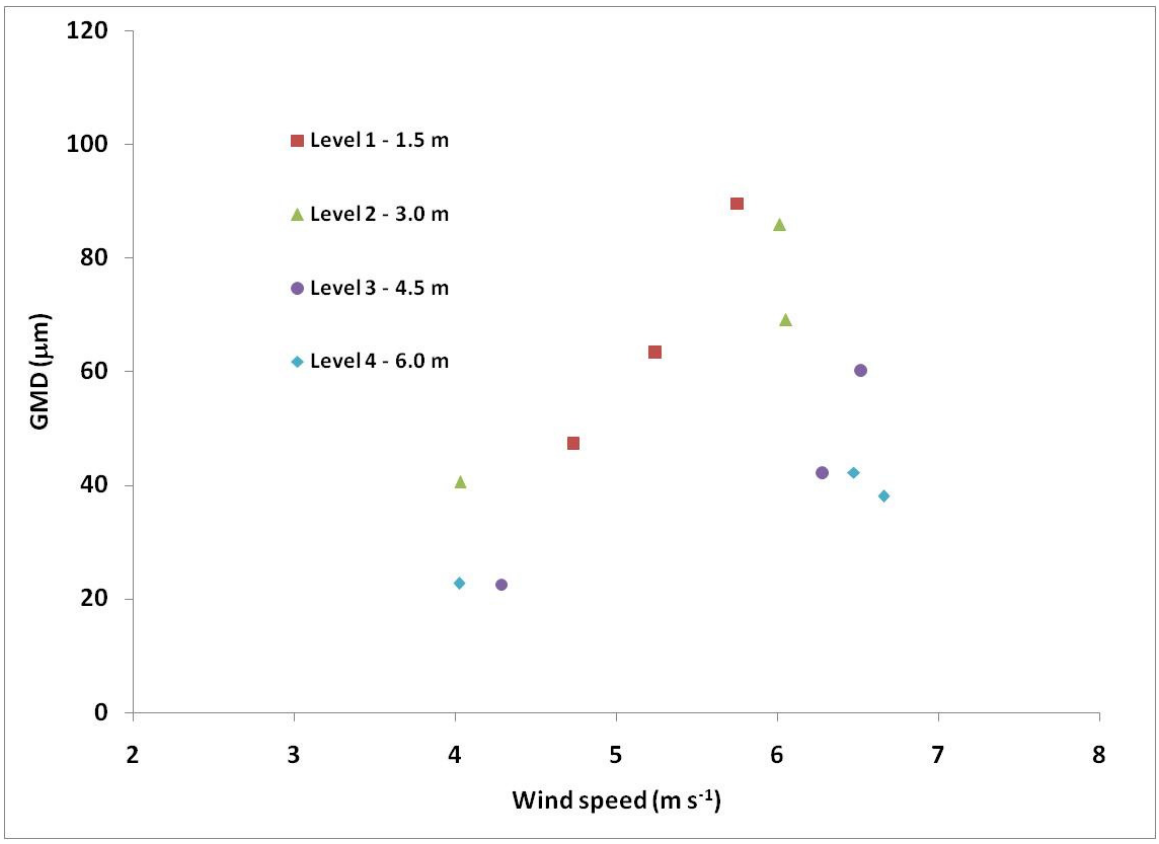

Figure 5.9. GMD and wind speed relationship at different heights.

5.3.2. Measurement of Dust Concentrations and Concentration Reduction

Measured concentrations summarized in Table 5.2 are not representative of the local ambient dust concentration, but they were used to compute collection efficiency of the Osage orange barrier. In addition, a correction derived from PM concentration values with and without barriers downwind was introduced to compute the dust concentration reduction efficiency of the Osage orange barrier, similar to the approach by Tiwary et al. (2008), to ensure that decreases in concentrations were due to the presence of the barrier. Mass concentrations of $PM_{2.5}$ and PM_{10} were also taken downwind of the source without the barrier and the corresponding value decreases are the correction factors used for the concentration reduction efficiency computations. Original dust generated from the ground soil was tested for $PM_{2.5}$ and PM_{10} compositions and found to have 1.9% and 5.8%, respectively.

Table 5.2. Mean mass concentrations and SEM of PM2.5, PM10, and TSP upwind and downwind of the barrier.

Height Above Ground (m)	Mean Mass Concentrations (μg m^{-3})					
	$PM_{2.5}$		PM_{10}		TSP	
	Upwind	Downwind	Upwind	Downwind	Upwind	Downwind
1.5	145 ± 25^{Ac}	123 ± 14^{Ac}	483 ± 84^{Ad}	374 ± 36^{Ad}	10815 ± 2260^{Ae}	8017 ± 368^{Ae}
3	226 ± 31^{Ac}	146 ± 27^{Ac}	779 ± 74^{Bd}	479 ± 65^{Ad}	14042 ± 2358^{Ae}	8952 ± 302^{Ae}
4.5	288 ± 54^{Ac}	131 ± 23^{Ac}	825 ± 200^{Bd}	460 ± 78^{Ad}	16331 ± 3076^{Ae}	6056 ± 693^{Ae}
6	136 ± 47^{Bc}	102 ± 37^{Ac}	516 ± 158^{Ad}	360 ± 127^{Ad}	10417 ± 2500^{Ae}	7523 ± 698^{Ae}
Overall	199 ± 39	126 ± 25	651 ± 129	418 ± 77	12901 ± 2549	7637 ± 515

***different letters indicate significant difference from each other (uppercase letter between rows and lowercase letter between columns)**

From the values in Table 5.2, the highest reduction of $PM_{2.5}$ and PM_{10} which corresponded to highest decrease in TSP occurred mainly on Level 3 (4.5 m) above the ground, differing significantly ($p < 0.02$) from $C_{Reduction}$ of the other levels. Lower values for the two lower levels (1.5 m and 3 m above ground) could be due to the fact that during sampling, the tested vegetative barrier (limited by field availability at the time of sampling) was full of gaps throughout the lower portions of the tree barrier, as shown in Figure 5.10, potentially due to intermittent changes in wind direction during sampling that caused some of the dust source to

drift away from the line of samplers. The highest value of $C_{Reduction}$ occurred at Level 3, which is the portion of the tree crown in which a significant amount of vegetation elements were present to filter out the dust particles. However, Level 4 was also part of the tree crown and did not show the same higher collection efficiency, possibly due to the level of dust source which was at 4.5 m (Figure 5.8) and insufficient resuspension of dust by the wind during tests that could have lifted dust particles to greater heights.

Figure 5.10. View of vegetative barrier tested for particle collection experiment.

Velocity reductions measured using cup anemometer data that represented identical heights as PM samplers at the Osage orange barrier compared to computed concentration reduction efficiencies of $PM_{2.5}$ and PM_{10} are shown in Table 5.3. As shown in the table, the greater the reduction of wind speed due to the presence of the Osage orange barrier, the greater the probability of the barrier to collect dust particles. However, Level 4 (6 m) did not exhibit this trend although that region was the canopy crown region, possibly due to insufficient resuspension of dust that originated from 4.5 m above the ground (Fig. 5.2). Although the values from Table 5.2 were not representative of the ambient concentration of dust within the

agricultural land tested, the overall dust reduction efficiency of the Osage orange was comparable to the performance of a Hawthorn hedge tested by Tiwary et al. (2008) where the range of collection efficiencies were 30 to 38 %.

Table 5.3. Comparison of speed reduction with PM particle concentration reduction.

Height Above Ground (m)	Speed Reduction (%)	$C_{Reduction}$ (%)		
		$PM_{2.5}$	PM_{10}	TSP
1.5	20.6^{Ac}	15.4^{Ac}	22.6^{Ac}	25.9^{Ac}
3	30.7^{Ac}	35.8^{Ac}	38.5^{Ac}	36.2^{Ac}
4.5	37.8^{Ac}	54.4^{Bc}	65.4^{Bc}	62.9^{Bc}
6	54.6^{Bd}	24.9^{Ac}	30.2^{Ac}	27.8^{Ac}
Overall	35.9	32.6	39.1	38.2

***different letters indicate significant difference from each other (uppercase letter between rows and lowercase letter between columns)**

5.4. Conclusions

A dust generator was fabricated and connected to a distributor to simulate a line source of dust to assess collection efficiencies of the Osage orange barrier. Ground soil (measured with GMD of 79.2 μm and GSD of 3.8) used as a dust source was composed of 1.9% $PM_{2.5}$ and 5.8% PM_{10}. Results showed that a single row of Osage orange captured 15 to 54% of $PM_{2.5}$ and 23 to 65% of PM_{10} from the simulated dust. Reduction of dust particles occurred better at the crown portion of the tree. The overall reduction efficiency of the Osage orange barrier (33 to 39%) was comparable to that of a published data for Hawthorn hedge (30 to 38%). Also, PSD analysis using the laser diffraction method showed that upwind of the barrier, larger particles were

collected on the lower portion of the barrier and smaller particles dominated collected dust from the upper level samplers. Downwind of the barrier, PSD analysis generally showed a decrease of GMD values at all heights within the barrier (1.5, 3, 4.5, and 6 m), indicating the presence of the Osage orange barrier removed passing dust particles, especially large particles. However, small particles, such as $PM_{2.5}$ and PM_{10}, were removed most efficiently at the crown area of the tree (4.5 m and 6 m).

5.5. References

Bird, P.R., Bicknell, D., Bulman, P.A., Burke, S.J.A., Leys, J.F., Parker, J.N., van der Sommen, F.J., & Voller, P. 1992. The role of shelter in Australia for protecting soils, plants and livestock. *Agrofores. Sys.* 20: 59-86.

Brandle, J.R., Hodges, L., & Zhou, X.H. 2004. Windbreaks in North American agricultural systems. *Agrofores. Sys.* 61: 65-78.

Brantley, H.L., Hagler, G.S.W., Deshmukh, P.J., & Baldauf, R.W. 2014. Field assessment of the effects of roadside vegetation on near road black carbon and particulate matter. *Sci. Total Environ.* 468-469: 120-129.

Burley, H.K., Adrizal, A., Patterson, P.H., Hulet, R.M., Lu, H., Bates, R.M., Martin, G.P., Myers, C.A.B., & Atkins, H.M. 2011. The potential of vegetative buffers to reduce dust and respiratory virus transmission from commercial poultry farms. *J. Appl. Poult. Res.* 20(2): 210-222.

Cavanagh, J.E., Peyman, Z.R., & Wilson, J.G. 2009. Spatial attenuation of ambient particulate matter air pollution within an urbanised native forest patch. *Urban Forestry & Urban Greening* 8(1): 21-30.

Cleugh, H.A. 1998. Effects of windbreaks on airflow, microclimates, and crop yields. *Agrofores. Sys.* 41: 55-84.

De Zoysa, M. 2008. Casuarina coastal forest shelterbelts in Hambantota city, Sri Lanka: Assessment of Impacts. *Small-scale Fores.* 7: 17-27.

Dierickx, W. 2003. Field evaluation of windbreak protection for orchards. *Biosys. Eng.* 84: 159-170.

El-Flah, A.H. 2009. The use of various wind barriers in controlling wind erosion in Northwestern parts of Egypt. *J. App. Sci. Res.* 5(5): 490-498.

Ffolliott, P. 1998. Multiple benefits of arid land agroforestry home gardens and riparian ecosystems. In *Farming the forest for specialty products*. Proceedings of the Conference on Enterprise Development Through Agroforestry, ed., Josiah, S. J., 41-46. St. Paul, MN: Center for Integrated Natural Resources and Agriculture Management, University of Minnesota.

Fryrear, Donald W., & E. L. Skidmore. 1985. "Methods for Controlling Wind Erosion." In *Soil Erosion and Crop Productivity*, edited by R. F. Follett and B. A. Stewart. Madison, Wisc.: American Soc. Agronomy, Crop Sci. Soc. America, Soil Sci. Soc. America.

Gonzales, H.B., Maghirang, R.G., Wilson, J.D., Razote, E.B., & Guo, L. 2012. Measuring cattle feedlot dust using laser diffraction analysis. *Trans. ASABE.* 54(6): 2319-2327.

Grala, R.K., Tyndall, J.C., & Mize, C.W. 2010. Impact of field windbreaks on visual appearance of agricultural lands. *Agrofores. Sys.* 80: 411-422.

Grantz, D.A., Vaughn, D.L., Farber, R.J., Kim, B., Ashbaugh, L., VanCuren, T., & Campbell, R. 1998. Wind barriers suppress fugitive dust and soil-derived airborne particles in arid regions. *J. Environ. Qual.* 27(4): 946-952.

Gregory, N.G. 1995. The role of shelterbelts in protecting livestock: A review. *New Zealand J. Agri. Res.* 38: 423-450.

Guo, X. 2008. Function and structure of the farmland shelterbelts in northern area of Shanxi Province. *J. Fores. Res.* 13(3): 217-220.

Hagen, L. & Skidmore, E. 1971. Windbreak drag as influenced by porosity. *Trans. ASAE* 14: 464-465.

Harris, R.A., & Cohn, L.F. 1985. Use of vegetation for abatement of highway traffic noise. *J. Urban Planning Develop.* 11: 34-48.

Huang, C.H., Lee, C.I., & Tsai, C.J. 2005. Reduction of particle reentrainment using porous fence in front of dust samples. *J. Environ. Eng.* 131: 1644-1648.

Hyams, D.G. 2013. Curve expert 1.4 software. www.curveexpert.net

Jones, A.M., Harrison, R.M., & Baker, J. 2010. The windspeed dependence of the concentrations of airborne particulate matter and NO_x. *Atmos. Environ.* 44(13): 1682-1690.

Kort, J. 1988. Benefits of windbreaks to field and forage crops. *Agri. Ecosys. Environ.* 22-23: 165-191.

Kulshreshtha, K., Rai, A., Mohanty, C.S., Roy, R.K., & Sharma, S.C. 2009. Particulate pollution mitigating ability of some plant species. *Int. J. Environ. Res.* 3(1): 137-142.

Lazzaro, L., Otto, S., & Zanin, G. 2008. Role of hedgerows in intercepting spray drift: Evaluation and modelling of the effects. *Agric. Ecosys. Environ.* 123(4): 317-327.

Lin, M.Y. & Khlystov, A. 2012. Investigation of ultrafine deposition to vegetation branches in a wind tunnel. *Aerosol Sci. Tech.* 46: 465-472.

Lundgren, D.A., Hausknecht, B.J., & Burton, R.M. 1984. Large particle size dsitribution in five U.S. cities and the effect on a new ambient particulate matter standard (PM_{10}). *Aerosol Sci. Tech.* 3(4): 467-473.

Mader, T.L., Dahlquist, J.M., Hahn, G.L., & Gaughan, J.B. 1999. Shade and wind barrier effects on summertime feedlot cattle performance. *J. Anim. Sci.* 77(8): 2065-2072.

Ozer, S., Irmak, M.A., & Yilmaz, H. 2008. Determination of roadside noise reduction effectiveness of *Pinus sylvestris* L. and *Populus nigra* L. in Erzurum, Turkey. *Environ. Monit. Assess.* 144: 191-197.

Prenni, A.J., Siefert, R.L., Onasch, T.B., Tolbert, M.A., & Demott, P.J. 2000. Design and characterization of a fluidized bed aerosol generator: A source for dry, submicrometer aerosol. *Aerosol Sci. Technol.* 32(5): 465-481.

Raupach, M.R., Woods, N., Dorr, G., Leys, J.F., & Cleugh, H.A. 2001. The entrapment of particles by windbreaks. *Atmos. Environ.* 35: 3373-3383.

Sellier, D., Brunet, Y., & Faurcaud, T. 2008. A numerical model of tree aerodynamic response to a turbulent flow. *Forestry* 81(3): 279-297.

Smith, J.L., & Perino, J.V. 1981. Osage Orange (*Maclura pomifera*): History and economic uses. *Econ. Bot.* 35(1): 24-41.

Sudmeyer, R.A., Crawford, M.C., Meinke, H., Poulton, P.L., & Robertson, M.J. 2002. Effect of artificial wind shelters on the growth and yield of rainfed crops. *Aus. J. Exp. Agric.* 42: 841-858.

Tiwary, A., Morvan, H.P., & Colls, J.J. 2005. Modelling the size-dependent collection efficiency of hedgerows for ambient aerosols. *Aerosol Sci.* 37: 990-1015.

Tiwary, A., Morvan, H.P., & Colls, J.J. 2008. Collection of ambient particulate matter by porous vegetation barriers: Sampling and characterization methods. *Aerosol Sci.* 39: 40-47.

Tyndall, J., & Colletti, J. 2007. Mitigating swine odor with strategically designed shelterbelt systems: a review. *Agrofores. Sys.* 69(1): 45-65.

Vischetti, C., Cardinali, A., Monaci, E., Nicelli, M., Ferrari, F., Trevisan, M., & Capri, E. 2008. Measures to reduce pesticide spray drift in a small aquatic ecosystem in vineyard estate. *Sci. Total Environ.* 389(2-3): 497-502.

CHAPTER 6 - Computational Fluid Dynamics Simulation of Airflow through Standing Vegetation

6.1. Introduction

Wind erosion poses a significant risk to agricultural lands despite numerous mitigation strategies employed for erosion reduction. One control strategy is the maintenance of vegetation cover at the soil surface. Previous studies focused on effects of sparse vegetation as a result of harvesting (Wolfe and Nickling, 1993; Hagen, 1996; Lancaster and Baas, 1998), land degradation as a result of land conversion (Li et al., 2005), dry land conditions, and low precipitation (Musick and Gillette, 1990; Toure et al., 2011) - conditions that make the soil surface vulnerable to wind erosion.

Previous studies have used wind tunnels to identify parameters and conditions that dictate the extent of wind erosion damage. Lyles and Allison (1976) compared spacing and orientation of standing stubble for mitigating effects of wind erosion. Their study showed that a perpendicular stubble orientation was more effective than a parallel stubble orientation for sheltering against wind erosion. Densities of simulated plant stalks with various diameters and heights were employed by van de Ven et al. (1989), resulting in up to 82% soil loss reduction due to the presence of stalks. Hagen and Armbrust (1994) proposed a theoretical approach of including surface friction velocity reduction and interception via saltation in standing stalks to predict the amount of soil loss. They found a high correlation ($R^2 = 0.89$) between soil loss reduction and plant area index of stalks. Standing sticks for their wind tunnel study were used by Dong et al. (2001) to demonstrate that height and density of standing vegetation influences roughness length and drag coefficient. They also deduced that the height/spacing ratio is the

most essential structural parameter that influences values of drag coefficients and roughness lengths.

Field studies have also been conducted to determine the effects of vegetated surfaces on wind erosion. Stockton and Gillette (1990) evaluated three test sites, and they found that dense vegetation corresponded to large area for sheltering as evidenced by small ratios of threshold friction velocities of vegetated surface to bare soil surface. Their measurements showed a range of 0.27 to 0.44, in which a value of 1.0 denotes bare sand configuration. A study by Li et al. (2005) on degraded grasslands in China showed that early stages of vegetation were more prone to wind erosion, while established grasses showed greater resistance to wind erosion. They found that wind erosion reduction could lower wind erosion rate to 1/47 of that of the fixed sandy land.

Field testing (Fryrear et al., 1991) is desirable to ensure realistic conditions, while use of wind tunnels is necessary to control a set of meteorological and soil parameters (e.g., soil type, wind speed, vegetation element type, and vegetation configuration). Both On-site field testing and wind tunnel testing are expensive and time consuming. Numerical simulation with computational fluid dynamics (CFD), combined with sufficient validation, provides an alternative approach to wind erosion research (Politis et al., 2008; Quiao and Liu, 2008; Defraeye et al., 2010; Bonifacio et al., 2014).

Numerical simulation using commercially available CFD software (e.g. Fluent) on various types of vegetation models (natural and artificial) has been studied extensively. Tiwary et al. (2005) used three tree species (Hawthorn, Holly, and Yew) to implement the turbulence model described by Menter (1994) as the shear stress transport (SST) with which they modeled airflow across the Hawthorn hedges. Lin et al. (2007) studied airflow and odor dispersion across tree shelterbelts, and they employed the $k-\omega$ turbulence closure model to accurately model

dispersion plumes. Rosenfeld et al. (2007) investigated airflow through various configurations of Cypress trees where they used individual trees and multiple rows of shelterbelts to compare to their experimental results. They concluded that reduced flow and lateral variations in wind speed were caused by canopy density. Gromke et al. (2008) investigated airflow and exhaust dispersion across trees planted along roads in an urban street canyon. They found that the Reynolds stress model (RSM) was better than $k-\varepsilon$ as a turbulence closure model for predicting dispersion occurring within trees. Endalew et al. (2009) attempted to model 3D architecture of leafless plant canopies using commercial CFD. They employed the standard $k-\varepsilon$ turbulence model and found that predicted velocities agreed with experimental results. Bitog et al (2012) compared wind tunnel measurements of the airflow across black pine trees and CFD simulations. They used Re-Normalization Group (RNG) $k-\varepsilon$ turbulence model and assessed the effects of gaps and rows between trees. Guo and Maghirang (2012) compared experimental values of Tiwary et al. (2005) to the CFD simulation using the standard $k-\varepsilon$ and realizable $k-\varepsilon$ turbulence closure models; they found good agreement between the two models.

Open-source codes, including Open-source Field Operation And Manipulation (OpenFOAM), has been gaining popularity in many disciplines because of the high cost of commercial CFD packages. Lysenko et al. (2013) reported that the performance of FLUENT and OpenFOAM in simulating flows across a bluff body were comparable. Higuera et al. (2013) used OpenFOAM to simulate realistic surface waves for hydrodynamic simulation. Bonifacio et al. (2014) compared results of AERMOD to OpenFOAM simulation to simulate particle transport from a ground-level source.

This study aimed to numerically model airflow through artificial standing vegetation using OpenFOAM. A specific solver of OpenFOAM architecture (simpleFoam) was tested to

simulate airflow through canopies using actual 3D structure of canopy in the wind tunnel created using another open source CAD geometry software (Salomé platform ver. 7.2, 2013). This study included the following specific objectives:

1) Model airflow through standing vegetation using open-source CFD software; and
2) Compare results of wind tunnel investigations to results of the CFD model for tested wind tunnel configurations.

6.2. Materials and Methods

6.2.1. Wind Tunnel Experiment

A detailed description of the wind tunnel experiment that was the basis for the comparison with a CFD simulation is discussed in Chapter 3. A majority of comparisons were based on wind velocity measurements from the pitot tube system within the artificial standing vegetation. Velocity profiles from the experiment were used to determine effective drag coefficient (C_n) values within the standing vegetation that were compared to the results of CFD simulation. A detailed derivation of the equation for C_n was shown by Endalew et al. (2010), and the resulting final equation used in this study is

$$C_n(z) = \frac{1}{LA} ln \frac{U_{up}(z)}{U_{down}(z)} \tag{6.1}$$

where $C_n(z)$ is the value of C_n at various vertical positions, L is the distance (m) between upwind and downwind positions of measurements of wind velocities, A is leaf area density (m^{-1}), $U_{up}(z)$ are mean vertical velocities in the upwind position, and $U_{down}(z)$ are mean vertical velocities in the downwind position. Mean values of upwind and downwind locations include velocity measurements taken at a single line at the back or front of the canopy. For example, at a

constant value of x, velocities must be taken at different y-positions upwind and downwind along the vertical height (z) of the canopy, as illustrated in Figure 6.1.

6.2.2. Computational Domain

The computational domain (Figure 6.1) is based on measurements of wind velocity profiles in the wind tunnel; the maximum height of the domain corresponds to freestream velocities measured within the wind tunnel (i.e., freestream velocities were measured at 0.9 m from the tunnel floor). Length and width of the domain was limited by the number of standing vegetation elements chosen to represent the simulation to minimize computation time but able to represent and show changes between wind profiles of artificial vegetation setup. For this study, seven elements were chosen to illustrate the behavior of wind velocities between rows for various artificial standing vegetation configurations within the tunnel (100×200, 200×200, and 300×200 mm spacings for two heights of vegetation at 150 mm and 220 mm).

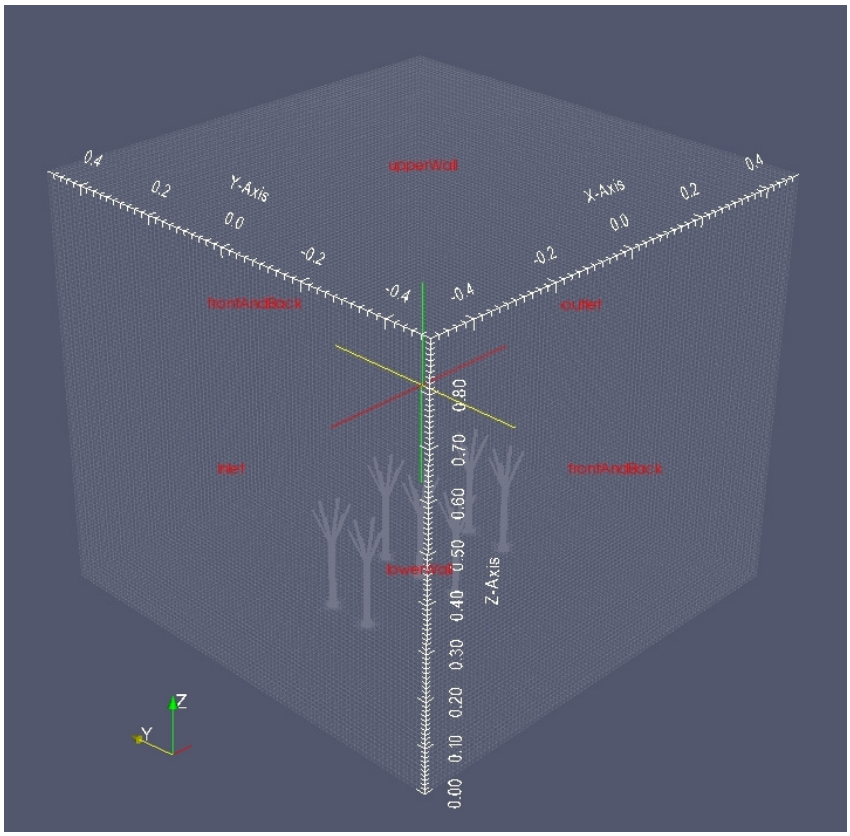

Figure 6.1. Computational domain for airflow through artificial standing vegetation using ParaView.

Table 6.1. Computational grid for the artificial standing vegetation.

Cells		1046096
Faces		3258462
Nodes		1172843
x coordinate (m)	min	-0.5
	max	0.5
y coordinate (m)	min	-0.5
	max	0.5
z coordinate (m)	min	0
	max	0.9

6.2.3. Numerical Simulation

CFD modeling involves three steps: preprocessing, processing, and post-processing. Preprocessing requires creation of the geometry and domain for the mesh. Requirements for the mesh are also dependent on the type of solution required, whether an internal flow (within the 3D CAD model) or an external flow (outside the 3D CAD model). This study was an external flow, and the geometry and domain were created accordingly. OpenFOAM (ver. 2.2.2, ESI-OpenCFD, openfoam.org) was the CFD software used in this study. Processing requires a specific solver within the OpenFOAM solution binaries programmed using C++. Post-processing was performed using ParaView installed with OpenFOAM software that automatically visualizes the simulation solution. Values generated from the solution were also exported and visualized using Microsoft Excel (Microsoft Corp.) for cross-checking and validation.

6.2.3.1. Governing Equations

This study focused turbulent airflow through a barrier (standing vegetation). The Reynolds-averaged Navier-Stokes (RANS) method was adopted because it is representative of turbulent components of instantaneous velocities of the fluid. Equations were based on 3D RANS steady-state, incompressible, isothermal, taking the turbulent atmospheric layer as neutrally stratified (Guo and Maghirang, 2012), and the mass transfer was neglected. Continuity and momentum conservation equations used (Cheng et al., 2003; Endalew et al., 2009; Yeh et al., 2010) were as follows:

$$\frac{\partial \overline{u_i}}{\partial x_i} = 0 \tag{6.2}$$

$$\frac{\partial u_i u_j}{\partial x_j} = -\frac{1}{\rho}\frac{\partial p}{\partial x_i} + \frac{1}{\rho}\frac{\partial}{\partial x_j}\mu\left(\frac{\partial u_i}{\partial x_j} + \frac{\partial u_j}{\partial x_i}\right) - \frac{\partial}{\partial x_j}\left(\overline{u_i' u_j'}\right) \tag{6.3}$$

where *i* is the subscript for all three directions (*x*, *y*, and *z*), *j* is the subscript for the direction evaluated (*x*, *y*, or *z*), u is the velocity (m s^{-1}), p is the pressure force (Pa) in *i*-direction evaluated, ρ is the fluid density (kg m^{-3}), and μ is the fluid viscosity (N s m^{-2}).

The RNG *k*-ε model was used (Yeh et al., 2010; Bitog et al., 2012):

$$\frac{\partial}{\partial x_i}(\rho k u_i) = \frac{\partial}{\partial x_j}\left[\alpha_k \mu_{eff} \frac{\partial k}{\partial x_i}\right] + G - \rho\varepsilon \tag{6.4}$$

$$\frac{\partial}{\partial x_i}(\rho \varepsilon u_i) = \frac{\partial}{\partial x_j}\left[\alpha_\varepsilon \mu_{eff} \frac{\partial \varepsilon}{\partial x_i}\right] + C_{1\varepsilon}\frac{\varepsilon}{k}(G) - C_{2\varepsilon}^{*}\rho\frac{\varepsilon^2}{k} \tag{6.5}$$

$$G = 2\mu_t S_{ij} S_{ij} \tag{6.6}$$

$$\mu_t = \rho C_\mu \frac{k^2}{\varepsilon} \tag{6.7}$$

where k is the turbulence kinetic energy (m^2 s^{-2}), α_k is the Prantdl number of the turbulence kinetic energy, ε is the turbulence dissipation rate (m^2 s^{-3}), α_ε is the Prantdl number of the turbulence dissipation rate, μ_{eff} is the effective viscosity (N s m^{-2}), S_{ij} is the strain rate tensor, μ_t is the turbulent viscosity (N s m^{-2}), and $C_{1\varepsilon}$ is a turbulence model constant equal to 1.42. $C_{2\varepsilon}^{*}$ is defined as follows:

$$C_{2\varepsilon}^{*} = C_{2\varepsilon} + C_{2\varepsilon}' \tag{6.8}$$

where $C_{2\varepsilon}$ is a turbulence model constant equal to 1.68 while $C_{2\varepsilon}'$ is further defined by the equation:

$$C_{2\varepsilon}' = \frac{C_\mu \rho \eta^3 (1-\eta/\eta_0)}{1+\beta\eta^3} \tag{6.9}$$

where η_o is a constant equal to 4.38 and η is further defined by the equation:

$$\eta = S\frac{k}{\varepsilon} \tag{6.10}$$

$$S = \sqrt{2S_{ij}S_{ij}} \tag{6.11}$$

The equations that define the turbulence kinetic energy and turbulence dissipation rate are as follows:

$$k = \frac{3}{2}\left(V_{avg}I\right)^2 \tag{6.12}$$

$$\varepsilon = C_{\mu}^{3/4}\frac{k^{3/2}}{\ell} \tag{6.13}$$

where V_{avg} is average velocity and I is turbulence intensity.

Previous studies (Lee and Lim, 2001; Packwood, 2000; Lee et. al., 2007; Li et al., 2007; Santiago et al., 2007; Bourdin and Wilson, 2008; Yeh et al., 2010; Bitog et al., 2012) indicated that the RNG $k-\varepsilon$ model was the most suitable turbulence model for investigating complex wind flows around barriers.

6.2.3.2. Geometry and Mesh Generation

For OpenFOAM, geometries for internal flows are typically created using a meshing tool, blockMesh, which creates fully-structured hexahedral meshes. For external flow as in this study, however, that tool cannot be used. For this study, 3D geometry was based on geometry of the artificial standing vegetation used in the wind tunnel (Figure 6.2). A third-party software, the Salome Platform (Open Cascade, Guyancourt, France), was used to create the geometry to be "snapped" or overlapped with the block domain using the other mesh tool of OpenFOAM, snappyHexMesh (built-in meshing tool suitable for creating internal faces within a domain necessary to evaluate external flows). The created 3D models were exported as sterelitography (.stl) file in ASCII format (file format recognized by snappyHexMesh).

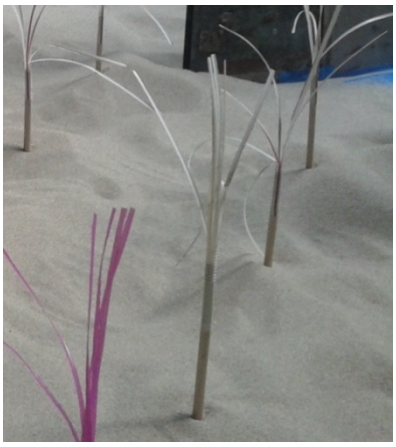

Figure 6.2. Actual standing vegetation model used in the wind tunnel.

6.2.3.3. Use of OpenFOAM for Simulation

SimpleFoam was used for this study because the solver is applicable to steady-state, incompressible turbulent flow. It utilizes the semi-implicit method for the pressure-linked equation (SIMPLE) algorithm developed by Patankar (1980) for decoupling pressure and velocity (OpenCFD, 2011). For a specific solver, various types of files are necessary. For simpleFoam solver, the three major folders (0, constant, and system) are necessary.

The 0 folder requires files necessary for initial and boundary conditions for ε, k, μ_t, p, and U. The constant folder requires files for the geometry (i.e., blockMeshDict, STL files) and the type of turbulence model to be used, defined in the file named RASProperties (Reynolds-average simulation properties). The system folder contains files necessary to control the extent of iteration runs via the ControlDict file (control dictionary file), parallel decomposition for parallel runs defined in decomposeParDict file, snappyHexMeshDict file that contains the file for setting up the mesh for the geometry, solution mechanisms in the file fvSolution (i.e., defines solvers for turbulence parameters and sets up relaxation values and residual control values), and numerical

schemes in the file fvSchemes (i.e., defines the numerical approach for various operators in the main equation: steady-state, Gauss linear, upwind differencing) (OpenCFD, 2011).

Table 6.2. Input parameters and their values for CFD simulation of airflow through artificial standing vegetation (OpenCFD, 2011; Guo and Maghirang, 2012; Bonifacio et al., 2014).

Parameter	Symbol	Value
Air density (kg m^{-3})	ρ	1.225
Air dynamic viscosity (kg m^{-1} s^{-1})	μ	1.79 x 10^{-5}
Kinematic viscosity (m^2 s^{-1})	υ	1.46 x 10^{-5}
Turbulence model constant	$C_{1\varepsilon}$	1.42
Turbulence model constant	$C_{2\varepsilon}$	1.68
Turbulence model constant	C_{μ}	0.085
Turbulence model constant	β	0.012
Turbulence model constant	η_o	4.38
Turbulence Prandtl number for k	σ_k	0.719
Turbulence Prandtl number for ε	σ_ε	0.719
von Karman constant	κ	0.4187

6.2.3.4. Boundary Conditions

Boundaries for the entire domain were set in the format read by the OpenFOAM solver. Initial values for ε, k, p, and U were necessary to initialize the solver, and they were placed as separate files in the 0 folder. These values were set for regions in the domain, namely, inlet, outlet, upperWall, lowerWall, front and back regions. Inlet values for ε and k were based on the equilibrium boundary layer assumption (described by Richards and Hoxey, 1993; Santiago et al.,

2007; Bourdin and Wilson, 2008; Yeh et al., 2010; Guo and Maghirang, 2012), obtained by the following equations:

$$k_{in} = \frac{u_*^2}{\sqrt{C_\mu}} \tag{6.14}$$

$$\varepsilon_{in} = \frac{u_*^3}{\kappa z} \tag{6.15}$$

where u_* is friction velocity far upstream of the vegetation element (from previous wind tunnel tests, u_* = 0.24 m s^{-1}). Pressure was initally set as zero (0 Pa) inside the domain (internalField in OpenFOAM) and was given zero gradient for inlet, upperWall, front and back; symmetry condition for upperWall; and constant outlet value. For other regions in the domain, outlet flow was given a fully-developed flow condition (i.e., zero velocity gradient), symmetry condition at the upperWall, back and front regions, no-slip condition at the lowerWall, and near-wall conditions for ε and k (i.e., $epsilonWallFunction$ and $kqrWallFunction$, respectively) for all other domain regions were utilized.

Initial values inside the domain (internalField in OpenFOAM) for all parameters were set to zero. Wind velocity measurements during the wind tunnel experiment served as input values for *x*-component inlet velocities (u_x); other velocity components u_y and u_z were assumed to be zero.

6.2.3.5. Post-Processing

Visualization of simulation results was done in Paraview 3.40. During computation (iteration steps), OpenFOAM intermediary results were cross-checked for stability, unboundedness, and residual behavior by installing the GNUPlot that aids visualization of results to ensure that parameters computed during numerical simulation are acceptable and whether or not convergence is met.

Velocity profiles measured during the wind tunnel experiment of various standing vegetation configurations were compared to simulation results. The option was available to export data from the ParaView contour plot to a .csv (comma-separated values format) that can then be read through the preferred spreadsheet program: Ubuntu has freeware Libre Office Calc, although some visualizations are limited but could be conducted using Microsoft Excel spreadsheet for Windows users. A useful option from ParaView was to filter out desired points or region within the domain to export data within ParaView; failure to do so causes an error because the entire set of data exceeds the maximum allowable rows in the spreadsheet program, especially if the mesh contained millions of cells.

6.2.3.6. Data Analysis

Mean values of wind velocities, optical porosities, and drag coefficients were compared using the normality and homogeneity of variances assumption and a standard statistical test (e.g., paired t-test using Microsoft Excel (Microsoft Corp., Redmond, Wash.)). An analysis of variance (ANOVA) was done to determine the effect of vegetation densities and heights. A 5% level of significance was used for all cases. CurveExpert 1.4 (Hyams, 2013) was used to plot best-fit curves that were compared to the curve fitting tool in Microsoft Excel (Microsoft Corp., Redmond, Wash.).

6.3. Results and Discussion

6.3.1. Geometry and Mesh Generation

Figure 6.3 shows the 3D model for the artificial standing vegetation created using Salome platform. The (.stl) file format of the 3D geometry was called within the dictionary of the snappyHexMesh meshing tool of OpenFOAM. In addition to geometry reconstruction, much of

mesh parameters' conditioning (i.e., level refinement, layer refinement, angles) was needed and evaluated as a result of a trial-and-error solution to obtain an accepted mesh (Figure 6.3) to proceed with iteration steps of the simulation (i.e., very fine mesh led to a very long computational procedure). Although mesh quality increased with the addition of sublayers, especially at edges of geometries in the snappyHexMesh step, the decision was made to ignore adding sublayers because the geometry was too small to add more layers and that the mesh created when sublayers were added almost always led to failure in mesh checks. During mesh creation, the mesh size of the domain (through blockMesh) dictates whether or not problematic faces would be created since, by default, snappyHexMesh creates a very fine mesh. Therefore, if blockMesh has a coarse mesh and the "snapped" figure has a relatively fine mesh, failed mesh checks would be present, resulting in unboundedness and divergence of the solution.

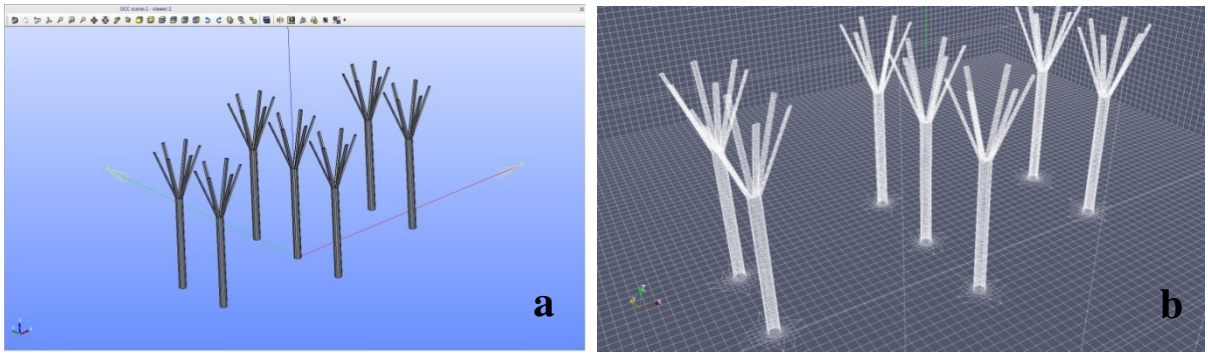

Figure 6.3. (a) Geometry created using Salome and (b) mesh created using snappyHexMesh for the 100 × 200 mm configuration at 220 mm standing vegetation height.

6.3.2. Use of OpenFOAM for Simulation

Applicability of the simpleFoam solver was tested for a rectangular block with simulation parameters and domain based on the study by Guo and Maghirang (2012). Good correlation existed between simulation results around a porous fence for the Guo and Maghirang (2012)

study and results obtained using OpenFOAM shown by similar horizontal velocity contours downwind of the rectangular block barrier, as illustrated in Figure 6.4. As shown in the figure, the two figures demonstrate parallelism with triangular-shaped wind speed reduction zones that extend far downwind of the barrier and a slight reduction of wind upwind of the barrier block. OpenFOAM simulation was also able to simulate the same observation as Guo and Maghirang (2012) with an increase in wind velocities above the block and a decrease of velocities further from the barrier as wind become close to the ground due to the mixing zone resulting from the wind profile being displaced at such regions.

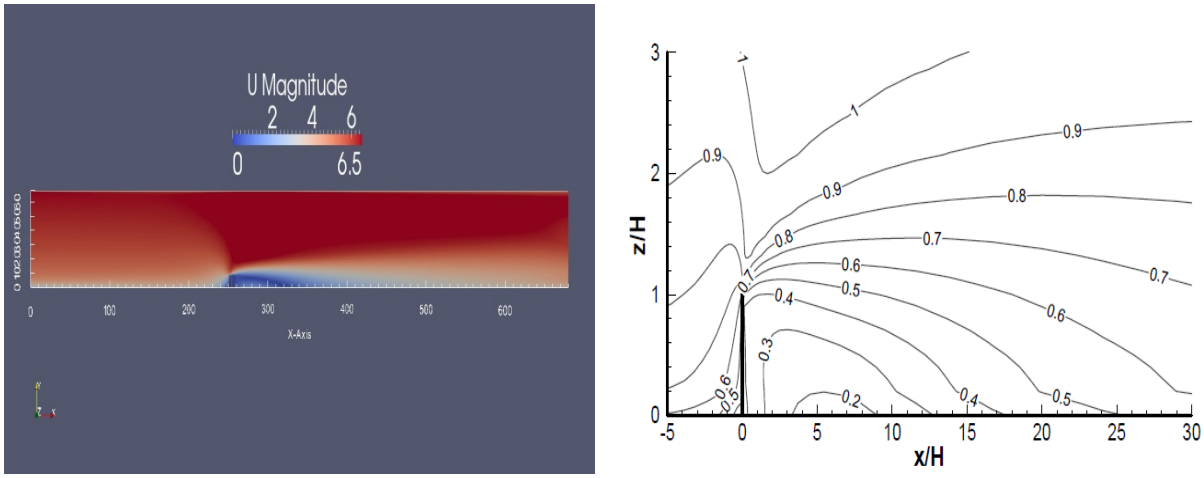

Figure 6.4. Horizontal velocity contours for (a) rectangular block using OpenFOAM and (b) fence simulation by Guo and Maghirang (2012).

6.3.3. Comparison of OpenFOAM Results with Experimental Results

Values of C_n for the various standing vegetation configurations are shown in Figure 6.5. As shown in the figure, although numerical values of C_n did not differ significantly ($p > 0.05$) between results of the OpenFOAM simulation and experimental results, profile shapes were slightly different, especially for denser configurations (100×200 mm), possibly as a result of

pertinent oscillations of airflow that created excessive turbulence as the density of standing vegetation increased. Slight discrepancies of profile shapes could be caused by the difference in what occurs during the experiment when the upper portion of the standing vegetation is subjected to bending motion as air travels through it - the oscillatory motions of the standing vegetation, which were unaccounted for during OpenFOAM simulation.

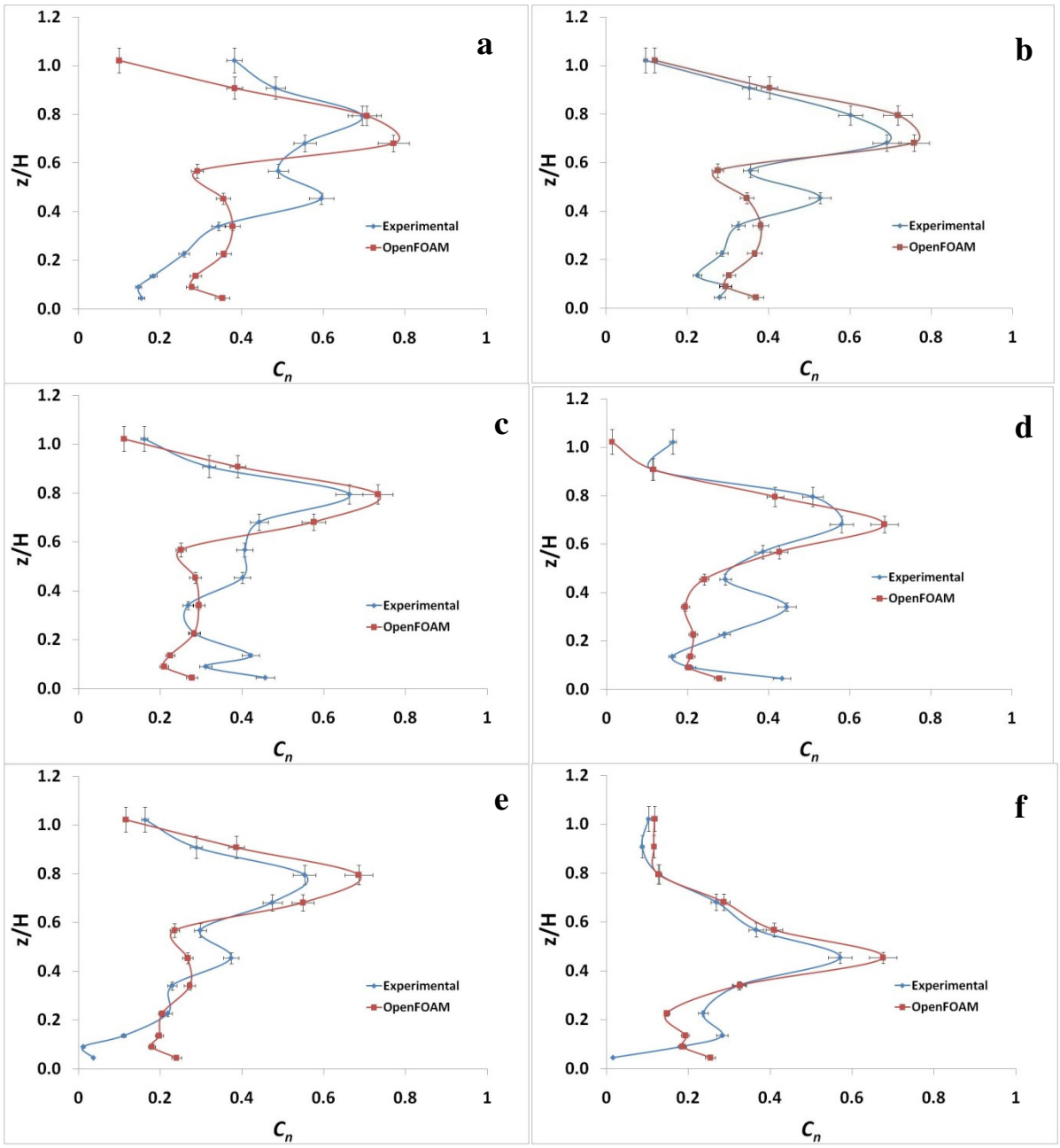

Figure 6.5. Vertical profiles of effective drag coefficient (C_n) for the different artificial standing vegetation configurations: (a) 100 × 200 at 220 mm ht; (b) 100 × 200 at 150 mm ht; (c) 200 × 200 at 220 mm ht; (d) 200 × 200 at 150 mm ht; (e) 300 × 200 at 220 mm ht; and (f) 300 × 200 at 150 mm ht. Error bars represent values within 5%.

A plot of the comparison of the normalized wind profile is shown in Figure 6.6 for the 100 × 200 mm at 220 mm standing vegetation height configuration. The comparison was made at velocities measured at 100 mm from the back of the canopy. This measurement essentially is half of the constant row spacing (200 mm) between configurations. Vertical height z was normalized with the height of the canopy, while velocity U was normalized by maximum velocity for the simulation or experiment. OpenFOAM simulation maximum velocity occurs at the topmost of the boundary, z = 0.9 m, which is the height of freestream velocity during the wind tunnel experiment, coinciding with maximum velocity within the tunnel.

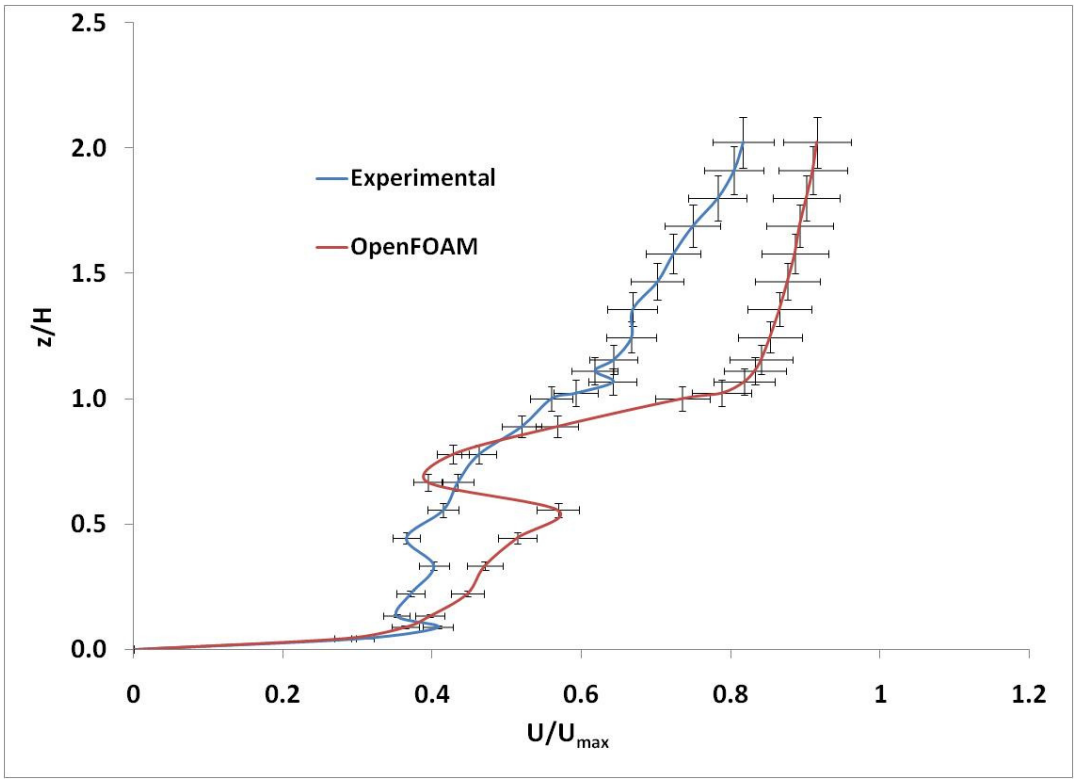

Figure 6.6. Comparison of normalized velocity profiles from the wind tunnel experiment and OpenFOAM simulation (measurements at the back of canopy for the 100 × 200 mm at 220 mm height configuration). Error bars represent values within 5%.

Slight differences in the shapes of velocity profiles between measured values during the wind tunnel experiment and simulation results are evident in Figure 6.6. Simulation results showed a dramatic decrease of velocities at the height of the canopy where the split portion of straws were systematically present. However, for measured values, this was not the case. Actual measurements showed limited decrease in velocities (limited drastic change in profile shape) at the wake of the canopy, but fluctuating values of wind velocities were evident. This could be attributed to the canopy behavior during the actual experiment. For simulation results, split portions of the straws were stationary and straw bending or oscillatory motions were not accounted for during simulation. However, during experimentation, continuous oscillatory motion of plastic straws within the canopies was evident when the standing vegetation is subjected to wind, potentially leading to overflows around the standing vegetation (above and at the sides of the canopy).

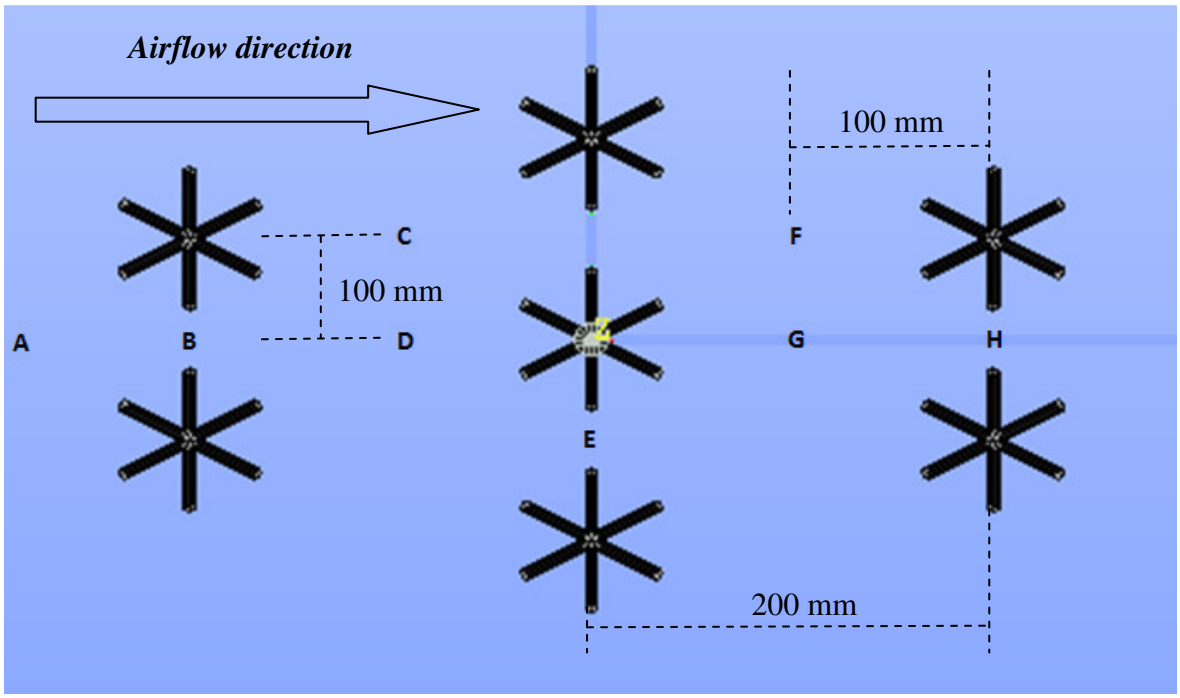

Figure 6.7. Top view of positions considered for velocity profile comparison (100 × 200 mm configuration illustrated).

Figure 6.8 shows comparisons of normalized predicted velocity profiles within the canopy at various regions (illustrated in Figure 6.7) across the domain for all standing vegetation configurations. The same regions were selected for all other configurations, that is, regions that represent in-between rows (C, D, F, and G), in-between canopies within a row (B,E, and H), and upwind of vegetation (A). Normalization was achieved by dividing vertical velocities with maximum velocity (velocity at the height of domain, z = 0.9 m, which represents maximum velocity within the tunnel and measured as freestream velocity).

The plots in Figure 6.8 showed expected behavior of normalized velocity profiles at the wake of the canopy identical to the observation in previous studies (Cionco and Ellefsen, 1998; Katul et al., 2004; Pyles et al., 2004; Endalew et al., 2010). Regions B and D had identical log profiles for velocity, similar to the upwind region A, as expected because no obstructions were in front of region A, B, and D even if they were within the canopy region. Figure 6.8 also showed that a reduction of wind velocities occurred within the canopy height and, as shown in Figure 6.8, the resistance resulting from the presence of split straws (approximately 0.15 to 0.22 value of z/H) were causes of a drastic decrease of velocities, as demonstrated by the sharp skewness of the profile towards the left as the wind hit the canopy for locations in which standing vegetation was an obstruction.

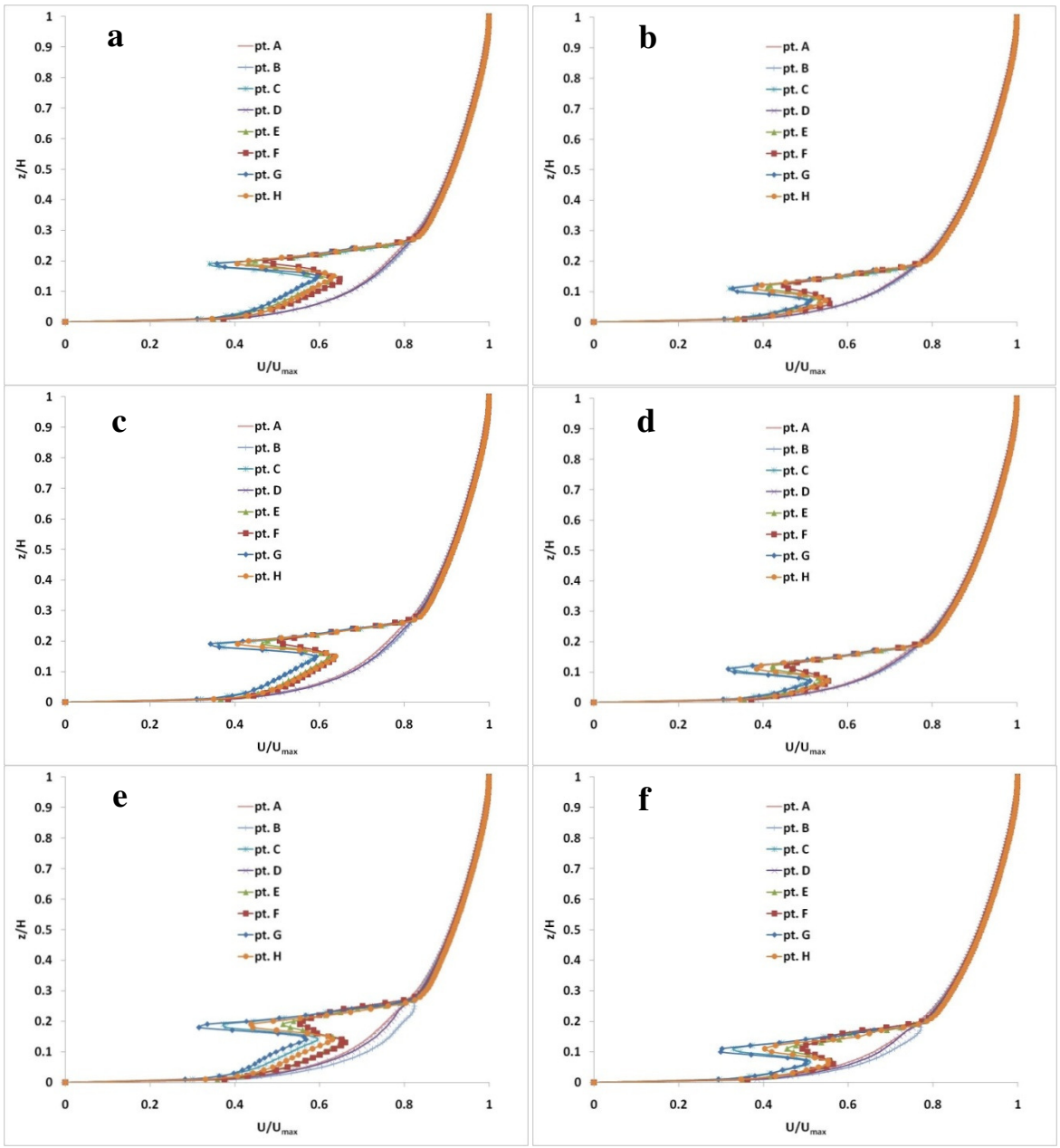

Figure 6.8. Comparison of predicted velocity profiles within the canopy for standing vegetation configurations: (a) 100 × 200 at 220 mm ht, (b) 100 × 200 at 150 mm ht, (c) 200 × 200 at 220 mm ht, (d) 200 × 200 at 150 mm ht, (e) 300 × 200 at 220 mm ht, and (f) 300 × 200 at 150 mm ht.

The same type of velocity profiles was observed for other configurations for the same regions portrayed. The difference between profiles for the same height configuration was that

wake velocities at Regions E and F were slightly lower for denser configurations (lowest for the densest configuration 100×200 mm) compared to other density types. Obstructions due to presence of vegetation can be seen as a greater depth of plot towards the left of the graph (more skewed to the left) at the region of velocity reduction, implying that the presence of additional standing vegetation would lead to better sheltering downwind. In addition, comparison of the same density with different heights (150 mm versus 220 mm) of standing vegetation configuration showed that the area of velocity reduction was greater for taller standing vegetations.

Investigation of contour plot of predicted velocities (Figure 6.9) within the standing vegetation showed that a majority of the displaced profiles (due to standing vegetation above and at the sides of the vegetation) were responsible for instantaneous increase of wind velocities, explained by the fact that since canopies were present, their resistance was compensated by the presence of overflows and instantaneous increases of wind velocities around the standing vegetation (Endalew et al, 2009). This region, known as the roughness sublayer (Georgiadis et al., 1996), dictates turbulence in airflow due to complexity and three-dimensionality of canopy structures.

A detailed discussion of the regions that comprised the roughness sublayer is given by Endalew et al. (2010). The region in which a majority of velocity reductions occur, as seen in Figure 6.9, is the canopy flow region where oscillations in airflow occur, rendered by increased entropy of the fluid at the wake and within the canopy. Therefore, turbulence kinetic energy (k) and turbulence intensity (I) are both increased.

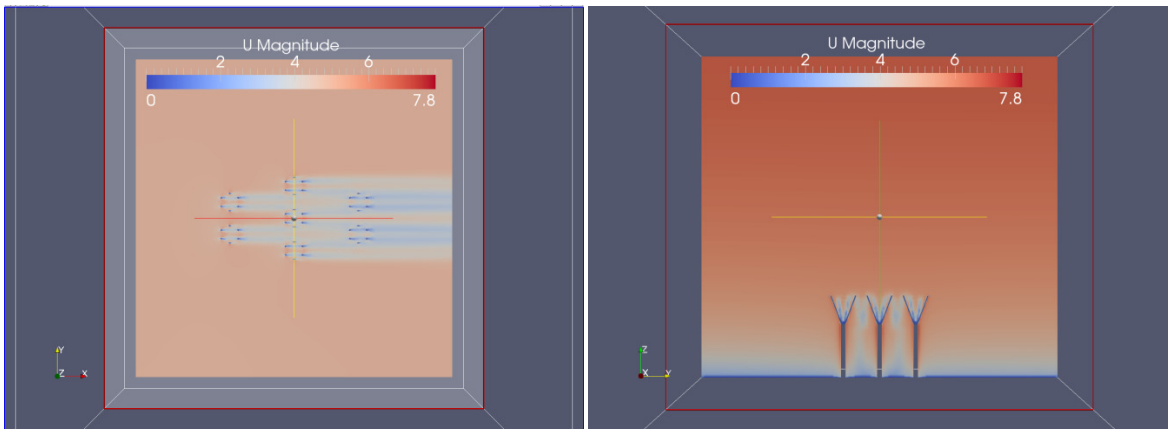

Figure 6.9. Slice view of the velocity contour for CFD simulation of the artificial standing vegetation.

Figure 6.10 shows a plot of typical profiles for normalized k as observed within the standing vegetation for the various configurations. The value of k was normalized by the square of the velocity (U^2), while vertical height (z) was normalized by the height of the canopy (H). To identify the region being considered as the canopy flow region, vertical boundaries for plots in Figure 6.11 were set at 1.6 times the height of the canopy because transition flow is believed to occur beyond this height (Cellier and Brunet, 1992; Wieringa, 1993). Comparisons included in Figure 6.10 are for regions that were well within the canopy and were obstructed by the presence of standing vegetation. The plots show that as the standing vegetation density increases, the value of k for the same region at different standing vegetation configurations also increases, proving that resistance employed by vegetation elements promotes greater turbulence in airflow within the perimeter of the standing vegetation.

As expected, disturbed regions were regions that had been obstructed by the presence of the canopies (all regions except region A, B, and D were plotted). The plots also imply that increased turbulence in airflow primarily occurred at regions in which split straws were present (z/H = 0.6) to a height that extended above the canopy height to approximately 25% of its height

(z/H = 1.25). Because of the structure complexity of the modeled standing vegetation, the argument could be made that specific regions were mostly disturbed within the canopy as shown in Regions C, G, and H. In general, however, regions between rows within the canopy were disturbed portions of the flow field that were illustrated by skewness and fluctuations in the line plots of Figure 6.10.

Because the same type of normalized k profiles were observable for all other standing vegetation configurations, evaluation of differences between values obtained during the experiment and those from the CFD simulation is useful. Figure 6.11 compares normalized profiles of k and OpenFOAM simulation and computations using results of the wind tunnel experiment. A large difference exists between the shapes of the two profiles, especially the ones at the lower portions close to the ground. Endalew et al. (2010) obtained the same observation, stating that such phenomenon could occur due to the limitation of all turbulence models derived from RANS equations to illustrate large number of velocity fluctuations that occur within investigated regions because of their dependence on parameter inputs, constants, and basic assumptions made during the iteration procedures. (Motions of the split straw portion were not considered for the simpleFoam solver because the mesh used was not a dynamic mesh.) In addition, the difficulty in assessing and recreating 3D geometry, mesh, and boundary conditions also limited the domain considered in calculations, thus hampering results of airflow modeling around the standing vegetation.

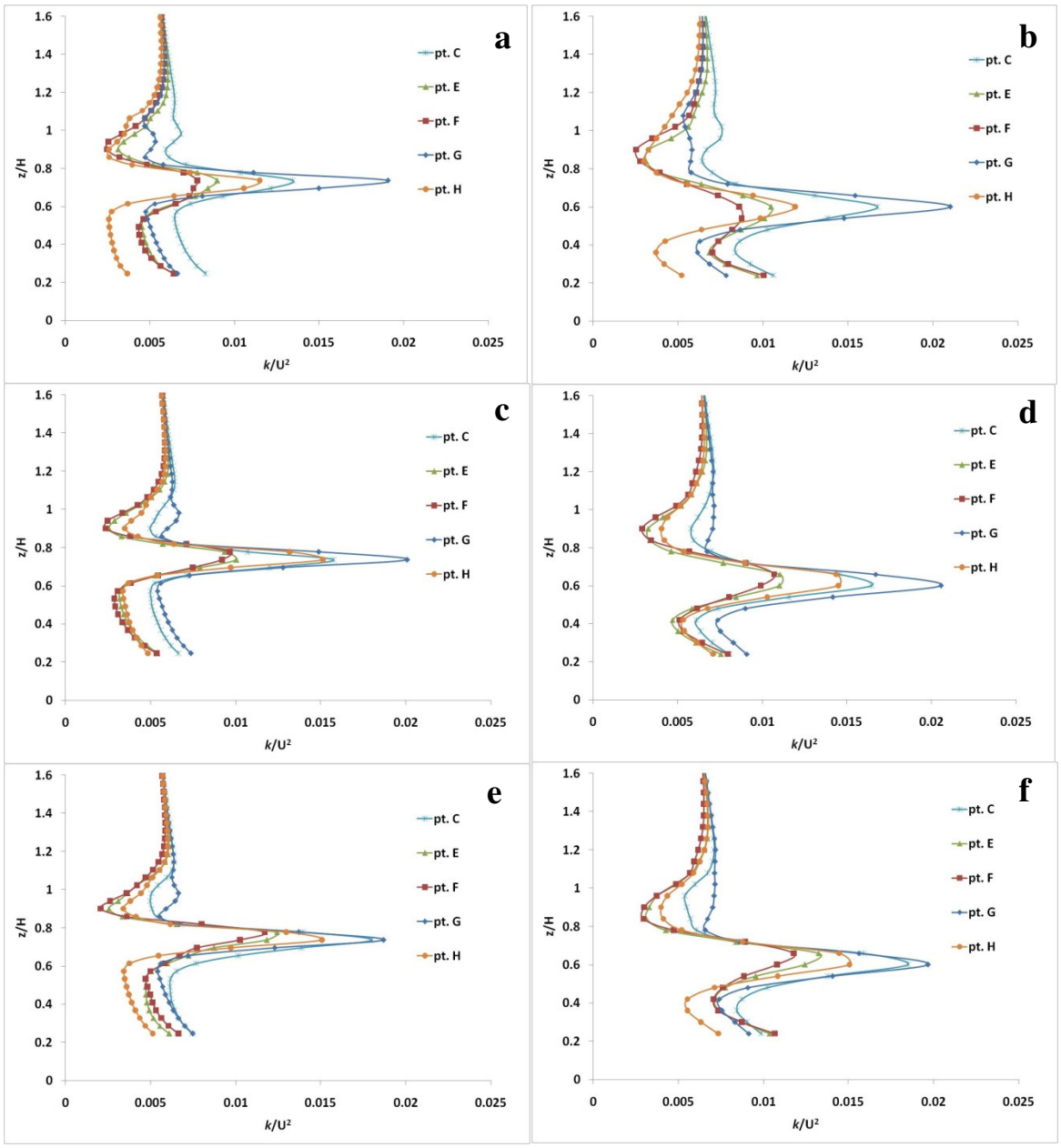

Figure 6.10. Normalized *k* profiles for standing vegetation configurations for CFD simulation: (a) 100 × 200 at 220 mm ht, (b) 100 × 200 at 150 mm ht, (c) 200 × 200 at 220 mm ht, (d) 200 × 200 at 150 mm ht, (e) 300 × 200 at 220 mm ht, and (f) 300 × 200 at 150 mm ht.

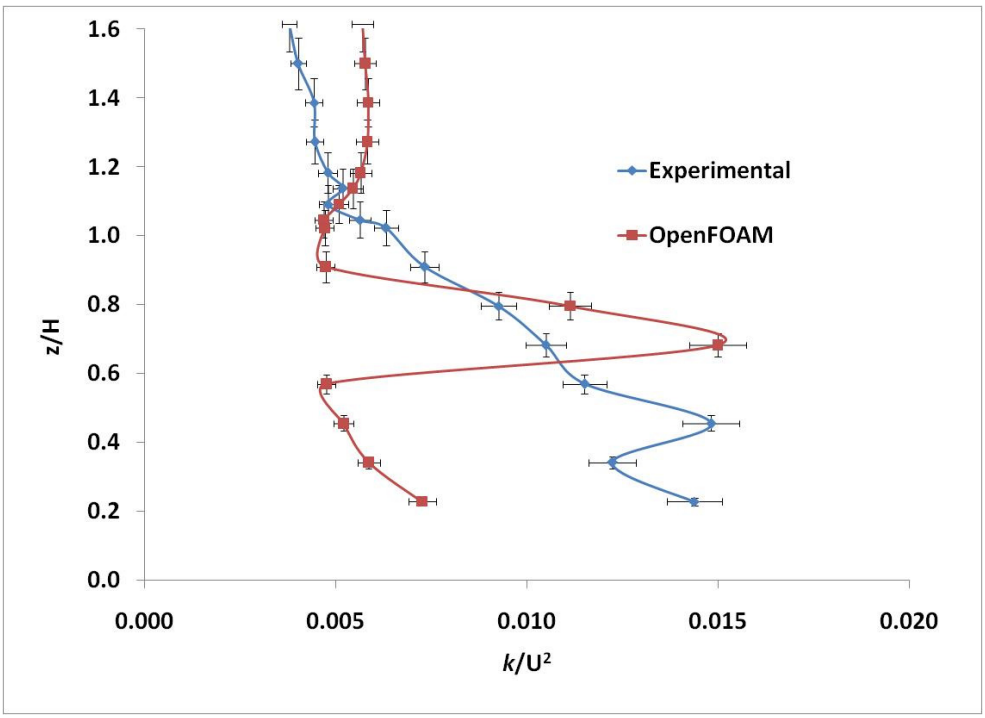

Figure 6.11. Comparison of normalized *k* profiles between experimental and CFD simulation results. Error bars represent values within 5%.

6.4. Conclusions

Wind speeds measured from the wind tunnel experiment differed slightly from the numerical simulation using OpenFOAM, especially at portions in which split straws were present. Such discrepancies could be a result of oscillatory motions unaccounted for during the simulation because the geometry used was stationary and not as dynamic as geometry observed during the experiment. Effective drag coefficients computed using wind profiles did not differ significantly ($p > 0.05$) between experimental and simulated results. In addition, differences found in normalized *k* profiles between the simulation and experimental values could be due to limitations of the turbulence model to simulate velocity fluctuations within the split straw regions. Results of this study will allow possibilities for research of other types of simulated

stubble or sparse vegetation during wind erosion events. Employment of dynamic motion using dynamic mesh in CFD simulation is recommended for validation with experimental results.

6.5. References

Bitog, J.P., Lee, I.B., Hwang, H.S., Shin, M.H., Hong, S.W., Seo, I.H., Kwon, K.S., Mostafa, E., & Pang, Z. 2012. Numerical simulation study of a tree windbreak. *Biosystems Eng.* 111(1): 40-48.

Bonifacio, H.F., Maghirang, R.G., & Glasgow, L.A. 2014. Numerical simulation of transport of particles emitted from ground-level area source using AERMOD and CFD. *Eng. Appl. Comp. Fluid Mech.* 8(4): 488-502.

Bourdin, P. & Wilson, J.D. 2008. Windbreak aerodynamics: Is computational fluid dynamics realiable? *Boundary Layer Meteorol.* 126: 181-208.

Cellier, P., & Brunet, Y. 1992. Flux-gradient relationships above tall canopies. *Agric. Forest. Meteorol.* 58: 93-117.

Cheng, Y., Lien, F.S., Yee, E., & Sinclair, R. 2003. A comparison of large eddy simulations with a standard $k - \varepsilon$ Reynolds-averaged Navier-Stokes model for the prediction of a fully developed turbulent flow over a matrix of cubes. *J. Wind Eng.* 91: 1301-1328.

Cionco, R.M., & Ellefsen, R. 1998. High resolution urban morphology data for urban wind flow modelling. *Atmos. Environ.* 32: 7-17.

Defraeye, T., Blocken, B.. Koninckx, E., Hespel, P., & Carmeliet, J. 2010. Aerodynamic study of different cyclist positions: CFD analysis and full-scale wind-tunnel tests. *J. Biomech.* 43(7): 1262-1268.

Dong, Z., Gao, S., & Fryrear, D.W. 2001. Drag coefficients, roughness length and zero-plane displacement height as disturbed by artificial standing vegetation. *J. Arid Environ.* 49(3): 485-505.

Endalew, A.M., Hertog, M., Delele, M.A., Baetens, K., Persoons, T., Baelmans, M., Ramon, H., Nicolaï, B.M., & Verboven, P. 2009. CFD modelling and wind tunnel validation of airflow through plant canopies using 3D canopy architecture. *Int. J. Heat Fluid Flow* 30: 356-368.

Fryrear, D.W., Stout, J.E., Hagen, L.J., & Vories, E.D. 1991. Wind erosion: Field measurement and analysis. *Trans. ASAE.* 34(1): 155-160.

Georgiadis, T., Dalpane, E., Rossi, F., & Nerozzi, F. 1996. Orchard-atmosphere physical exchanges: Modelling the canopy aerodynamics. *Acta Hort.* 416: 177-182.

Gromke, C., Buccolieri, R., Di Sabatino, S., & Ruck, B. 2008. Dispersion study in a street canyon with tree planting by means of wind tunnel and numerical investigations - Evaluation of CFD data with experimental data. *Atmos. Environ.* 42: 8640-8650.

Guo, L. & Maghirang, R.G. 2012. Numerical simulation of airflow and particle collection by vegetative barriers. *Eng. Applic. Comp. Fluid Mech.* 6(1): 110-122.

Hagen, L.J. 1996. Crop residue effects on aerodynamic processes and wind erosion. *Theor. Appl. Climatol.* 54: 39-46.

Hagen, L.J., & Armbrust, D.V. 1994. Plant canopy effects on wind erosion saltation. *Trans. ASAE.* 37(2): 461-465.

Hagen, L. & Skidmore, E. 1971. Windbreak drag as influenced by porosity. *Trans. ASAE* 14: 464-465.

Higuera, P., Lara, J.L., & Losada, I.J. 2013. Simulating coastal engineering processes with OpenFOAM. *Coastal Eng.* 71: 119-134.

Hyams, D.G. 2013. Curve expert 1.4 software. www.curveexpert.net

Katul, G.G., Mahrt, L., Poggi, D., & Sanz, C. 2004. One- and two-equation models for canopy turbulence. *Boundary-Layer Meteorol.* 113: 81-109.

Lancaster, N., & Baas, A. 1998. Influence of vegetation cover on sand transport by wind: Field studies at Owens Lake, California. *Earth Surface Processes & Landforms* 23: 69-82.

Lee, I.B., Sase, S., & Sung, S.H. 2007. Evaluation of CFD accuracy for the ventilation study of a naturally ventilated broiler house. *Japan Agri. Res. Quarterly* 41(1): 53-64.

Lee, S.J. & Lim, H.C. 2001. A numerical study on flow around a triangular prism located behind a porous fence. *Fluid Dynamics Res.* 28: 209-221.

Li, F.R., Kang, L.F., Zhang, H., Zhao, L.Y., Shirato, Y., & Taniyama, I. 2005. Changes in intensity of wind erosion at different stages of degradation development in grasslands of Inner Mongolia, China. *J. Arid Environ.* 62(4): 567-585.

Li, W., Wang, F., & Bell, S. 2007. Simulating the sheltering effects of windbreaks in urban outdoor open space. *J. Wind Eng. Ind. Aerodyn.* 95: 533-549.

Lin, X.-J., Barrington, S., Choiniere, D., & Prasher, S. 2007. Simulation of the effect of windbreaks on odour dispersion. *Biosys. Eng.* 98: 347-363.

Lyles, L. & Allison, B.E. 1976. Wind erosion: The protective role of simulated standing stubble. *Trans. ASAE* 19(1): 61-64.

Lysenko, D.A., Ertesvåg, I.S., & Rian, K.E. 2013. Modeling of turbulent separated flows using OpenFOAM. *Computers & Fluids* 80: 408-422.

Menter, F.R. 1994. Two-equation eddy-viscosity turbulence models for engineering applications. *AIAA Journal* 32: 1598-1605.

Musick, H.B. & Gillette, D.A. 1990. Field evaluation of relationships between a vegetation structural parameter and sheltering against wind erosion. *Land Degrad. Dev.* 2(2): 87-94.

OpenCFD Ltd. 2011. OpenFOAM User Manual.

Packwood, A.R. 2000. Flow through porous fences in thick boundary layers: comparisons between laboratory and numerical experiments. *J. Wind Eng. Indus. Aerodyn.* 88: 75-90.

Patankar, S.V. 1980. Numerical heat transfer and fluid flow. Hemisphere, Washington, D.C.

Politis, A.K., Stavropoulos, G.P., Christolis, M.N., Panagopoulos, P.G., Vlachos, N.S., & Markatos, N.C. 2008. Numerical modelling of simulated blood flow in idealized composite arterial coronary grafts: Transient flow. *J. Biomech.* 41(1): 25-39.

Pyles, R.D., Paw, U.K.T., & Falk, M. 2004. Directional wind shear within an old-growth temperate forest rainforest: Observations and model results. *Agric. Forest Meteorol.* 125: 19-31.

Quiao, A. & Liu, Y. 2008. Medical application oriented blood flow simulation. *Clinical Biomech.* 23(1): S130-S136.

Richards, P.J., & Hoxey, R.P. 1993. Approriate boundary conditions for computational wind engineering models using the $k - \varepsilon$ turbulence model. *J. Wind Eng. Ind. Aerodyn.* 46&47: 145-153.

Rosenfeld, M., Marom, G., & Bitan, A. 2010. Numerical simulation of the airflow across trees in a windbreak. *Boundary Layer Meteorol.* 135(1): 89-107.

Salomé Platform. 2013. User Guide: Salomé - The Open Source Integration Platform for Numerical Simulation. http://www.salome-platform.org.

Santiago, J.L., Martin, F., Cuerva, A., Bezdenejnykh, N., & Sanz-Andres, A. 2007. Experimental and numerical study of wind flow behind windbreaks. *Atmos. Environ.* 41: 6406-6420.

Stockton, P.H. & Gillette, D.A. 1990. Field measurement of the sheltering effect of vegetation on erodible land surfaces. *Land Degrad. Develop.* 2(2): 77-85.

Tiwary, A., Morvan, H.P., & Colls, J.J. 2005. Modelling the size-dependent collection efficiency of hedgerows for ambient aerosols. *Aerosol Sci.* 37: 990-1015.

Toure, A.A., Rajot, J.L., Garba, Z., Marticorena, B., Petit, C., & Sebag, D. 2011. Impact of very low crop residues cover on wind erosion in the Sahel. *Catena* 85: 205-214.

van de Ven, T.A.M., Fryrear, D.W., & Spaan, W.P. 1989. Vegetation characteristics and soil loss by wind. *J. Soil Water Conservation* 44(4): 347-349.

Wieringa, J. 1993. Representative roughness parameters for homogeneous terrain. *Boundary-Layer Meteorol.* 63: 323-363.

Wolfe, S.A. & Nickling, W.G. 1993. The protective role of sparse vegetation in wind erosion. *Progress Phys. Geog.* 17(1): 50-68.

Yeh, C.P., Tsai, C.H., & Yang, R.J. 2010. An investigation into the sheltering performance of porous windbreaks under various wind directions. *J. Wind Eng. Ind. Aerodyn.* 98: 520-532.

CHAPTER 7 - Numerical Simulation of Air and Particle Flow Across a Single Row of Vegetative Barrier (*Maclura pomifera*)

7.1. Introduction

Vegetative barriers are often used on the perimeter of agricultural lands to prevent complications arising from wind erosion. Benefits of these barriers have been widely documented (Bird et al., 1992; Cleugh, 1998; Ffolliott, 1998; Kort, 1998; Mader et al., 1999; Sudmeyer et al., 2002; Grala et al., 2010; Lazzaro et al., 2008). Studies have determined factors that promote these benefits (Hagen and Skidmore, 1971; Fryrear and Skidmore, 1985; Gregory, 1995; Brandle et al., 2004; Tiwary et al., 2005; Santiago et al., 2007; De Zoysa, 2008; Guo, 2008; El-Flah, 2009; Rosenfeld et al., 2010), but the studies have been limited only to specific types of vegetative barrier. Osage orange trees (*Maclura pomifera*), a commonly used vegetative barrier in Kansas agricultural lands, are known for their relative strength and durability. Osage orange trees also were used to successfully fence and protect agricultural lands, as detailed by Smith and Perino (1981).

Although Osage orange is commonly used as a vegetative barrier in Kansas, limited information is available on its properties for efficient sheltering of crops. As a deciduous tree, foliage density variation occurs throughout the year; therefore, effectiveness of the tree as a barrier during its leaf-off stage compared to its leaf-on condition is expected to differ.

On-site field tests are necessary to determine actual behavior and measurement parameters (i.e., flow patterns, filtration and dust collection measures, aerodynamic parameters), but these tests are limited by weather conditions, instrument availability, and cost. An alternative approach is numerical simulation using computational fluid dynamics (CFD) (Norton and Sun, 2006). Use of CFD software to run simulations has become increasingly popular because of its

power to optimize characteristic parameters for the applied process. Many fields of study (Parsons et al., 2004; Norton and Sun, 2006; Zhang, et al., 2008; Schlegel et al., 2012) have utilized this technology. In addition to growth of CFD, advancement in the use of open-source software (freeware under the GNU Public License (GPL)) has also grown.

This study aimed to predict airflow and particle collection through Osage orange barriers using open-source CFD software. Specific objectives were to:

1) simulate airflow through a porous region using OpenFOAM;
2) simulate particle collection efficiency of Osage orange barrier using OpenFOAM; and
3) compare experimental results to simulation results.

7.2. Materials and Methods

7.2.1. Computational Domain

Field measurements were conducted at a farm near Riley, Kansas, to differentiate airflow across the Osage orange barrier. The study was conducted from August 2013 to December 2013 during leaf-on and leaf-off stages and between August 2014 and September 2014 to test ability of Osage orange barrier during leaf-on stage to capture dust particles. Aerodynamic properties (i.e., aerodynamic and optical porosities, drag coefficients) of the Osage orange barrier obtained in Chapters 4 and 5 served as input parameters for numerical simulation. Mean wind profiles from the field study were also used as input velocities for the simulation. The vegetative barrier row considered for the simulation had dimensions of 2.5 m in width and an average tree height (H) of 8.5 m and length of 50 m. To simplify numerical analysis, end effects were neglected and the vegetative barrier was considered as a uniform row of barrier (Rosenfeld et al., 2010). The computational domain had an upwind distance of 30H from the barrier row, downwind distance of 80H, and height of 8H.

7.2.2. Governing Equations

Airflow was assumed to follow a steady-state, isothermal, two-dimensional (2D) turbulent flow (Yeh et al., 2010; Guo and Maghirang, 2012). Continuity and momentum conservation equations used (Santiago et. al., 2007; Rosenfeld et al., 2010; Bitog et al., 2012; Guo and Maghirang, 2012) were as follows:

$$\frac{\partial \overline{u_i}}{\partial x_i} = 0 \tag{7.1}$$

$$\overline{\mu_j}\frac{\partial \overline{\mu_i}}{\partial x_j} = -\frac{1}{\rho}\frac{\partial \bar{P}}{\partial x_i} + u\frac{\partial^2 \overline{\mu_i}}{\partial x_j^2} - \frac{\partial}{\partial x_j}\left(\mu_i'\mu_j'\right) + S_i \tag{7.2}$$

where *i* is the subscript for all three directions (*x*, *y*, and *z*), *j* is the subscript for the direction evaluated (*x*, *y*, or *z*), u is the velocity (m s^{-1}), $\bar{P}$ is the pressure force (Pa) in *i*-direction evaluated, μ is the fluid viscosity (N s m^{-2}), and S_i is the source term. Bar symbols in Eq. 7.1 and 7.2 are average component values resulting from use of the Reynolds decomposition method.

The RNG $k-\varepsilon$ model turbulence closure model described in Chapter 6 , a model used by numerous studies regarding simulation of vegetative barriers (Lee and Lim, 2001; Packwood, 2000; Lee et. al., 2007; Li et al., 2007; Santiago et al., 2007; Bourdin and Wilson, 2008; Bitog et al., 2012) was implemented for this study. Equations for the RNG $k-\varepsilon$ model were given in Chapter 6.

7.2.3. Simulation of Vegetative Barrier as Porous Media

A momentum sink (pressure discontinuity) was implemented in the rectangular block geometry to simulate the porous vegetative barrier (Guo and Maghirang, 2012), incorporating viscous and inertial losses. By assuming that the porous region is fully homogeneous, the Darcy-Forchheimer equation for porous media, which accounts for viscous fluid effects, can be implemented as the momentum sink, given by

$$-\nabla p = \frac{\mu}{\alpha} u_i + \beta_D \rho |u| u_i \tag{7.3}$$

where ∇p is the pressure gradient due to the porous medium, α is permeability (m^2), β_D is inertial coefficient (m^{-1}) and ρ is density of fluid (kg m^{-3}). Implementation of Equation (7.3) in OpenFOAM is given by the following equation:

$$S_i = \mu \bar{\bar{d}} u_i + \bar{\bar{f}} \frac{1}{2} \rho |u| u_i \tag{7.4}$$

where $\bar{\bar{d}}$ and $\bar{\bar{f}}$ are porosity parameter inputs within the OpenFOAM structure that were solved through the permeability and inertial resistance values, given by the following:

$$\bar{\bar{d}} = \frac{1}{\alpha} \tag{7.5}$$

$$\bar{\bar{f}} = 2\beta_D \tag{7.6}$$

7.2.4. Simulation of Particle Transport

Particle transport through vegetative barriers was simulated using the convection-diffusion equation (scalar transport equation) that treated particle concentration as passive scalar (Bonifacio et al., 2014):

$$\frac{\partial}{\partial x_i}(u_i C) - \frac{\partial^2}{\partial x_i^2}(\Gamma_D C) = 0 \tag{7.7}$$

where C is particle concentration and Γ_D is effective diffusion coefficient of particles. Furthermore, $\Gamma_D = \Gamma_L + \Gamma_T$ where Γ_L is the laminar component, while Γ_T is the turbulent component. Γ_L is computed using the Stokes-Einstein equation (Guo and Maghirang, 2012):

$$\Gamma_L = \frac{\zeta T C_c}{3\pi\mu d_p} \tag{7.8}$$

where ζ is the Boltzmann constant, T is absolute temperature (K), C_c is the slip correction factor, and d_p is particle diameter. C_c was computed with the following equation:

$$C_C = 1 + \frac{\lambda}{d_p}\left[2.34 + 1.05exp\left(-\frac{0.39d_p}{\lambda}\right)\right] \quad (7.9)$$

where λ is the mean free path (μm). Computation of Γ_L gave a value of 7.70 x 10^{-13} m^2 s^{-1} for a 32-μm particle diameter (based on computed GMD of dust used during field tests in Chapter 5). Γ_T was computed using the following equation:

$$\Gamma_T = \frac{\left(\frac{\rho C_\mu k}{\varepsilon}\right)}{Sc_t} \quad (7.10)$$

where Sc_t is the turbulent Schmidt number. Tominaga and Stathotpoulos (2007) summarized the choice of value for Sc_t, indicating that specific types of flow fields require different values of Sc_t. For this study, a value of 0.63 was used based on the Riddle et al. (2004) study that showed values lower than 0.7 gave better predictions of plume dispersion. Computed Γ_T showed values in the range of 7.58 x 10^{-2} to 22.9 m^2 s^{-1}, proving that $\Gamma_T >> \Gamma_L$ simplifies the definition of the effective diffusion coefficient to be equal to the turbulent component only. Gravitational settling of particles was not accounted for in this study.

Eq. 7.7 solves particle transport concentration by implementing a user-defined stationary velocity field. Thus, for this study, the velocity field was obtained from results of the porousSimpleFoam solver that was then used as input for velocity fields in the OpenFOAM solver (scalarTransportFoam) modified based on Equation 7.7.

Convergence was set up by assuring that residuals should be less than 1 x 10^{-7}, and it was reached for approximately 10,000 iterations for wind velocity simulation, and approximately 2,300 iterations were required for the concentration simulation.

7.2.5. Geometry and Mesh Generation

Because the Osage orange barrier was represented by a rectangular block for the remainder of the simulation, the blockMesh tool was used to generate the mesh shown in Figure 7.1. A porous zone was created to represent the porous region. In this case, the topoSet utility (topoSetDict file) within OpenFOAM structure was used to set up and create sets of faces that were bounding regions for the porous zone (i.e., the region in which the tree barrier exists).

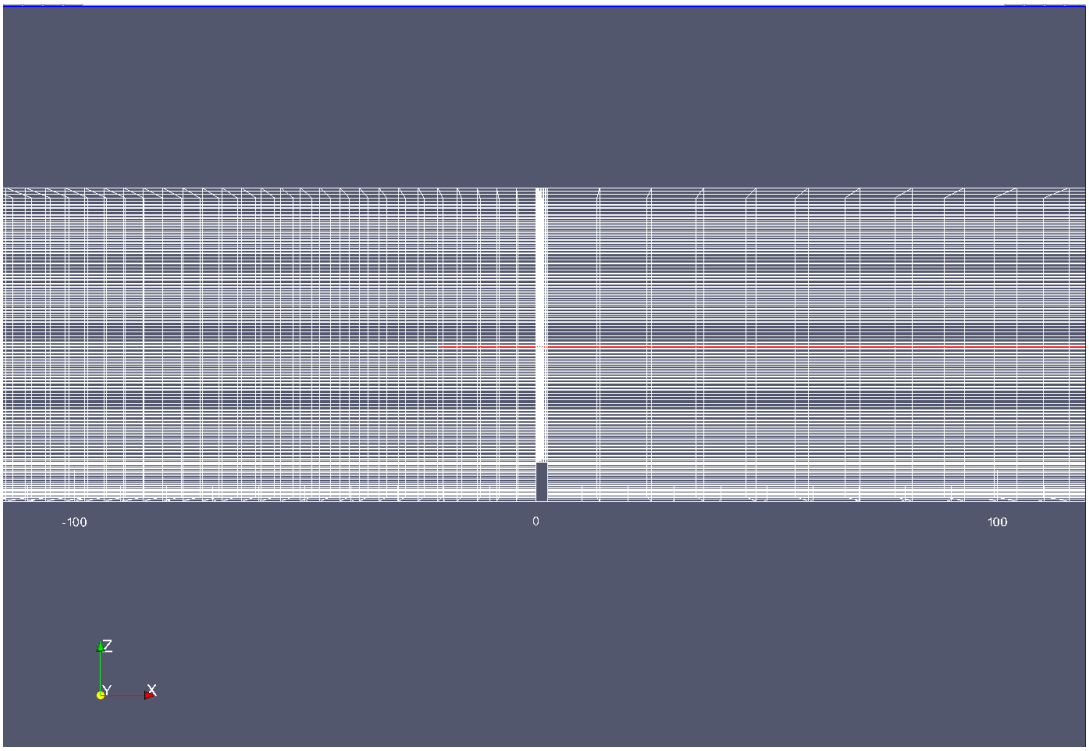

Figure 7.1. Mesh created using blockMesh tool in OpenFOAM as visualized in ParaView (zoomed-in version to show grids).

Table 7.1. Computational grid for porous barrier.

Cells		12800
Faces		51450
Nodes		26102
x coordinate (m)	min	-255
	max	680
z coordinate (m)	min	0
	max	68

7.2.6. Use of OpenFOAM for Simulation (Processing)

For this study, the porousSimpleFoam solver was used to model steady-state, incompressible turbulent flow of air with porous media treatment. It is based on the semi-implicit method for pressure linked equations (SIMPLE) algorithm developed by Patankar (1980) for decoupling pressure and velocity (OpenCFD, 2011). As per OpenFOAM requirements, three general folders (0, constant, and system folders) were required to run the solver, but an additional dictionary file for porous media treatment was included. A porosityProperties file was necessary to define and create the porous region named by default as cellZone. This region was set up so that the porosity parameters followed the Darcy Forchheimer equation (Equation 7.4).

The 0 folder included files for initial and boundary conditions (i.e., ε, k, p, and $U-$ termed epsilon, kappa, p, and U files, respectively, in OpenFOAM). The constant folder included files for geometry (i.e., blockMeshDict), file for creating the porous zone (i.e., porosityProperties), and file that dictated the type of turbulence model to be used (i.e., Reynolds-average simulation properties (RASProperties)). The system folder included files that dictated the extent of iteration (i.e., ControlDict), decomposition of solution for parallel runs (i.e.,

decomposeParDict), solution mechanisms that defined turbulence parameters, relaxation, residual control values (i.e., fvSolution), and numerical schemes that defined the numerical approach for various operators in the main Navier-Stokes equation (i.e., fvSchemes). A summary of input values for CFD simulation is shown in Table 7.2.

The porousSimpleFoam solver results in velocity fields necessary for input to another solver (scalarTransportFoam) used for the particle collection simulation. An arbitrary uniform concentration of 1.0 was chosen as the initial concentration at the inlet.

Table 7.2. Input values for CFD simulation (OpenCFD, 2011; Guo and Maghirang, 2012; Bonifacio et al., 2014).

Parameter	Symbol	Value
Air density (kg m^{-3})	ρ	1.225
Air dynamic viscosity (kg m^{-1} s^{-1})	μ	1.79 x 10^{-5}
Kinematic viscosity (m^2 s^{-1})	υ	1.46 x 10^{-5}
Turbulence model constant	$C_{1\varepsilon}$	1.42
Turbulence model constant	$C_{2\varepsilon}$	1.68
Turbulence model constant	C_{μ}	0.09
Turbulence Prandtl number for k	σ_k	0.719
Turbulence Prandtl number for ε	σ_ε	0.719
Von Karman constant	κ	0.4187

7.2.7. Boundary Conditions

Initial values for ε, k, p, and U were placed as separate files in the 0 folder. These values were set for regions in the domain, namely inlet, outlet, upperWall, lowerWall, front, and back regions. The equilibrium boundary layer assumption (described by Richards and Hoxey, 1993; Santiago et al., 2007; Bourdin and Wilson, 2008; Yeh et al., 2010; Guo and Maghirang, 2012) was used as an assumption to obtain inlet values for ε and k, which were obtained by the following equations:

$$k_{in} = \frac{u_*^2}{\sqrt{C_\mu}} \tag{7.11}$$

$$\varepsilon_{in} = \frac{u_*^3}{\kappa z} \tag{7.12}$$

where u_* is friction velocity far upstream of the vegetation element (from previous field tests, u_* = 0.11 m s^{-1} obtained using equations enumerated in Chapter 3 where simultaneous wind profiles were accounted for to compute values of u_*). Pressure was initally set as atmospheric pressure (101325 Pa) inside the domain (internalField in OpenFOAM) and given zero gradient for inlet, upperWall, front and back; symmetry condition for upperWall; and constant outlet value. For other regions in the domain, outlet flow was given a fully-developed flow condition (i.e., zero velocity gradient), symmetry condition at the upperWall, back and front regions, no-slip condition at the lowerWall, and near-wall conditions for ε and k (i.e., $epsilonWallFunction$ and $kqrWallFunction$, respectively) for all other domain regions were utilized.

Initial values inside the domain (internalField in OpenFOAM) for all parameters were set to zero. Wind velocity measurements during field tests served as input values for the *x*-component inlet velocities (u_x); other velocity components u_y and u_z were assumed to be zero.

7.2.8. Post-Processing

Visualization of simulation results was done in Paraview 3.40. A graphical interface (GNUPlot) was run simultaneously with the solver to cross-check results and preview behavior of residual values.

7.2.9. Determination of Resistance Coefficient of Osage Orange Barrier

Methodology of Tiwary et al. (2005) was adopted to compute resistance coefficients (k_r) within the Osage orange barrier necessary for the particle collection method. The method was based on studies of Raupach et al. (2001) where values of throughflow velocities (U_b) obtained at various height levels (z/H values were 0.18, 0.38, 0.5, and 0.8) during the experiment were incorporated into the following equation:

$$k_r = \frac{\Gamma_{bl}}{\left(\frac{U_b}{U_{0H}}\right)^2} - \Gamma_{bl} k_1 \tag{7.13}$$

where Γ_{bl} is bulk drag coefficient, U_{0H} is freestream velocity at various height levels, and

$$k_1 = 1 + 2a. \tag{7.14}$$

The value for Γ_{bl} used for the computation was 1.07, based on barriers in a field (Raupach et al., 2001). For this study, a value of 0.17 was assigned for the roughness parameter, a, because $a = 0.17$ denotes the presence of tall grasses evident in the field under study (according to Raupach et al. (2001) value of a could range from 0.14 (short grass) to 0.3 (orchards) adjacent to barriers). Values for U_{0H} were obtained from field measurements using the anemometer stationed upwind at the height of the barrier (x = -10H and z/H = 1).

7.2.10. Data Analysis

Normalized wind velocities measured during field tests were compared to CFD simulation results using the normality and homogeneity of variances assumption and a standard statistical test (e.g., paired t-test using Microsoft Excel (Microsoft Corp., Redmond, WA.)).

7.3. Results and Discussion

7.3.1. Aerodynamic Properties

Essential aerodynamic parameters (i.e., porosity, drag coefficient) needed for simulation are discussed in Chapter 4. For this study, only the leaf-on condition of the Osage orange barrier was addressed for dust transport because no field test of dust transport was conducted during the leaf-off condition of the barrier.

The profile of k_r for the Osage orange barrier (Figure 7.2) is similar to that presented by Tiwary et al. (2005) for Hawthorn hedge. Most resistance of the Osage orange tree was concentrated at the middle to the upper portion (peak value of k_r was observed at z/H = 0.8, identical to the observation by Tiwary et al. (2005)) where canopy density was high due to the presence of the leaves.

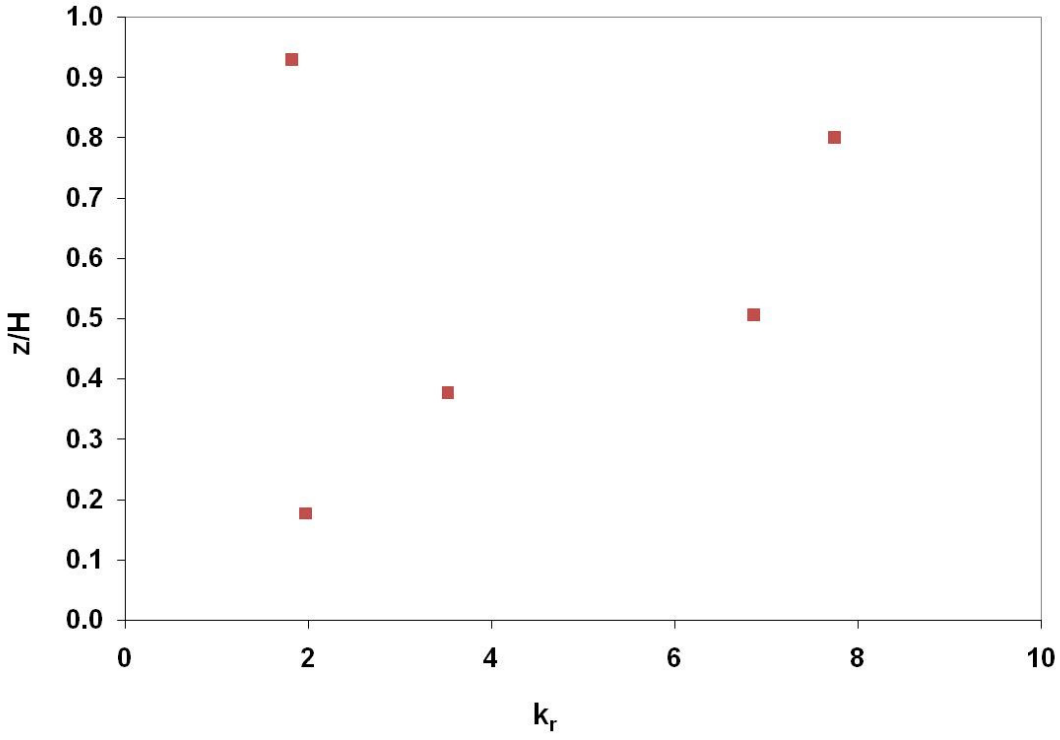

Figure 7.2. Resistance coefficients of the Osage orange barrier based on wind speed measurements at four heights.

7.3.2. Numerical Simulation Using OpenFOAM

A comparison of mean normalized wind speeds between field results and OpenFOAM simulation is shown in Figure 7.3. Normalization was obtained from the ratio of instantaneous velocities (u) and approach velocities (u_o) and the ratio of vertical tree heights (z) average tree height (H). Results of the OpenFOAM simulation were not significantly different from results of the field experiment ($p > 0.05$). Slight discrepancies in wind profiles could be due to the inherent difficulty in measuring wind velocities. During field tests, gathering of anemometer data spanned approximately 30 minutes per run and was conducted for three runs per downwind distance. Changes in wind speeds occurred between runs, potentially promoting differences in values.

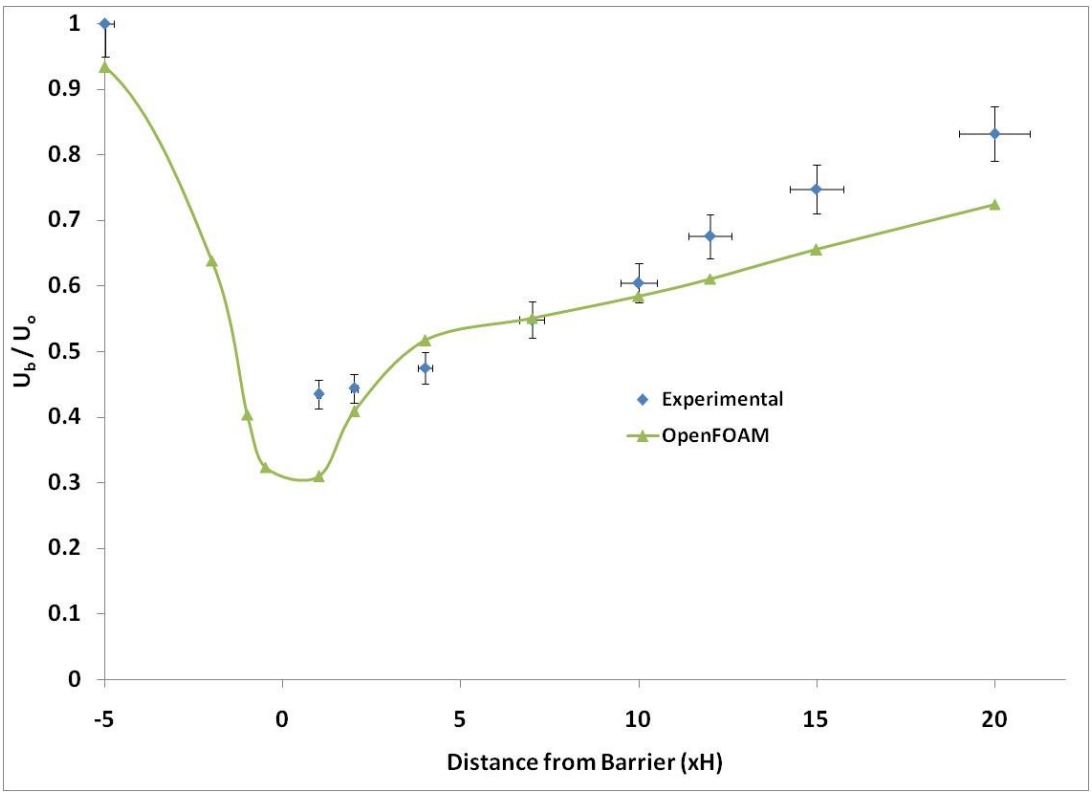

Figure 7.3. Comparison of normalized mean wind speeds between experimental results and CFD results. Error bars represent values within 5%.

Velocity fields from the porousSimpleFoam solver are shown in Figure 7.4. Unfortunately, ParaView generically shows axes labels as x, y, and z and for the figure, x = distance (m) from the barrier and z is height of domain (m). As shown in the figure, the extent to which velocity is reduced extends more than 10 times the height of the barrier used for simulation (8.5 m), as evidenced by the roughly triangular shaped contour on the velocity fields right after where the Osage orange barrier is located ($x = 0$ to $x = 2.5$). In addition, Figure 7.4 shows that approximately 1H upwind of the barrier, a velocity reduction was also evident in Figure 7.3 for the normalized wind profile using CFD simulation.

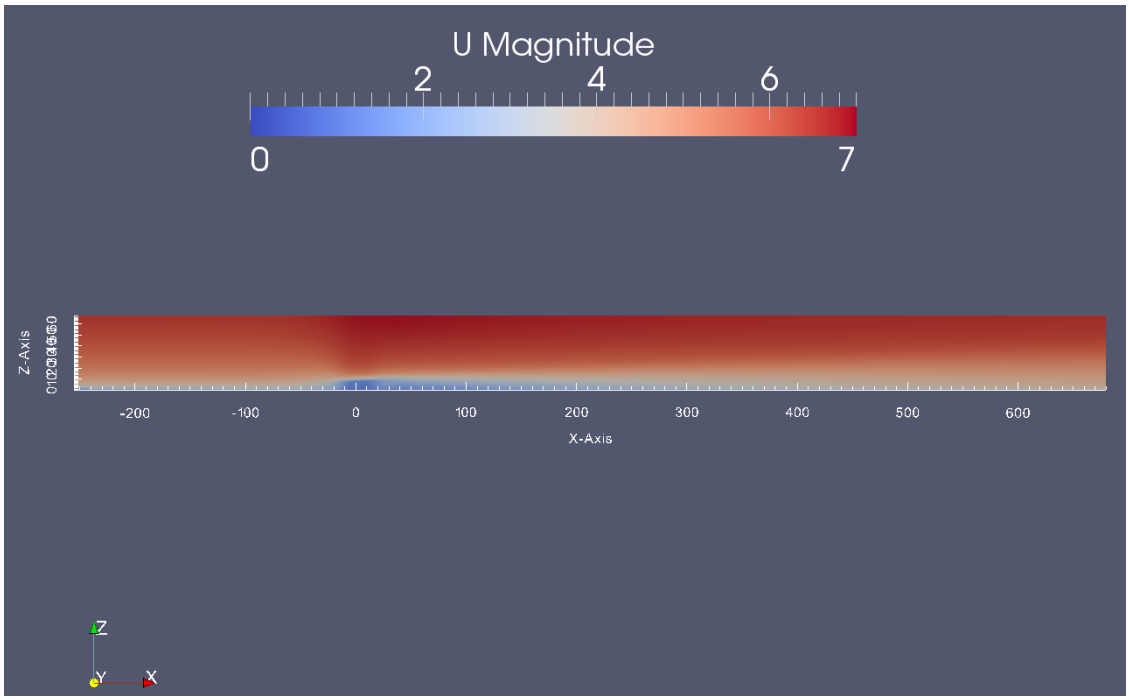

Figure 7.4. Velocity fields used as input for particle transport simulation.

A plot of normalized k within the height of the porous Osage orange barrier is shown in Figure 7.5. Normalization was done by taking the ratio of k with the square of the velocity (U^2) and the ratio of vertical height (z) with barrier height (H). Because the region considered for Figure 7.5 was the canopy flow region (Endalew et al., 2009), the *y*-axis for Figure 7.6 was set at 1.6 times the height of the canopy because it was believed that above such height, transition flow already occurs (Cellier and Brunet, 1992; Wieringa, 1993). The plot shows that resistance employed by the presence of the Osage orange barrier promoted greater turbulence in airflow along the height of the porous tree model. In addition, as the distance downwind from the barrier increased, turbulence caused by the presence of the barrier also decreased.

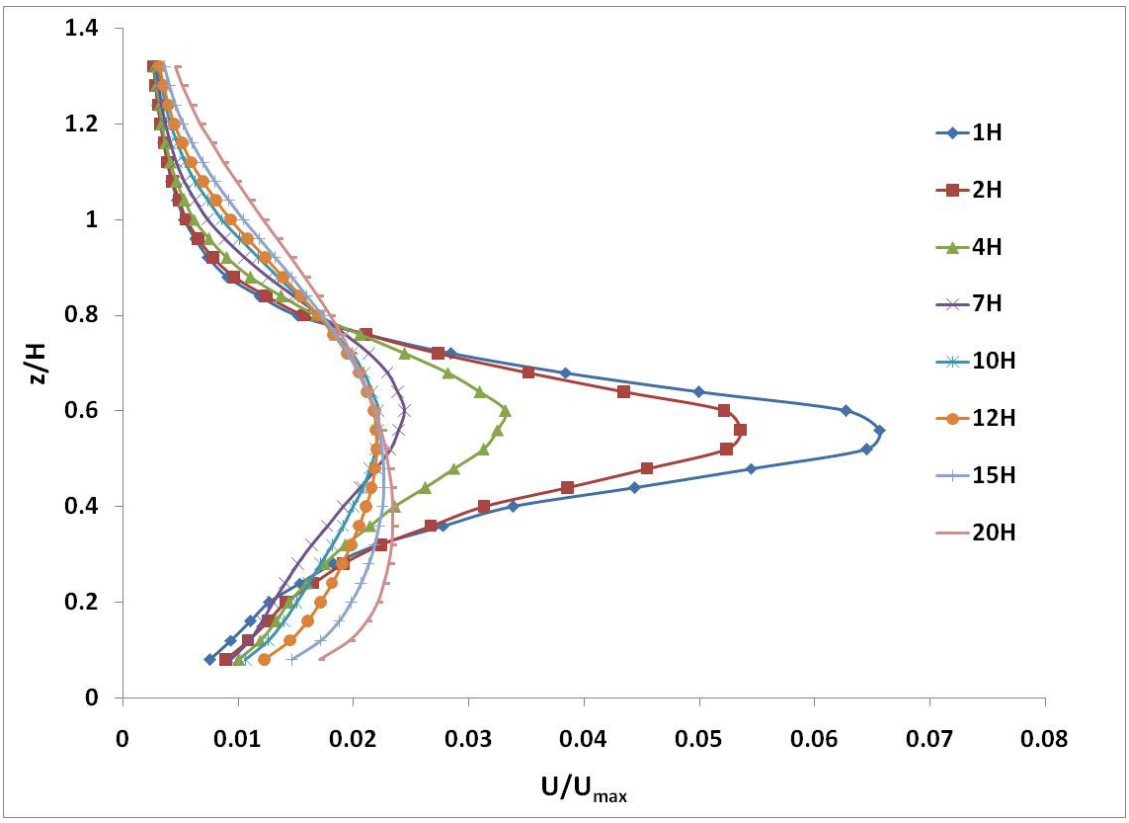

Figure 7.5. Normalized predicted *k* profiles downwind of the Osage orange barrier.

Reduction of dust concentration could extend up to 12H distance downwind the Osage orange barrier, as shown in concentration contours of Figure 7.6. This region of reduced concentration of particles is called the scrubbed layer (Raupach et al., 2001). A majority of the reduction in dust concentration occurred at the middle to upper portion of the porous Osage orange tree region (where vegetation elements such as leaves and branches are dominant), implying that the presence of vegetation elements are important for increasing effectiveness of the vegetative barrier and reducing dust. A decrease in dust concentration was observed slightly above the Osage orange barrier (part of the displaced region of airflow) where there could have been lowering of wind speed at such region which reduced dust concentration. This is due to the limitation of the study where the solver used did not consider gravitational settling and that the

magnitude of wind speed dictated the value of dust concentration. Figure 7.6 also implies that height of the vegetative barrier is a good indicator of particle removal efficiency of the tree barrier because reduction extended to approximately 12H.

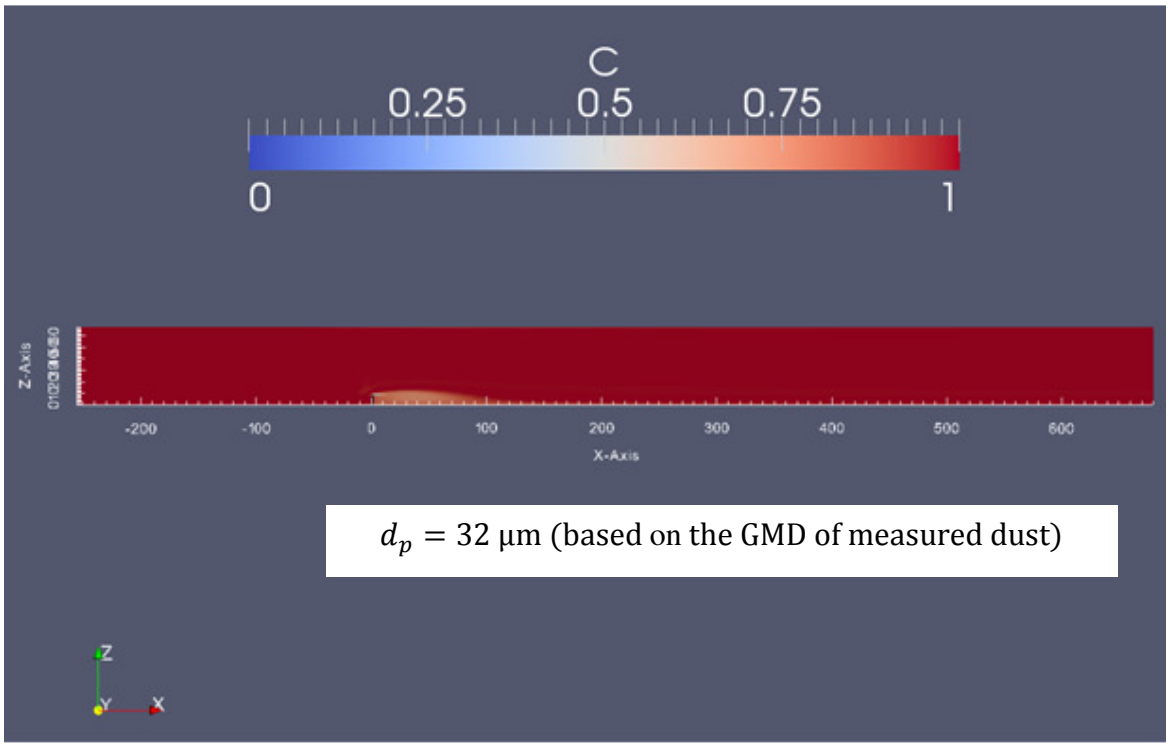

Figure 7.6. Simulation of particle concentration (µg m^{-3}) through the Osage orange barrier taken as a porous region.

According to Figure 7.7, horizontal variation of dust concentration was significantly lower within the vicinity of the Osage orange barrier (x = 0 to x = 2.5) and reduction also started upwind of the vegetative barrier. Guo and Maghirang (2012) observed the same shape of the concentration profile at the mixing zone (described by Judd et al., 1996) occurring further downwind (within the sheltered zone) of the vegetative barrier. The near-surface dust concentration approached equilibrium with the displaced profile as flow continued to evolve

downwind through the sheltered region of the vegetative barrier. Experimental measurements were also compared in which the source was considered to have a concentration of 1.0, while PM samplers (located upwind and downwind positions 1H away from barrier) showed a decrease of concentration similar to the CFD simulation. Particle concentration was reduced downwind of the barrier to approximately 0.70 of the original concentration obtained during field tests, while CFD simulations lowered the concentration to approximately 0.62. Discrepancies could be due to instantaneous changes in wind speed during experimentations that potentially affected the concentration of particles upwind and downwind of the barrier. Also, aside from gravitational settling not considered for the simulation, the particle collection/capture mechanism was also not considered for the simulation which could have accounted for such discrepancy in experimental and numerical simulation values.

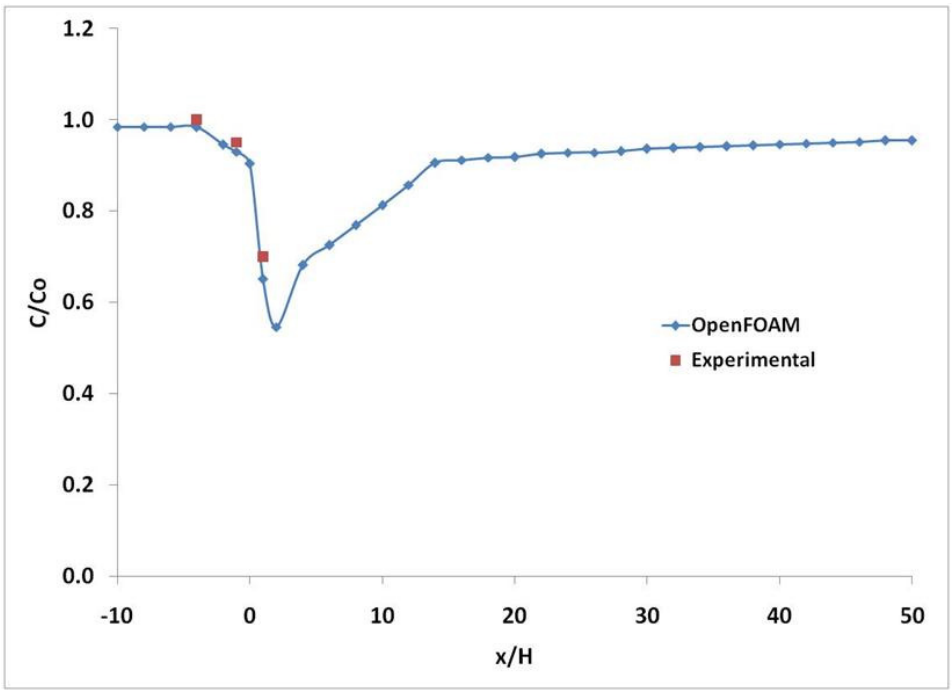

Figure 7.7. Horizontal variation of normalized dust concentration at z = 0.75H.

7.4. Conclusions

Numerical simulation of airflow and dust transport across an Osage orange tree vegetative barrier was conducted. The model in the open-source CFD software, OpenFOAM, predicted airflow and dust transport using simple block geometry to model the Osage orange tree as a porous region. No significant difference ($p > 0.05$) was observed between measured values of mean wind speeds during field tests and results from OpenFOAM. CFD simulation showed a lower value of concentration 1H downwind of the barrier ($C = 0.62$), while field tests showed a value of $C = 0.70$. Inherent difficulties in maintaining wind speeds during tests could account for the differences in values.

Further research on the effect of multiple rows of Osage orange trees and validation through experimental results are needed to further quantify aerodynamic effectiveness of Osage orange trees. Use of dynamic mesh and more complex geometry of actual trees could also be attempted as development of OpenFOAM progresses to enable more realistic modeling of vegetative barriers.

7.5. References

Bird, P.R., Bicknell, D., Bulman, P.A., Burke, S.J.A., Leys, J.F., Parker, J.N., van der Sommen, F.J., & Voller, P. 1992. The role of shelter in Australia for protecting soils, plants and livestock. *Agrofores. Sys.* 20: 59-86.

Bitog, J.P., Lee, I.B., Hwang, H.S., Shin, M.H., Hong, S.W., Seo, I.H., Kwon, K.S., Mostafa, E., & Pang, Z. 2012. Numerical simulation study of a tree windbreak. *Biosystems Eng.* 111(1): 40-48.

Bonifacio, H.F., Maghirang, R.G., & Glasgow, L.A. 2014. Numerical simulation of transport of particles emitted from ground-level area source using AERMOD and CFD. *Eng. Appl. Comp. Fluid Mech.* 8(4): 488-502.

Bourdin, P. & Wilson, J.D. 2008. Windbreak aerodynamics: Is computational fluid dynamics realiable? *Boundary Layer Meteorol.* 126: 181-208.

Brandle, J.R., Hodges, L., & Zhou, X.H. 2004. Windbreaks in North American agricultural systems. *Agrofores. Sys.* 61: 65-78.

Cellier, P., & Brunet, Y. 1992. Flux-gradient relationships above tall canopies. *Agric. Forest. Meteorol.* 58: 93-117.

Cleugh, H.A. 1998. Effects of windbreaks on airflow, microclimates, and crop yields. *Agroforestry Sys.* 41: 55-84.

De Zoysa, M. 2008. Casuarina coastal forest shelterbelts in Hambantota city, Sri Lanka: Assessment of Impacts. *Small-scale Fores.* 7: 17-27.

El-Flah, A.H. 2009. The use of various wind barriers in controlling wind erosion in Northwestern parts of Egypt. *J. App. Sci. Res.* 5(5): 490-498.

Endalew, A.M., Hertog, M., Delele, M.A., Baetens, K., Persoons, T., Baelmans, M., Ramon, H., Nicolaï, B.M., & Verboven, P. 2009. CFD modelling and wind tunnel validation of airflow through plant canopies using 3D canopy architecture. *Int. J. Heat Fluid Flow* 30: 356-368.

Ffolliott, P. 1998. Multiple benefits of arid land agroforestry home gardens and riparian ecosystems. In *Farming the forest for specialty products*. Proceedings of the Conference on Enterprise Development Through Agroforestry, ed., Josiah, S. J., 41-46. St. Paul, MN:

Center for Integrated Natural Resources and Agriculture Management, University of Minnesota.

Fryrear, D.W. & Skidmore, E.L. 1985. "Methods for Controlling Wind Erosion." In *Soil Erosion and Crop Productivity*, edited by R. F. Follett and B. A. Stewart. Madison, Wisc.: American Soc. Agronomy, Crop Sci. Soc. America, Soil Sci. Soc. America.

Gonzales, H. B. 2010. Cattle feedlot dust – Laser diffraction analysis of size distribution and estimation of emissions from unpaved roads and wind erosion. MS Thesis. Manhattan, Kan.: Kansas State University.

Gonzales, H.B., R.G. Maghirang, J.D. Wilson, E.B. Razote, and L. Guo. 2011. Measuring cattle feedlot dust using laser diffraction analysis. *Trans. ASAE* 54(6): 2319-2327.

Grala, R.K., Tyndall, J.C., & Mize, C.W. 2010. Impact of field windbreaks on visual appearance of agricultural lands. *Agroforest Sys.* 80: 411-422.

Gregory, N.G. 1995. The role of shelterbelts in protecting livestock: A review. *New Zealand J. Agri. Res.* 38: 423-450.

Guo, X. 2008. Function and structure of the farmland shelterbelts in northern area of Shanxi Province. *J. Fores. Res.* 13(3): 217-220.

Guo, L. & Maghirang, R.G. 2012. Numerical simulation of airflow and particle collection by vegetative barriers. *Eng. Applic. Comp. Fluid Mech.* 6(1): 110-122.

Hagen, L. & Skidmore, E. 1971. Windbreak drag as influenced by porosity. *Trans. ASAE* 14: 464-465.

Kort, J. 1988. Benefits of windbreaks to field and forage crops. *Agri. Ecosys. Environ.* 22-23: 165-191.

Lazzaro, L., Otto, S., & Zanin, G. 2008. Role of hedgerows in intercepting spray drift: Evaluation and modelling of the effects. *Agric. Ecosys. Environ.* 123(4): 317-327.

Lee, S.J. & Lim, H.C. 2001. A numerical study on flow around a triangular prism located behind a porous fence. *Fluid Dynamics Res.* 28: 209-221.

Lee, I.B., Sase, S., & Sung, S.H. 2007. Evaluation of CFD accuracy for the ventilation study of a naturally ventilated broiler house. *Japan Agri. Res. Quarterly* 41(1): 53-64.

Li, J., Okin, G.S., Alvarez, L., & Epstein, H. 2007. Quantitative effects of vegetation cover on wind erosion and soil nutrient loss in a desert grassland of southern New Mexico, USA. *Biogeochem.* 85(3): 317-332.

Mader, T.L., J.M. Dahlquist, G.L. Hahn, & Gaughan, J.B. 1999. Shade and wind barrier effects on summertime feedlot cattle performance. *J. Anim. Sci.* 77(8): 2065-2072.

Norton, T. & Sun, D.W. 2006. Computational fluid dynamics (CFD) - an effective and efficient design and analysis tool for the food industry: A review. *Trends Food Sci. Technol.* 17(11): 600-620.

OpenCFD Ltd. 2011. OpenFOAM User Manual. Available at http://cfd.direct/openfoam/user-guide/ Accessed May 2015.

Parsons, D.R., Wiggs, G.F.S., Walker, I.J., Ferguson, R.I., & Garvey, B.G. 2004. Numerical modelling of airflow over an idealised transverse dune. *Environ. Model. Softw.* 19: 153-162.

Patankar, S. V. 1980. *Numerical heat transfer and fluid flow*. Washington, D.C.: Hemisphere.

Raupach, M.R., Woods, N., Dorr, G., Leys, J.F., & Cleugh, H.A. 2001. The entrapment of particles by windbreaks. *Atmos. Environ.* 35(20): 3373-3383.

Riddle, A., Carruthers, D., Sharpe, A., McHugh, C., & Stocker, J. 2004. Comparisons between FLUENT and ADMS for atmospheric dispersion modeling. *Atmos. Environ.* 38: 1029-1038.

Rosenfeld, M., Marom, G., & Bitan, A. 2010. Numerical simulation of the airflow across trees in a windbreak. *Boundary Layer Meteorol.* 135(1): 89-107.

Santiago, J.L., Martin, F., Cuerva, A., Bezdenejnykh, N., & Sanz-Andres, A. 2007. Experimental and numerical study of wind flow behind windbreaks. *Atmos. Environ.* 41: 6406-6420.

Schlegel, F., Stiller, J., Bienert, A., Mass, H.G., Queck, R., & Bernhofer, C. 2012. Large-eddy simulation of inhomogeneous canopy flows using high resolution terrestrial laser scanning data. *Boundary-Layer Meteorol.* 142: 223-243.

Sellier, D., Brunet, Y., & Faurcaud, T. 2008. A numerical model of tree aerodynamic response to a turbulent flow. *Forestry* 81(3): 279-297.

Smith, J.L., & Perino, J.V. 1981. Osage Orange (*Maclura pomifera*): History and economic uses. *Econ. Bot.* 35(1): 24-41.

Sudmeyer, R.A., Crawford, M.C., Meinke, H., Poulton, P.L., & Robertson, M.J. 2002. Effect of artificial wind shelters on the growth and yield of rainfed crops. *Aus. J. Exp. Agric.* 42: 841-858.

Tiwary, A., Morvan, H.P., & Colls, J.J. 2005. Modelling the size-dependent collection efficiency of hedgerows for ambient aerosols. *Aerosol Sci.* 37: 990-1015.

Tominaga, Y. & Stathopoulos, T. 2007. Turbulent Schmidt numbers for CFD analysis with various types of flowfield. *Atmos. Environ.* 41: 8091-8099.

Wieringa, J. 1993. Representative roughness parameters for homogeneous terrain. *Boundary-Layer Meteorol.* 63: 323-363.

Yeh, C.P., Tsai, C.H., & Yang, R.J. 2010. An investigation into the sheltering performance of porous windbreaks under various wind directions. *J. Wind Eng. Ind. Aerodyn.* 98: 520-532.

Zhang, N., Zheng, Z.C. & Maghirang, R.G. 2008. Numerical simulation of smoke clearing with nanoparticle aggregates. *Int. J. Numer. Engng.* 74: 601-618.

CHAPTER 8 - Conclusions and Recommendations

8.1. Summary and Conclusions

Vegetation (i.e., standing vegetation and shelterbelts) are commonly used as control strategies to prevent wind erosion in Kansas. Research is needed to quantify aerodynamic properties of Osage orange (*Maclura pomifera*) and assess abrasion attributed to saltation through standing vegetation. This research was conducted to: (1) measure sand transport and abrasion on artificial standing vegetation, (2) determine porosity and drag of a single row of Osage orange (*Maclura pomifera*) barrier, (3) assess effectiveness of Osage orange barriers in reducing dust, (4) predict airflow through standing vegetation, and (5) predict airflow and particle collection through Osage orange barriers.

The following conclusions were drawn from this research:

- Tall (220 mm) standing vegetation had higher canopy aerodynamic roughness, showing greater canopy sheltering downwind than the shorter canopies. Sand discharge was dependent on canopy density and height within the tunnel. The abrasion coefficient was independent of wind speed but was dependent on canopy density. As canopy density increased, the wind profile and saltation behavior changed, causing less impact of saltating particles on the canopy and lowering abrasion coefficients.
- Leaf-on condition of the Osage orange barrier was more effective than leaf-off condition in reducing wind speeds downwind of the barrier. Aerodynamic (α_p) and optical (β_p) porosities of this species were determined using wind profiles and image analysis, respectively, and an empirical relationship was derived ($\alpha_p = {\beta_p}^{0.65}$; $R^2 =$

0.78). Optical porosity correlated well with drag coefficient ($R^2 = 0.98$) for the barrier.

- Field measurements showed that a single row of Osage orange removed 15 to 54% of PM less than 2.5 μm ($PM_{2.5}$) and 23 to 65 % of PM less than 10 μm (PM_{10}) of the incoming dust source. The crown portion of the vegetative barrier also removed a majority of the dust particles. PSD analysis showed that upwind of the barrier, large particles were dominantly collected by lower level samplers, while most small particles were collected by upper level samplers. However, downwind of the barrier, PSD analysis generally showed a decrease of GMD values at all height levels within the barrier (1.5, 3, 4.5, and 6 m), meaning that the Osage orange barrier removed dust particles that passed through it, especially large particles. However, small particles such as $PM_{2.5}$ and PM_{10} were removed more efficiently at the crown area of the tree (4.5 m and 6 m).
- Use of OpenFOAM as CFD simulation software with implementation of the RNG $k - \varepsilon$ turbulence model was able to simulate air flow through artificial standing vegetation. Discrepancies in wind speed values at the wake of standing vegetation between experimental and CFD results could be due to inability of OpenFOAM model to simulate oscillations occurring within the vegetation.
- OpenFOAM also simulated airflow and particle flow through the Osage orange barrier considered to be a porous region. No significant difference ($p > 0.05$) was observed between measured values of mean wind speeds during field tests and results from OpenFOAM. Particle concentration was reduced downwind of the barrier to approximately 0.70 of the original concentration obtained during field tests, while

CFD simulation lowered the concentration to approximately 0.62. Discrepancies could be due to instantaneous changes in wind speed during experimentations that potentially affected the concentration of particles upwind and downwind of the barrier. Also, there was no gravitational settling considered for the simulation.

8.2. Recommendations for Further Study

Wind erosion control using standing vegetation and barriers of specific tree species must be established to determine their specific advantages. Standing vegetation patterns and canopy densities within a field are important for increasing effectiveness of wind erosion control, but study of specific types of stubble and sparse vegetation is also ideal. Understanding dust transport through Osage orange barriers requires additional validation by taking into account lateral changes of airflow and particle flow within the barrier. Therefore, the following recommendations are included for future studies:

- Employ multiple PM samplers and anemometers at different locations parallel to the row of vegetative barriers (in addition to PM samplers at different heights) to account for lateral changes of particle concentration reductions as influenced by changes in wind speeds.
- Determine effects of weather parameters (i.e., humidity, precipitation) on dust transport through an Osage orange barrier in on agricultural land.
- Determine effects of various heights, widths, and lengths of Osage orange barriers on particle concentration reduction.
- Improve the OpenFOAM code to enable multiphase simulation of air and particle flow through vegetative barriers that could also be extended for use in actual tree geometry.